SAPIENZA
UNIVERSITÀ DI ROMA

Faculty of Mathematical, Physical and Natural Sciences

PhD School in Chemical Sciences
Cycle XXXI

Multitasking Fe_3O_4@Cu@Au and Fe_3O_4@SiO_2 nanoparticles for biomedical applications

PhD Supervisor:
Prof. Mario Barteri

PhD Student:
Ginevra Berardi

PhD Coordinator:
Prof. Osvaldo Lanzalunga

2018

TABLE OF CONTENTS

1. GENERAL INTRODUCTION

1.1 NANOPARTICLES AND NANOMEDICINE

Nanotechnology is a modern research field related to the design, development and use of materials at the nanoscale, which involves several scientific areas, including biology and chemistry. Nanomaterials have peculiar chemical and physical properties, different from those of the corresponding bulk materials, therefore they have attracted great interest. As shown in Figure 1.1-1 from ref. [1], the dimensions of nanomaterials allow them to easily interact with cells and subcellular elements, enabling the action on these biological systems. Therefore, in medicine and life science these materials are helpful and innovative tools; in fact, by using them new and more powerful strategies and applications can be performed, since they can solve several problems related to standard approaches.[2] In this context, the term "nanomedicine" has been introduced to indicate this branch of nanotechnology, dedicated to the development of nanomaterials for medical applications. Nanomaterials are suitable for *in vitro* diagnostics, *in vivo* imaging or therapy; moreover, some nanosystems are able to combine the therapeutic application with the diagnostic aspect, improving the quality and the sensitivity of imaging techniques, thus resulting promising theranostic tools for several pathologies.[3,4]

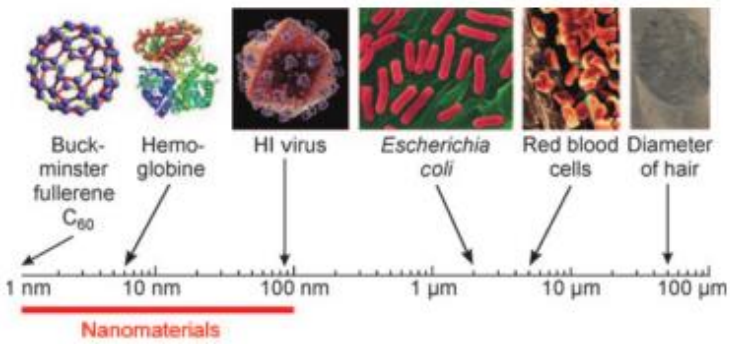

Figure 1.1-1: Length scale from 1 nm to 100 µm comparing nanomaterials to cells and subcellular elements (from ref. [1]).

In the wide world of nanomaterials, nanoparticles (NPs) are those presenting all three dimensions at the nanoscale.[5] As shown in Figure 1.1-2 from ref [6], NPs can be distinguished according to the chemical composition, shape, size and functionalization of the surface. These parameters can be modulated during the synthesis, in order to provide the proper instruments for a specific biomedical application.[2] For example, liposomes and polymeric NPs are promising tools in therapeutic applications, such as drug delivery, but they have some limitations in diagnostics. On the other hand, several inorganic NPs can be used for *in vitro* diagnostics or can be exploited as contrast agents in imaging techniques, improving the reliability of the diagnosis.

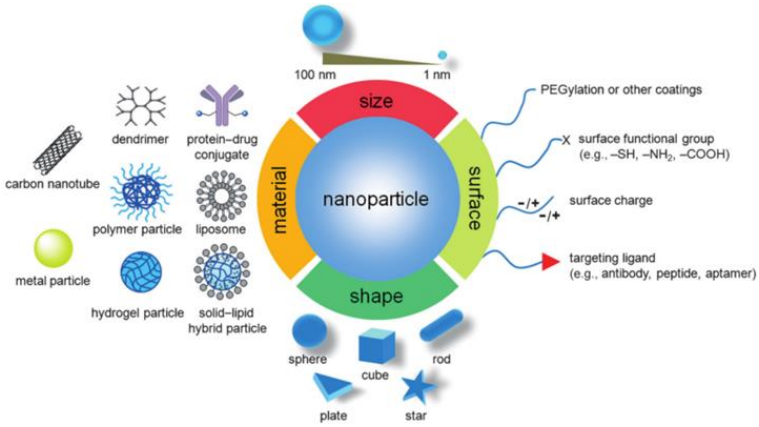

Figure 1.1-2: Schematic representation of nanoparticles used in nanomedicine, differing in chemical composition, size, surface functionalization or shape (from ref. [6]).

Concerning therapy, the use of NPs can provide solutions to the intrinsic limitations of classic drug administration methods; in fact, the drug loading on nanocarriers, especially lipid or polymeric ones, modify the pharmacokinetic features of the pharmaceuticals, for instance, improving their water-solubility and prolonging plasma half-life.[7] In this way, better therapeutic effects can be obtained, reducing the administered drug amount and, consequently, the side effects on healthy tissues. In this context, several liposomal drugs and polymer-drug conjugates are already commercially available or in clinical or preclinical

trials: for instance AmBisome® (Gilead Sciences, USA), a liposomal formulation of amphotericin B, or Prothecan® (Enzon Pharmaceuticals, USA), a PEG–camptothecin nanoconjugate, for the treatment of fungal and protozoal infections or various cancers, respectively.[2]

Conversely, inorganic NPs such as those made of Au or iron oxide are exploited for *in vivo* imaging techniques. Their optical or magnetic features make them good contrast agents for imaging techniques, providing more spatial and temporal information and increasing the sensitivity of the diagnostic tool. Moreover, their joining may often enable multimodal imaging combining different techniques. For instance, Au NPs can be exploited as contrast agents in X-ray imaging and computed tomography (CT) while iron oxide superparamagnetic NPs in magnetic resonance imaging (MRI).[8-10]

Concerning *in vitro* diagnostics, inorganic NPs like Au NPs or magnetic NPs are the most promising.[11] The nanoparticle-based diagnostics can offer advantages for the detection of specific markers, opening new frontiers in the diagnosis of several pathologies, including cancer, neurological disorders and infectious diseases.[12] Through adequate surface functionalization with macromolecules, especially enzymes and antibodies, interesting bioanalytical applications of NPs can be achieved, improving the sensitivity of the analytical methods or innovating them. For example, these kinds of NPs have been commonly employed in biosensors and immunoassays.[13,14] For instance, Au NPs have been used for detecting biologically relevant molecules in optical and electrochemical analytical methods.[15,16] Magnetic NPs, instead, have been utilized preferentially for detection and bio-separation of analytes or specific cell populations, like stem cells or pathogenic bacteria. In fact, by exploiting their magnetic properties, the application of an external magnetic field allows their efficient separation from a complex biological matrix.[17,18]

1.1.1 General features of NPs

NPs show peculiar chemical and physical characteristics which differentiate them from the corresponding bulk material. These properties can be divided into three groups: the surface-dependent, the dimension-related and those deriving from the quantum-size effect.[1]

The extended surface in the small volume of NPs leads to high surface-to-volume ratio that affects many of their properties. In fact, compared to 3D materials the increase in the number of surface atoms, characterized by binding weaker than the internal atoms, produces changes in the physicochemical properties, such as melting point and chemical reactivity. Other features like magnetic ones change, instead, according to the dimensions of the material. For example, ferromagnetic and ferrimagnetic materials exhibit superparamagnetic behaviour when their size is nanoscale.[19] Finally, the size-dependent quantum effects are related to the change in the electronic levels of nanomaterials, which become discrete sets instead of a continuum as in the bulk counterparts. Variations in the optical properties of Au NPs are due to this phenomenon.[20,21]

The presence of special intrinsic properties in NPs explains why they have had great success in the nanotechnological field and, in particular, in nanomedicine. Moreover, the characteristics of NPs can be adapted to obtain more specific nanosystems for a selected biomedical application through the surface coating with chemically different materials and/or the functionalization with biomolecules or pharmaceuticals.[22]

1.1.2 Multitasking NPs

In the last years, the scientific community is making considerable efforts to design and develop multifunctional nanosystems in order to improve and extend the applicability of the NPs in a theranostic view. A multitasking NP is defined as a system capable of carrying out different functions at the same time; for instance, presenting proper functionalities, a single nanoplatform can be suitable for diagnostic and therapeutic purposes.[23] The introduction of these functionalities can be performed during the synthesis of NPs through an appropriate modification of their surface with inorganic compounds or organic molecules or macromolecules which leads to the combination of the specific physical, chemical, biological or pharmaceutical features deriving from each component.

As shown in Figure 1.1-3 from ref. [24], a general multitasking nanosystem for theranostics contains both functionalities for diagnostic and for therapeutic purposes. For example, the presence of an inorganic material such as Au or iron oxide which have peculiar optical or magnetic properties make the NPs suitable in medical imaging techniques (MRI or optical imaging). Otherwise, the incorporation of elements or compounds presenting radioactivity or fluorescence, such as radionuclides, organic fluorescent probes or lanthanides, can help monitoring the nanosystems during *in vivo* diagnostic applications.[25] Often, a multimodal imaging using different techniques can also be possible.

At the same time, the presence of biologically or pharmacologically active compounds, for instance drugs or biomolecules, allows the use of the multitasking nanosystem as a therapeutic tool. Moreover, the addition of macromolecules or small molecules, like antibodies or targeting ligands, able to interact with specific biological target, can selectively address NPs into the pathological area.[3,24]

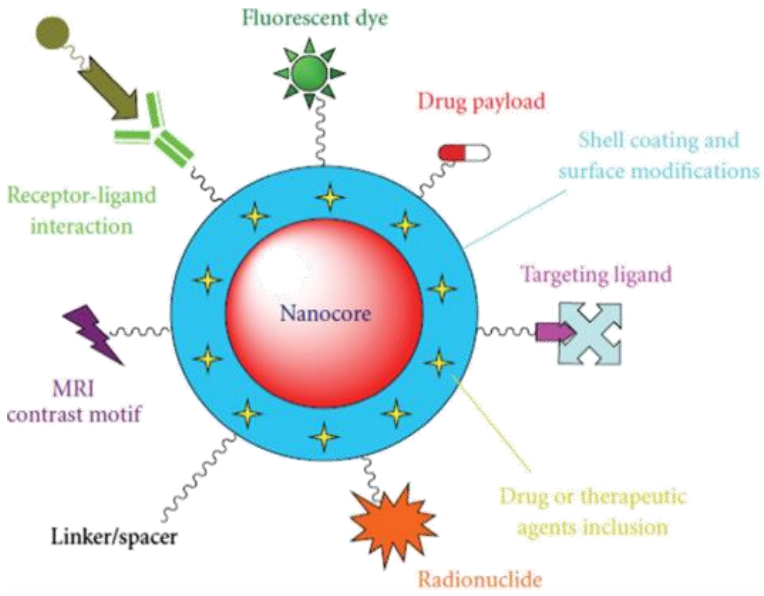

Figure 1.1-3: General representation of a multitasking nanosystem for theranostic applications (from ref. [24]). The nanocore can be coated by inorganic or organic shells and functionalized with molecules or macromolecules acting as targeting, therapeutic or diagnostic agents.

Concerning *in vitro* diagnostic, the combination of components with peculiar physical properties, like Au NPs or iron-oxide NPs, with molecules or macromolecules characterized by high-recognition features, like antibodies or specific ligands, can offer advantages in the analytical method. For instance, multitasking NPs can improve the analytical features of the technique, like sensitivity and specificity; they can allow the performance of multistep procedures in easier way, facilitating the sample preparation or reducing the time of the analysis.[26,27]

1.2 MAGNETIC NANOPARTICLES

Among the NPs, the magnetic ones can offer many solutions in nanomedicine, facilitating, innovating or integrating standard procedures. Being sensitive to the magnetic field, they can be helpful for *in vitro* and *in vivo* diagnostic techniques, but also in therapeutic applications such as drug delivery and hyperthermia.[28,29] The combination of these NPs with other materials, such as Au NPs, liposomes or polymers, or their modification with biologically relevant molecules are the main strategies to fulfil the need of efficient medical tools. Engineered magnetic NPs can therefore represent promising instruments in diagnostics and theranostics and may contribute to approach the personalized medicine.[25,26,30]

1.2.1 Magnetite nanoparticles and superparamagnetism

Among the most interesting magnetic nanoparticles (MNPs), iron oxides NPs are the best known and, in particular, those made of magnetite (Fe_3O_4) are considered the most promising for biomedical applications thanks to their special features. The crystal structure of Fe_3O_4, as shown in Figure 1.2-1 from ref. [31], consists in a cubic inverse spinel structure in which O atoms form a close-packed cubic lattice while the interstitial tetrahedral sites are occupied by Fe^{3+} ions and the octahedral ones by Fe^{3+} and Fe^{2+} ions.

The synthetic strategies commonly used to produce Fe_3O_4 MNPs are physical methods, such as gas-phase deposition and electron beam lithography, or wet chemical preparations, for instance sol-gel synthesis or chemical co-precipitation.[32-34] The last one is the simplest and most efficient synthesis method to obtain Fe_3O_4 MNPs. In the absence of surface coatings or functionalization, Fe_3O_4 MNPs are unstable since they tend to oxidize and aggregate. The transformation in hematite (α-Fe_2O_3) or maghemite (Υ-Fe_2O_3) or the increase of

the particle dimensions produce changes in the magnetic properties of the nanomaterials, limiting or compromising their biomedical use. [34]

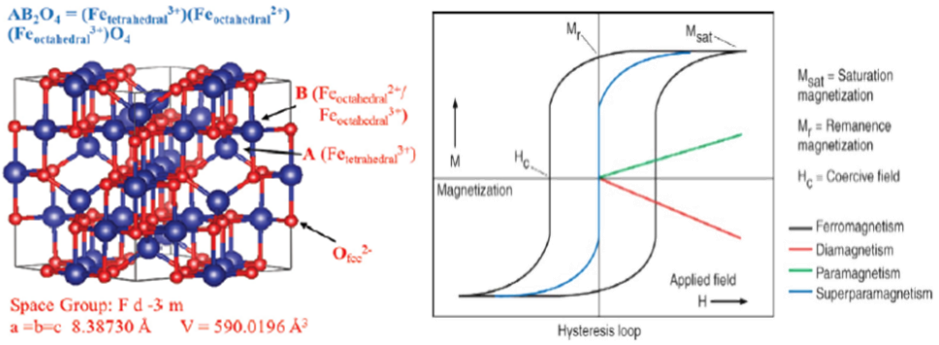

Figure 1.2-1: On the left: schematic representation of the inverse spinel structure of magnetite, highlighting Fe and O atoms in red and blue, respectively (from ref. [31]). Fe^{3+} ions occupied the interstitial octahedral and tetrahedral sites while Fe^{2+} ions only the octahedral ones. **On the right:** representation of the magnetization **M** *vs* applied field **H** plot for materials showing different magnetic properties (from ref. [28]).

1.2.1.1 Magnetic properties

The materials can be classified in paramagnetic, diamagnetic or ferromagnetic/ferrimagnetic depending on their response to an applied external magnetic field (**H**), and according to the value of the magnetic susceptibility (χ). This parameter represents the proportional constant between the magnetization of the material (**M**) and **H**, according to the equation $\mathbf{M} = \chi\mathbf{H}$. The values of $\chi > 0$ characterize paramagnetic materials, $\chi < 0$ the diamagnetic ones while $\chi >> 0$ the ferro/ferrimagnetic materials.

Figure 1.2-1 from ref. [28] shows the relation between **M** and **H**. From the graph **M** *vs* **H,** the parameters saturation magnetization ($\mathbf{M}_{sat}$), remanence ($\mathbf{M}_r$) and coercivity ($\mathbf{H}_c$) can be obtained. $\mathbf{M}_{sat}$ corresponds to the highest **M** value obtainable during the application of **H**. $\mathbf{M}_r$ represents the **M** value once **H** is absent while $\mathbf{H}_c$ is the intensity of the applied **H** required to reduce $\mathbf{M}_{sat}$ to zero.

Among the magnetic properties, ferromagnetism is considered a cooperative behaviour, since only a certain number of atoms bound together can display it. These materials possess unpaired electrons spins which align spontaneously in the same direction (ferromagnetic) or in the opposite one (antiferromagnetic), exhibiting magnetization in the absence of a magnetic field. When the number of the antiparallel aligned magnetic moments is not equal, an overall magnetization is present, and the material is classified as ferrimagnetic. Concerning Fe_3O_4, its ferrimagnetic character derives from the antiferromagnetic coupling between the Fe^{3+} ions which allows the magnetic moments of Fe^{2+} ions to generate the magnetization of the unit cell. Ferromagnetic and ferrimagnetic materials exhibit permanent magnetization once **H** is removed and they are characterized by the presence of the hysteresis loop into the **M** *vs* **H** representation. However, when the dimensions of the particles decrease up to a particular domain, each particle comprises a single magnetic domain and the magnetic behaviour changes from ferro/ferrimagnetism to superparamagnetism. For instance, in MNPs a size < 20 nm is required to have superparamagnetism while 128 nm is the critical dimension for forming multi-domain structures in spherical MNPs which leads to the decrease in the $\mathbf{H}_c$ value.[35] The main difference between ferro/ferrimagnetic and superparamagnetic material is that the second does not remain magnetized once the external magnetic field is removed, like a paramagnetic one. Superparamagnetic materials do not show magnetic hysteresis and their value of magnetic susceptibility is higher than that of paramagnetic materials and quite similar to ferromagnetic ones.[19]

1.3 BIOMEDICAL APPLICATIONS OF MNPs

The pharmaceutical and biomedical applications of Fe_3O_4 MNPs cover all the medical fields. The general features of NPs and the peculiar magnetic properties, biocompatibility and low cytotoxicity of Fe_3O_4 MNPs make them suitable for diagnostic, imaging and/or therapy. For *in vivo* applications they should have low dimensions and narrow size distribution, to avoid the rapid clearance, and high magnetization.[2,36] In this context, superparamagnetism is fundamental to avoid magnetically-driven particle agglomeration, after the removal of the magnetic field; in fact, the presence of aggregates can lead to occlusion of capillary vessels and dangerous side effects. To improve the chemical stability and biocompatibility of Fe_3O_4 MNPs surface functionalization is often required.[37] Engineered Fe_3O_4 MNPs are thus innovating standard medical strategies, improving their sensitivity and reliability, and are enabling new applications, previously unimaginable, especially in therapeutic treatments.

As depicted in Figure 1.3-1 from ref. [38], Fe_3O_4 MNPs are providing their benefits also in *in vitro* diagnostics in several bioanalytical methods, like biosensing techniques, in the separation and sample-enrichment of analytes or in the immobilization of macromolecules.[18,26,39] *In vivo* Fe_3O_4 MNPs are used as contrast agents in MRI, while their high potential as drug delivery systems or in hyperthermia has also been studied.[29,36] They can be used alone or in combination with other nanomaterials, allowing the joining of different properties and the widening of their applicability.[40,41] The biomedical applications of Fe_3O_4 MNPs are described in more details in the following sections.

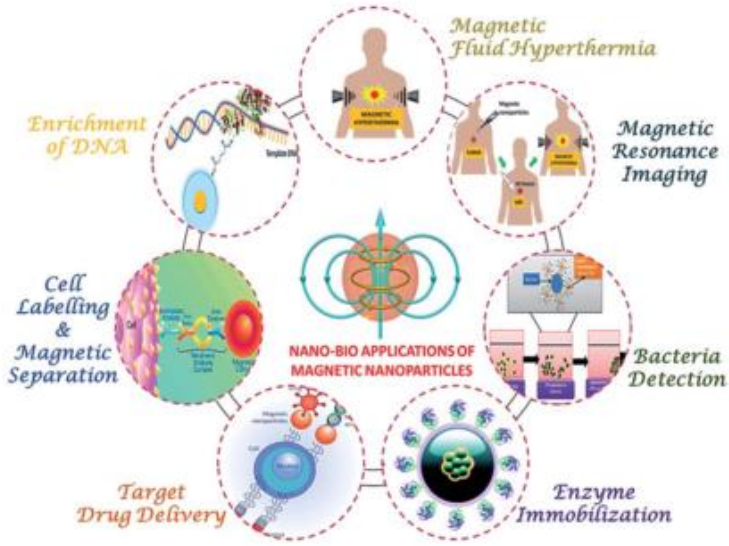

Figure 1.3-1: Schematic representation of biomedical applications of magnetic nanoparticles (from ref. [38]). MNPs can be exploited in therapeutic applications like magnetic hyperthermia and drug delivery or in *in vivo* imaging as contrast agents for MRI. Their main uses in *in vitro* diagnostics concern cell labelling and magnetic separation and immobilization of macromolecules.

1.3.1 *In vivo* imaging

A proper and reliable imaging of internal organs is fundamental for allowing the further appropriate medical treatments; in this area, MRI is one of the mainly used imaging techniques since it produces images with good temporal and spatial resolution without performing invasive procedures. In fact, MRI is very helpful in discriminating between healthy and affected tissue in case of several pathologies, related especially to soft tissues and cartilages. MRI is based on the achievement of relaxation signals of proton spins corresponding to water molecules in the human body, after the excitation by radiofrequency waves in a strong magnetic field.

Contrast agents, generally based on paramagnetic materials such as Gd, are used for clarifying the collected images and promoting a better diagnosis. Fe_3O_4 MNPs

are providing the development of a new generation of contrast agents; in fact, thanks to their superparamagnetic behaviour these MNPs are able to generate strong contrast effect and consequently excellent sensitivity in T_2-weighted images (T_2= spin-spin relaxation time), improving image resolution.[9,39,42] In this context, several formulations of polymer-coated/stabilized superparamagnetic nanoparticles of iron oxides (SPION) are already commercially available as MRI contrast agents, for instance Resovist® (Bayer HealthCare Pharmaceuticals, USA) or Feridex I.V.® (AMAG Pharmaceuticals Inc., USA) for liver, spleen and bone marrow imaging.[42]

1.3.2 Therapy

Concerning therapeutic applications, Fe_3O_4 MNPs offer the possibility to achieve stimuli-sensitive drug nanocarriers because of the magnetic field responsiveness typical of these nanosystems. In fact, by applying an extracorporeal magnetic field the remote magnetic focusing of the engineered Fe_3O_4 MNPs to a desired area can be achieved.[43] The simultaneous presence of active targeting agents can help facilitating the interaction with affected tissue or cell. To develop a good drug delivery system, the engineering of Fe_3O_4 MNPs is generally required; in this way high drug loading can be obtained together with the improvement of physicochemical and biological features of Fe_3O_4 MNPs, for instance their chemical stability and half-life.[38] Drug delivery systems based on engineered Fe_3O_4 MNPs or incorporating them have been developed for magnetically guided chemotherapy, radioimmunotherapy, photodynamic therapy or magnetofection.[40,44,45] Due to the opsonization phenomenon, the intravenous administration of these nanosystems limits their applicability since it leads to rapid clearance, as happened for several kinds of NPs.[46,47] A more recent strategy, known as cell-mediated delivery, consists in exploiting immune cells loaded with engineered NPs, often functionalized with drugs, for transporting and delivering

the nanosystems in the pathological area.[48] Moreover, it has been demonstrated that cells engulfed with Fe_3O_4 MNPs acquired magnetic field responsiveness.[49]

In cancer therapy, Fe_3O_4 MNPs can be exploited also for magnetic hyperthermia; this therapeutic strategy consists in killing cancer cells by exposing them to high temperatures (42-46 °C).[41,50] In this case, Fe_3O_4 MNPs represent the source of heat since they can be heated by alternating magnetic field. When Fe_3O_4 MNPs are located in the tumour area, the exposition to an external alternating magnetic field generate heat locally in the tumour, thus causing the preferential death of malignant cells. The heat production depends on several factors such as the physicochemical properties of Fe_3O_4 MNPs or their functionalization or parameters of the magnetic field. Several examples for thermal treatment of different kinds of cancer can be found in the literature.[29,51,52]

Finally, the combination of drug delivery and hyperthermia results in better therapeutic treatments while the matching of one or both of these strategies with the use in MRI imaging, make Fe_3O_4 MNPs highly powerful theranostic tools.[40,50,53,54]

1.3.3 *In vitro* diagnostics

The main applications of Fe_3O_4 MNPs in *in vitro* diagnostics concern cell labelling and separation, detection of microorganisms or biologically-relevant molecules, protein immobilization, bioanalysis and immunoassays.[12,55] For instance, the selective recognition of a specific kind of cell by Fe_3O_4 MNPs allows the further magnetic separation from a complex matrix; in this way it is possible to prepare enriched samples suitable for other analysis.[56] For performing the detection or the labelling of cells, microorganisms or other molecules, Fe_3O_4 MNPs have to be chemically modified introducing a functionality able to recognize the target. Antibodies (Ab) are very commonly used for this purpose thanks to their selective

binding capacity. In this context, several Fe_3O_4 MNPs-Ab have been developed for the *in vitro* recognition and separation of cancer cells, stem cells or pathogenic bacteria or biochemicals, such as proteins or small molecules.[57-60]

Thanks to the possible easy and quick recovery, Fe_3O_4 MNPs immobilizing enzymes or proteins have been developed without dramatically affecting the catalytic activity or the structure of the macromolecules. Moreover, the general features of NPs improve the sensitivity of these enzyme-immobilized platforms, reducing also the operational costs.[61,62] Finally, in medical and clinical diagnostics Fe_3O_4 MNPs can be used as solid support also for the immobilization of biomarkers or antibodies able to detect specific ligands. Fe_3O_4 MNPs-Ab can therefore be exploited in immunoassays, such as Enzyme Linked ImmunoSorbent Assay (ELISA) or NPs-based bio-barcode assays, or in biosensors for the detection and quantification of small molecules or biomolecules in complex biological matrices.[63-65]

2. AIM AND STRUCTURE OF THIS THESIS

2.1 Objectives and scientific strategy

The main aim of this thesis has been the development of new multifunctional superparamagnetic nanosystems for biomedical applications in the field of therapy and *in vitro* diagnostics. Starting from the favourable features of Fe_3O_4 MNPs, which make them already suitable for several purposes, the design of core-shell structured nanosystems has been accomplished to increase the potential applicability. In fact, covering the superparamagnetic core with inert and biocompatible inorganic materials leads to an increase in the chemical stability of the entire nanosystem. Moreover, in this way the surface functionalization can be easily carried out according to the chemical features of the external shell.

Two kinds of core-shell nanosystems have been firstly developed in this research work and then engineered depending on the planned end use. In fact, the introduction of other functionalities on the MNPs deriving from organic coatings, and the loading of bioactive molecules or macromolecules, like proteins or drugs, lead to the production of more efficient and specific nanosystems towards the biological targets.

Thus, the specific objectives proposed in this research work are:

- The development of core-shell nanosystems made of Fe_3O_4@Cu@Au MNPs and Fe_3O_4@SiO_2 MNPs as the starting points for the production of engineered multitasking MNPs for different biomedical applications.
- The achievement of new nanosystems loading chemotherapeutic drugs or antimicrobial compounds for therapeutic purposes and the *in vitro* evaluation of their activity on cancer cell lines or microbial cultures.
- The study of internalization of differently coated MNPs into human immune cells for contributing on investigating the therapeutic approach based on cell-mediated drug delivery.

- The development of innovative immunoassays and immunosensors involving MNPs-Ab for *in vitro* diagnostic purposes.

2.2 Thesis structure

After the brief general introduction presented in chapter 1 on MNPs for biomedical purposes, the production and physicochemical characterization of the two nanosystems Fe_3O_4@Cu@Au MNPs and Fe_3O_4@SiO_2 MNPs, on which this thesis is based, are explained in chapter 3. The several engineered nanosystems developed starting from one or both of the basic inorganic nanostructures and their *in vitro* applications are described in the following chapters.

As shown in Figure 2.2-1 the central sections of this thesis deal with:

- The development of Fe_3O_4@Cu@Au nanosystems loading the bioactive targeting molecules, folic acid and methotrexate, and the *in vitro* interaction with the human breast cancer cell lines MCF-7 and MDA-MB-231 (chapter 4).
- The coating of Fe_3O_4@Cu@Au MNPs with homo-polypeptides or proteins and the evaluation of their uptake by monocyte-differentiated macrophages (chapter 5).
- The functionalization of Fe_3O_4@SiO_2 MNPs with two bacterial secondary metabolites, syringomycin E and syringopeptin 22A, and the study of the antimicrobial activity on yeast cultures and the internalization into monocyte-differentiated macrophages (chapter 6).
- The evaluation of new immunoreagents for the detection of epinephrine by standard ELISA assays and the implementation of the diagnostic platforms using MNPs-Ab for the development of magneto-ELISAs and amperometric magneto-immunosensors (chapter 7).

- Proof-of-concept of the possibility to use MNPs-Ab as catalyst for the *in vitro* detection of epinephrine (annex).

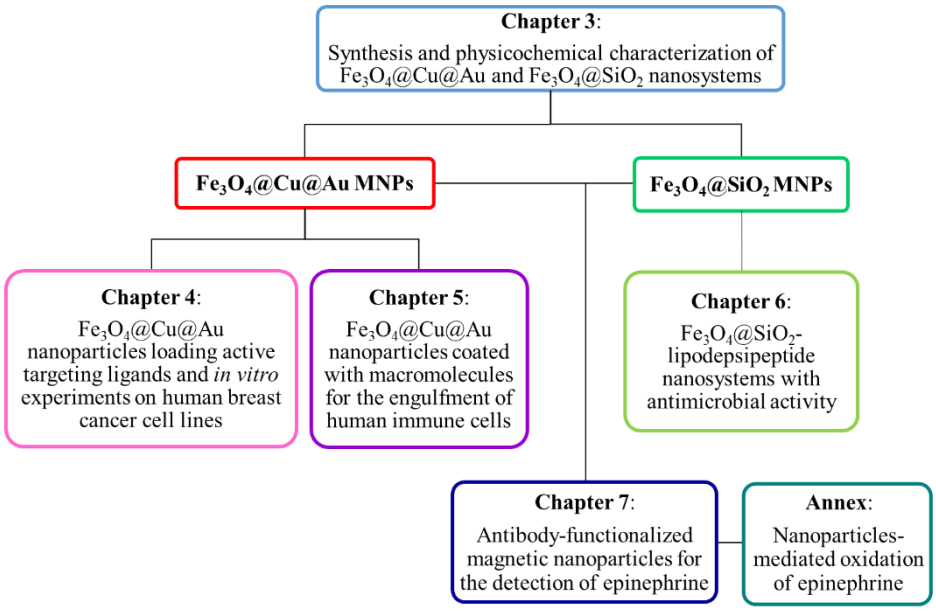

Figure 2.2-1: Structure of this thesis, starting from the synthesis of the basic nanostructures Fe_3O_4@Cu@Au MNPs and Fe_3O_4@SiO_2 MNPs (chapter 3) leading to their surface modification for the *in vitro* biomedical applications (chapters 4-7 and annex).

Conclusions of this thesis can be found in chapter 9 while the bibliography on which this research work has been supported can be found in chapter 11, after chapter 10 which includes the acronyms and abbreviations.

3. SYNTHESIS AND PHYSICOCHEMICAL CHARACTERIZATION OF Fe_3O_4@Cu@Au AND Fe_3O_4@SiO_2 NANOSYSTEMS

3.1 INTRODUCTION

This chapter deals with the development of the nanosystems used in this thesis, corresponding to Fe_3O_4@Cu@Au MNPs and Fe_3O_4@SiO_2 MNPs. The limits of using bare Fe_3O_4 MNPs, deriving from their vulnerability to oxidation and spontaneous aggregation process, can be minimized planning a core-shell structure. The ideas behind the development of these inorganic nanosystems, in addition to the synthetic processes and their physicochemical characterization are illustrated in this section.

3.1.1 Core-shell nanoparticles

The development of nanosystems with a core-shell structure extends the use of the NPs due to the improvement of some of their features.[66] This structure is characterized by the presence of an internal nucleus (core) and one or more layers made of other materials (shell). These kinds of NPs are able to greatly improve the chemical stability or biocompatibility of the material constituting the core, thus expanding their applicability in the biomedical field. The choice of the shell composition generally depends to the end use of the NP.[24]

Concerning the core-shell MNPs, Fe_3O_4 almost always constitutes the core of the system and it is enclosed inside one or more shells of organic or inorganic materials, as shown in Figure 3.1-1. The advantages of a core-shell magnetic nanostructure derive from the possibility to combine the properties of the core, in this case superparamagnetism, with other physicochemical features of the external material.[67] The outer coating preserves Fe_3O_4 from the oxidation of Fe^{2+} ions, that would alter the structure

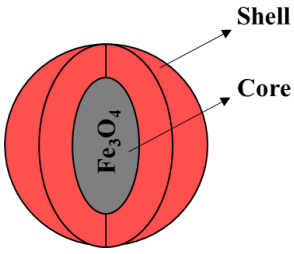

Figure 3.1-1: General scheme of a Fe_3O_4 MNPs with core-shell structure.

and thus the magnetic properties. By modulating the chemical composition of the coating, it is possible to improve the stability and dispersibility of Fe_3O_4 MNPs, also minimizing the formation of aggregates. The presence of shells made of inorganic compounds can add or enhance the properties of the entire nanosystem, such as the optical, the catalytic or the electrical ones.[37] Furthermore, by using proper coating materials the drug loading capacity or the biocompatibility of the nanosystem can be improved, facilitating the more effective interaction with biological systems and providing more powerful drug delivery systems.[68] Conversely, the presence of a coating material having peculiar properties, such as radioactivity, fluorescence or absorption, makes those nanosystems active in more than one medical diagnostic technique.[69-71] Among the materials selected for covering Fe_3O_4 MNPs, gold and silica are the most commonly used due to the chemical inertia and biocompatibility. These materials provide the stability of the MNPs in solution, limiting their spontaneous aggregation, and help to covalently bind various molecules or biomolecules suitable for the final biomedical applications.[38]

3.1.1.1 Silica shell

The chemical inertness and stability are interesting features of silica (SiO_2), making it an optimal material for covering Fe_3O_4 MNPs. Compared to the bare magnetite nanosystems, silica-coated magnetite MNPs (Fe_3O_4@SiO_2 MNPs) are much more stable in solution since the shell protects them from oxidation and limits their aggregation process; in fact, silica coating is able to shield the magnetic dipole interactions and increase the surface negative charges on Fe_3O_4 MNPs, enhancing their electrostatic repulsion.[37]

Although SiO_2 NPs, especially those made of mesoporous SiO_2 [72], are very promising materials for drug delivery or generally in nanomedicine, the combination with a superparamagnetic core offers advantages in focusing,

monitoring and revealing them during *in vivo* administration.[73] Fe_3O_4@SiO_2 MNPs can be synthesized by different procedures among which the Stöber method is the most commonly used for the achievement of an homogeneous silica shell.[74] Furthermore, the presence of a SiO_2 layer facilitates the surface modification of the Fe_3O_4@SiO_2 MNPs with heterobifunctional molecules exploitable as linkers for the conjugation of biologically relevant compounds. In fact, the presence of surface silanol groups ensures high reactivity towards alcohols or silane coupling agents through hard-hard interactions.[75] Using alkoxysilanes, such as those shown in Figure 3.1-2, the surface activation of the nanosystems with other functional groups, such as amino, thiol or epoxy groups, can be carried out allowing further functionalization.[38,76]

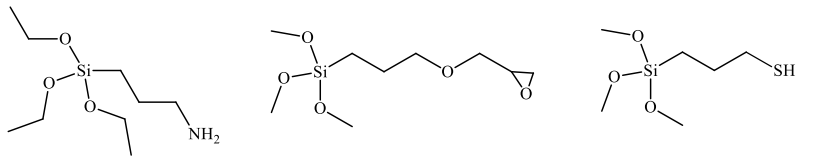

Figure 3.1-2: Chemical structure of the alkoxysilanes APTES, GPTMS and MPTMS.

3.1.1.2 Gold shell

Gold is commonly used for the coating of Fe_3O_4 MNPs since this noble metal is characterized by extraordinary optical and electronic properties, in addition to high chemical stability and biocompatibility. Thanks to those features, many research studies are focused on the applications of gold nanoparticles (Au NPs) in nanomedicine, as diagnostic or therapeutic agents for instance in biosensing or drug delivery (for more information see ref. [77,78]).

The special optical features of Au NPs are related to the phenomenon known as Localized Surface Plasmon Resonance (LSPR) which consists in the collective oscillation of the free conduction electrons due to the interaction with an

electromagnetic wave. The oscillation frequency normally occurs in the visible region and its changes can be monitored following the corresponding strong absorption band.[20] This phenomenon is very sensitive to the composition, the size, the shape and the environment of Au NPs and, for these reasons, it is commonly used for detecting and studying surface binding processes.[79] Moreover, the optical properties of Au are exploited for a promising therapeutic application for cancer therapy known as phototherapy, based on the local heating upon excitation of the surface plasmon oscillations, which can cause cancer cell death.[80]

Thus, the coating of the F_3O_4 core with an Au layer produces an enhancement of the stability and inertness of Fe_3O_4, preventing its oxidation and maintaining the superparamagnetic properties. Moreover, the presence of a Au shell gives the possibility to match the magnetic properties of the core with the optical features of Au, leading to nanosystems suitable for theranostics; for instance, NPs active at the same time in MRI, hyperthermia and photothermal therapy can be achieved.[80] In addition to the improvement of biocompatibility, the Au shell ensures the surface modification of the nanosystem via gold-thiol chemistry.[38]

3.1.1.3 Functionalization of gold shell

The Au shell offers the opportunity to easily functionalize the NPs exploiting soft-soft interactions, occurring between the soft acid Au and the soft base S.[81] This interaction leads to stable bonds (binding energy of S-Au bond = 45 kcal/mol) ensuring the covalent but quite easily breakable anchorage of different kinds of molecules.[82] The self-assembled monolayers (SAMs) of thiolate-Au can be achieved by using monothiol (RSH), thioether (RSR') or disulfide (RSSR') molecules containing alkyl or aryl groups, which general structure is reported in Figure 3.1-3. SAMs may also be made of two or more linkers with different functional groups, enabling further functionalization with several kinds of molecules and biomolecules.[83]

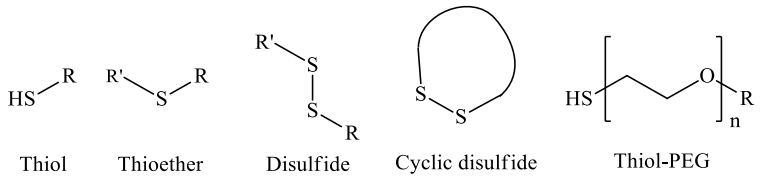

Figure 3.1-3: General structure of the organosulfur compound thiol, thioether, disulfide and cyclic disulfide. The general structure of thiol-terminated polyethylene glycol is also reported.

Thiol-terminated polyethylene glycol (thiol-PEG), which structure is shown in Figure 3.1-3, is one of the most commonly used polymeric coating for the functionalization of Au shell, since it leads to an increase of the *in vitro* and *in vivo* stability of the NPs.[84] The PEGylation of the nanosystems improves the dispersibility and the biocompatibility, avoiding the non-specific binding to protein and cells present in the vascular system during the *in vivo* administration of the NPs.[85] The use of heterobifunctional PEG molecules containing, on one side, the thiol group and, on the other side, another functional group, like amino or carboxyl group, enables to form covalent bonds with both the Au surface and other biomolecules or bioactive compounds, such as enzymes, antibodies or drugs. Mixed SAMs made of heterobifunctional-PEG molecules alternating reactive and non-reactive groups, for instance thiol-PEG containing -COOH or -OCH_3, can be a good option for the further functionalization with proteins; in fact, the reduction of the surface charge density may promote the binding of the macromolecule.[86]

The functionalization of Au surface can also be performed with short-length thiols or sulfides, for instance a heterobifunctional molecule carrying a thiol and a carboxylic acid group. In this case, choosing molecules containing a disulfide group instead of a thiol can avoid the formation of disordered and unstable structures. Moreover, cyclic disulfide can produce a more stable coating compared to acyclic disulfides since the anchorage occurs through two S atoms.[87]

3.1.1.4 Fe_3O_4@Au nanoparticles

Although several examples of Fe_3O_4@Au nanosystems can be found in the literature, the production of core-shell Fe_3O_4@Au MNPs with a uniform and homogeneous Au layer is not easy.[88,89] This problem arises from the fact that Au provides a defective and incomplete coating of Fe_3O_4; in fact, Au reacts with soft ligands while the magnetic core exposes the hard -OH groups that have low affinity for Au. For these reasons, the Au deposition on the iron oxide surface is extremely challenging since the noble metal tends to form separated NPs. The direct synthesis of core-shell Fe_3O_4@Au MNPs has been achieved by a reverse-micelle approach, which present some limitations due to low yield and poor reproducibility.[90,91]

An interesting strategy to overcome these problems and obtain a uniform coating was developed in the research group in which this thesis was carried out, depositing an intermediate Cu shell between the Fe_3O_4 core and Au layer.

3.1.1.5 Copper shell

Cu has high chemical affinity for Au, as proved by their ability to give alloys, that may guarantee the deposition of a homogeneous Au layer on Fe_3O_4 MNPs, and it can easily be deposited on magnetite surface by simple redox reactions.[92,93] Thus, the Cu layer on one hand protects Fe_3O_4 from oxidation and, on the other hand, can be exploited for the Au deposition through a direct redox reaction. Moreover, the presence of Cu enhances some physicochemical features of the nanosystems, especially in terms of catalytic ability.[94]

Therefore, the development of core-shell nanosystems made of Fe_3O_4@Cu or the production of superparamagnetic NPs loading copper ions can provide advantages in biomedical applications. In fact, nanosystems able to act as contrast agents in both MRI and positron emission tomography (PET) can be achieved using the

mixture of ^{63}Cu and the radionuclide ^{64}Cu. The integration of these techniques allows to highly improve the diagnosis of pathologies, in pre-clinical and clinical applications, since it matches the high resolution of MRI with the sensitivity of PET.[70,95]

3.2 CHAPTER OBJECTIVES

Since the central aim of this thesis is the development of new superparamagnetic nanosystems for biomedical applications, the synthesis and physicochemical characterization of the basic inorganic structures have been the first steps to address.

The nucleus made of Fe_3O_4 is the central part of two kinds of core-shell nanosystems differing in the materials that constitute the external shells. The core-shell structure has been selected in order to protect Fe_3O_4 from oxidation, maintaining its superparamagnetic features, and to improve the chemical stability and biocompatibility of the nanosystems. The choice of producing two kinds of nanosystems instead of one derives from the possibility to easily achieve different surface functionalization exploiting the specific chemical reactivity of the materials constituting the shells. In fact, selecting, from one hand, the noble metal Au and, from the other hand, the inert material SiO_2, the surface functionalization can be based on soft-soft or hard-hard interactions, respectively. In this way it is possible to covalently attach molecules bringing completely different functional groups, avoiding their derivatization, and also to modulate the strength of the bond between MNPs and surface coating depending on the biomedical end use.

The core-shell nanostructures designed and synthesized in this research work are Fe_3O_4@Cu@Au MNPs and Fe_3O@SiO_2 MNPs; the first is characterized by an intermediate shell of Cu covered by the external shell of Au while the second presents a SiO_2 shell, as shown in Figure 3.2-1.

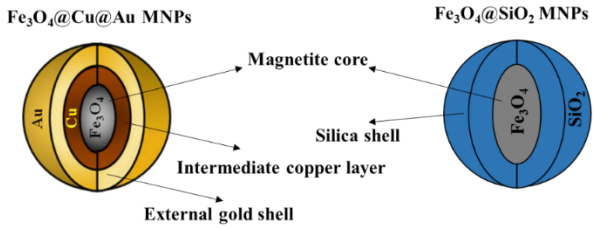

Figure 3.2-1: Schematic representation of the inorganic structure of the nanosystems developed in this thesis: core-shell Fe_3O_4@Cu@Au MNPs (on the left) and Fe_3O_4@SiO_2 MNPs(on the right).

As previously introduced, concerning Fe_3O_4@Cu@Au MNPs, the choice of Cu is due to its chemical affinity towards the -OH groups on Fe_3O_4 surface and to its redox properties which allow the further uniform deposition of Au through a direct reaction. On the other side, the production of a uniform SiO_2 shell on Fe_3O_4 is possible thanks to the high compatibility between silicon and iron oxide. In this case, the need of an intermediate layer is avoided, producing directly Fe_3O_4@SiO_2 MNPs.

The physicochemical characterization of Fe_3O_4@Cu@Au MNPs and Fe_3O_4@SiO_2 MNPs is very important to confirm their chemical nature and morphological features and to evaluate their properties. For this reason, different spectroscopic and microscopic techniques will be used to collect information about the chemical composition, the shape, the dimensions and the internal structure of those nanosystems.

3.3 RESULTS AND DISCUSSION

The experimental results concerning the synthetic strategies for the achievement of Fe_3O_4@Cu@Au MNPs and Fe_3O_4@SiO_2 MNPs and their physicochemical characterization by means of spectroscopic and microscopic techniques are presented and discussed in this section.

3.3.1 Fe_3O_4@Cu@Au MNPs

3.3.1.1 Synthesis of the core: Fe_3O_4 MNPs

The magnetic nucleus of the core-shell Fe_3O_4@Cu@Au MNPs was obtained by a modification of the synthetic protocol based on Massart's procedure.[96] As shown in Figure 3.3-1, the nucleation of Fe_3O_4 was carried out by co-precipitation method, adding dropwise a solution containing Fe^{2+}/Fe^{3+}, with a molar ratio of 1:2, to an ammonia solution at room temperature (rt).

$$2Fe^{3+} + Fe^{2+} + 8OH^- \longrightarrow Fe_3O_4 + 4H_2O$$

Figure 3.3-1: Reaction scheme for the synthesis of Fe_3O_4 MNPs by co-precipitation method.

The synthesis was performed in inert conditions to avoid the oxidation of Fe^{2+} that can lead to the formation of maghemite (γ-Fe_2O_3) instead of magnetite, modifying the magnetic properties of the MNPs.[97] This synthetic protocol was easy to perform, cost effective and quick; in fact, the addition of the iron solution in the basic environment rapidly led to the formation of black magnetic NPs.

During the synthetic step, the vigorous mechanical stirring and the use of high molar excess of the stabilizing agent polyvinylpirrolidone (PVP) allow to minimize the aggregation process normally occurring among Fe_3O_4 MNPs through the formation of μ-oxo bonds. PVP – the structure of which is shown in Figure 3.3-2 - is a water soluble and biocompatible polymer able to coordinate iron through its C=O groups, reducing the average particle size.[98] After 30 min reacting at rt, the mixture was heated at 80°C, promoting the loss of -OH surface groups involved in the aggregation processes, in order to facilitate the formation of the crystal structure in Fe_3O_4 nuclei.

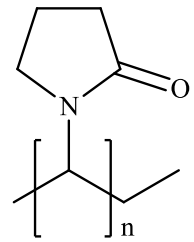

Figure 3.3-2: Chemical structure of polyvinylpirrolidone

The superparamagnetic nature of the Fe_3O_4 MNPs allows the separation from the reaction mixture through magnetic collection, carried out by applying external permanent magnets, as shown in Figure 3.3-3. Finally, to remove the unreacted reagents Fe_3O_4 MNPs were purified by dialysis against H_2O and then dried and characterized before undergoing covering steps.

Figure 3.3-3: Magnetic separation of MNPs using external permanent magnets. After few minutes from applying magnets the black solution containing MNPs (left) becomes transparent (right).

3.3.1.2 Physicochemical characterization of Fe_3O_4 MNPs

Since the development and applications of magnetic nanosystems based on Fe_3O_4@Cu@Au MNPs is the central topic of the research group led by Prof. Mario Barteri, in which this thesis was carried out, several experimental data on the physicochemical characterization of this kind of nanosystem had already been collected and/or published.[99-101]

The magnetic properties of Fe_3O_4 MNPs studied by means of vibrating sample magnetometer (VSM) were reported in a previous doctoral thesis, confirming the superparamagnetic features of these MNPs, since the measured $\mathbf{M_s}$ was of 71.6 ± 0.2 emu/g, comparable to the reference value of $\approx$ 80 emu/g.[99] The analysis performed by means of atomic force microscopy (AFM) demonstrated the nanometric dimensions and spherical shape of Fe_3O_4 MNPs, showing an average diameter of 15 nm, but also the presence of larger aggregates.

The X-ray powder diffraction (XRPD) measurements made it possible to study the crystal nature of the Fe_3O_4 MNPs. As shown in the diffractogram in Figure 3.3-4, the peaks belonging to Fe_3O_4 crystals were identified, using reference data (JCPDS file No. 88-0315), and the corresponding Miller indices were reported. The broadness of the diffraction peaks may be related to the nanometric size of the particles while the significant background noise may be due to the presence of a not-negligible portion of amorphous materials.

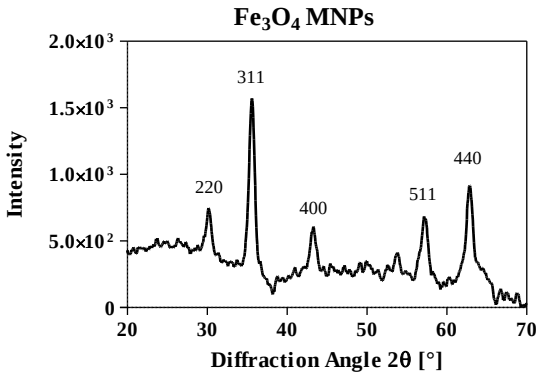

Figure 3.3-4: XRPD spectrum of Fe_3O_4 MNPs including Miller indices corresponding to Fe_3O_4.

3.3.1.3 Synthesis of the Cu shell: Fe_3O_4@Cu MNPs

Fe_3O_4 MNPs were exploited as nucleation seeds for the deposition of metallic Cu; this layer was produced by a redox reaction between a salt of Cu (II) and the reducing agent L-ascorbic acid, as reported in Figure 3.3-5.

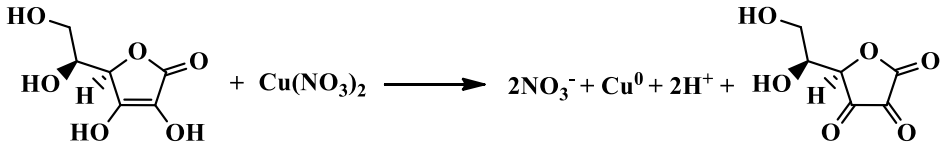

Figure 3.3-5: Scheme of the redox reaction between L-ascorbic acid and copper (II) nitrate for the deposition of the copper shell on Fe_3O_4 MNPs.

L- ascorbic acid, known as vitamin c, was used as reducing agent thanks to its peculiar features: its involvement in many metabolic pathways, both as reducing agent and coenzyme, has proven its high biocompatibility and poor cytotoxicity. Moreover, it is characterized by low cost and high-water solubility (400 mg/mL at T 40°C) and it could act at the same time as reducing agent and stabilizer, simplifying the synthetic procedure.[102] Ascorbic acid, in fact, could easily reduce Cu^{II} to Cu^0 ($E°_{Cu^{II}/Cu^0}$ = 0,34V *vs* SCE at T 25°C), being oxidized to dehydroascorbic acid ($E°_{Dehydroascorbic/ascorbic\ acid}$= 0.08V *vs* SCE at T 25°C).

The reaction was mechanically stirred for 1 h at 50 °C and Fe_3O_4@Cu MNPs were purified by dialysis against H_2O and finally dried. The same coating protocol was performed twice in order to improve the homogeneity of the Cu layer.

3.3.1.4 Physicochemical characterization of Fe_3O_4@Cu MNPs

The physicochemical characterization of Fe_3O_4@Cu MNPs was performed by means of XRPD in order to confirm the success of the deposition reaction.

XRPD spectrum, reported in Figure 3.3-6, proved the presence of Cu as Cu^0 and CuO into the nanosystems, in addition to Fe_3O_4, as shown by the diffraction peaks and the corresponding Miller indices, compared to the reference data present in the literature (JCPDS file No. 04-0836 and No. 80-1916).

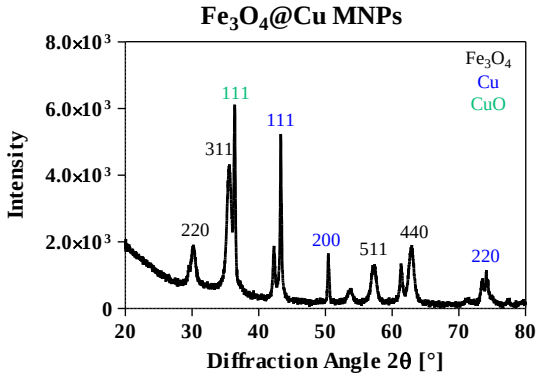

Figure 3.3-6: XRPD analysis of Fe_3O_4@Cu MNPs; The Miller indices corresponding to Fe_3O_4 (in black), Cu^0 (in blue) and CuO (in green) are indicated.

3.3.1.5 Synthesis of the Au shell: Fe_3O_4@Cu@Au MNPs

As previously described, the Cu layer in Fe_3O_4@Cu MNPs allowed the deposition of Au through a direct redox reaction between the tetrachloroauric acid, containing Au^{3+} ions, and the Cu^0 shell, as reported in Figure 3.3-7.

$$2HAuCl_4 + 3Cu^0 \longrightarrow 2Au^0 + 3Cu^{2+} + 8Cl^- + 2H^+$$

Figure 3.3-7: Scheme of the direct redox reaction between the copper shell and tetrachloroauric acid for the deposition of the Au layer on Fe_3O_4@Cu MNPs.

The Au^{3+} is characterized by a strong oxidative power ($E°_{Au3+/Au0}$ = 1.52 V at T 25°C) and it can easily react with Cu^0, consuming the copper shell and releasing Cu^{2+} in solution. It was important to neutralize the strong acidity of $HAuCl_4$, reaching pH 6,5 by adding saturated bicarbonate solution, in order to avoid the degradation and solubilization of Fe_3O_4@Cu MNPs. The reaction mixture was mechanically stirred 45 min at 60°C and, after washing with H_2O, a second coating was carried out to improve the thickness of the layer, reaching to a more homogeneous Au shell.

For the second deposition, L-ascorbic acid was used as the reducing agent thanks to its peculiar features previously described. The reaction, reported in Figure 3.3-8, was stirred for 2 h at 60°C in bicarbonate buffer solution, neutralizing the solution as previously performed, and using high excess of vitamin c.[103]

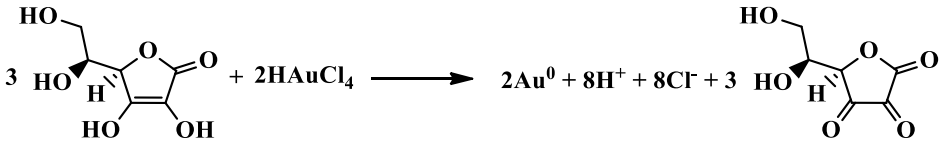

Figure 3.3-8: Scheme of the redox reaction between L-ascorbic acid and chloroauric acid for the second deposition of the gold shell on Fe_3O_4@Cu MNPs.

After magnetic separation, the Fe_3O_4@Cu@Au MNPs were purified by dialysis against H_2O, dried and characterized by spectroscopic and microscopic techniques.

3.3.1.6 Physicochemical characterization of Fe_3O_4@Cu@Au MNPs

Fe_3O_4@Cu@Au MNPs were characterized by means of XRPD, AFM and transmission electron microscopy (TEM).

The XRPD analysis proved the successful deposition of Au since several peaks in the diffractogram, reported in Figure 3.3-9, could be assigned to the noble metal, in addition to those belonging to Fe_3O_4, as confirmed by reference data (JCPDS file No. 04-0784). Moreover, the absence of diffraction peaks related to Cu, except those of its oxidized compound CuO, suggested the consumption of that shell.

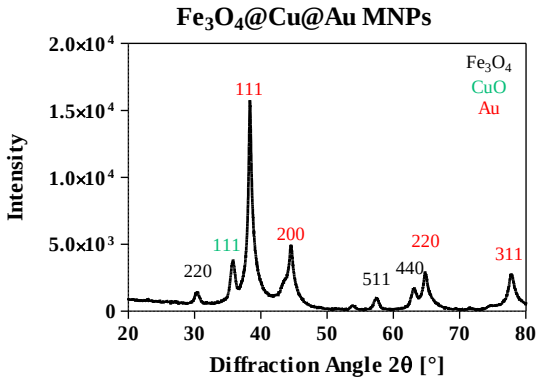

Figure 3.3-9: XRPD analysis of Fe_3O_4@Cu@Au MNPs; Miller indices belonging to Fe_3O_4 (in black), CuO (in green) and Au (in red) are reported.

The characterization of Fe_3O_4@Cu@Au MNPs by means of the microscopic technique AFM and TEM confirmed the spherical shape of the nanosystems and their nanometer dimensions. In fact, according to the images shown in Figure 3.3-10, the average diameter of Fe_3O_4@Cu@Au MNPs was estimated of 20 nm and the evidence of a core-shell structure was obtained. Aggregates having nanometric and micrometric dimensions were also detected.

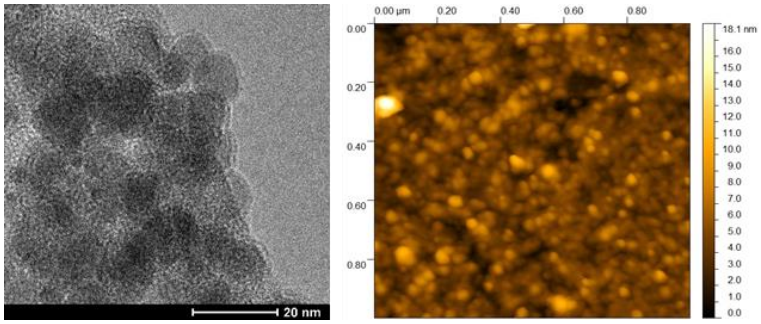

Figure 3.3-10: TEM (on the left) and AFM (on the right) analysis of Fe_3O_4@Cu@Au MNPs, confirming the nanometer dimension and the core-shell structure of the nanosystems.

3.3.2 Fe_3O_4@SiO_2 MNPs

In order to produce the other kind of nanosystem, Fe_3O_4 MNPs were exploited as nucleation seeds for the deposition of SiO_2 shell. As previously described in section 3.1.1.1, SiO_2 was selected as the coating agent because of its excellent biocompatibility and chemical stability. Moreover, the surface functionalization of Fe_3O_4@SiO_2 MNPs could be carried out taking advantages from the strong hard-hard interactions among silicon and other compounds, especially silanes; using heterobifunctional silanes the conjugation of molecules or biomolecules of interest can be achieved.[104]

3.3.2.1 Synthesis of silica shell: Fe_3O_4@SiO_2 MNPs

The deposition of the SiO_2 shell on Fe_3O_4 MNPs was carried out by the sol-gel process, known as Stöber method.[74] This synthetic strategy concerned the polymerization of tetraethoxysilane (TEOS) in alcohol solution using ammonia as catalyst, as reported in Figure 3.3-11.

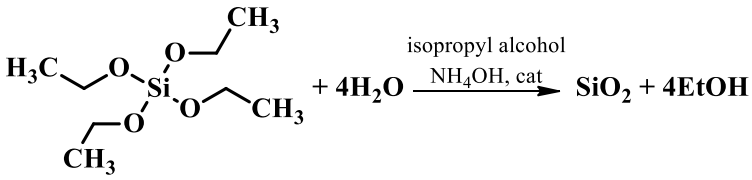

Figure 3.3-11: Scheme of the polymerization reaction of TEOS for the deposition of SiO_2 shell on Fe_3O_4 MNPs.

The reaction was performed stirring Fe_3O_4 MNPs for 3 h at rt in TEOS solution. The mechanism consists in the hydrolysis of TEOS in isopropyl alcohol followed by the condensation step on the surface of Fe_3O_4 MNPs, leading to the formation of the SiO_2 shell. Fe_3O_4@SiO_2 MNPs were separated from the reaction mixtures through magnetic collection, washed several times first with alcohol and then with H_2O and finally dried. Two kinds of Fe_3O_4@SiO_2 MNPs differing in the thickness of the shell were synthesized; these MNPs were produced performing the reactions with different amounts of TEOS, using three-times the concentration of TEOS in one reaction compared to the other.[105]

3.3.2.2 Physicochemical characterization of Fe_3O_4@SiO_2 MNPs

Fe_3O_4@SiO_2 MNPs were characterized by means of spectroscopic and microscopic techniques. The chemical characterization was achieved performing Fourier-transform infrared spectroscopy (FT-IR) and XRPD analysis while the morphological study was carried out by using AFM and TEM.

The FT-IR spectrum of Fe_3O_4@SiO_2 MNPs, shown in Figure 3.3-12, confirmed the presence of silica in the inorganic nanostructure in addition to the iron oxide since the typical vibrational bands of SiO_2 and Fe_3O_4 could be clearly recognized. In fact, the intense vibrational bands centred at $\nu \approx 1067$ cm^{-1} and $\nu \approx 587$ cm^{-1} could be assigned to the stretching vibrations of Si-O-Si and Fe-O bond, respectively. The broad band at $\nu \approx 3430$ cm^{-1} and that at $\nu \approx 1630$ cm^{-1} could, instead, be ascribed to the O-H vibrations of adsorbed H_2O.

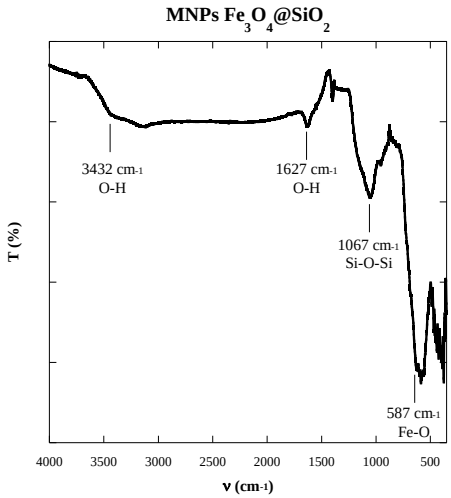

Figure 3.3-12: FT-IR spectrum of Fe_3O_4@SiO_2 MNPs, highlighting the typical vibrational bands belonging to O-H, Si-O-Si and Fe-O bonds.

The XRPD spectrum of Fe_3O_4@SiO_2 MNPs, shown in Figure 3.3-13, suggested the presence of SiO_2 in an amorphous state. This consideration derived from the increase in the non-crystalline portion of the material, which caused high background at diffraction angles < 30°, and in the contemporary absence of diffraction peaks corresponding to SiO_2 crystals. The diffraction peaks belonging to Fe_3O_4 were, instead, identified by the corresponding Miller indices.

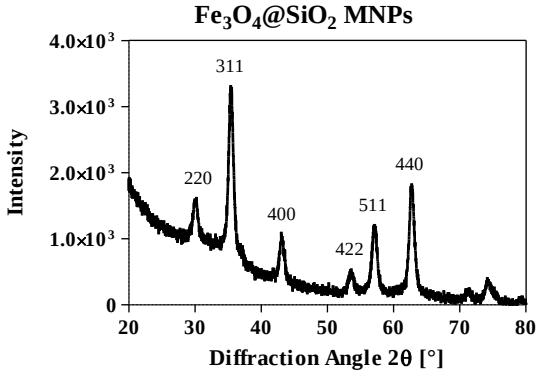

Figure 3.3-13: XRPD analysis of Fe_3O_4@SiO_2-MNPs; SiO_2 was present in an amorphous state while the diffraction peaks belonging to Fe_3O_4 were identified by the corresponding Miller indices.

The AFM image, shown in Figure 3.3-14, proved the spherical shape and the nanometric dimensions of Fe_3O_4@SiO_2 MNPs; the average diameter was estimated of 20 nm but aggregates with larger dimensions were found.

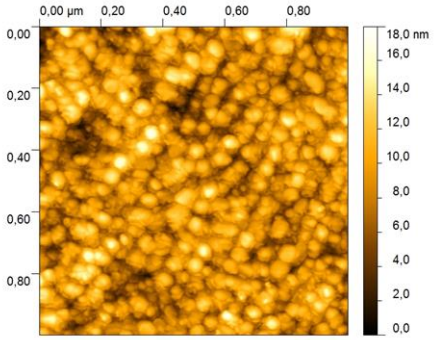

Figure 3.3-14: AFM image of Fe_3O_4@SiO_2 MNPs, confirming the spherical shape and nanometric dimensions.

The analysis of Fe_3O_4@SiO_2 MNPs by means of TEM confirmed these morphological features and allowed also to appreciate the internal structure. The comparison among the TEM images corresponding to the bare Fe_3O_4 MNPs (A) with those of the coated Fe_3O_4@SiO_2 MNPs synthesized using the lowest (B) or the highest (C) quantity of TEOS is reported in Figure 3.3-15. All the samples were not well dispersed and presented aggregates. The core diameter was estimated around 10-15 nm, in agreement with the AFM analysis. Concerning the coating reactions, Fe_3O_4@SiO_2 MNPs sample B, obtained using the less concentration of TEOS, had comparable dimensions and similar appearance to Fe_3O_4 MNPs, since the presence of the SiO_2 shell was not detected. Conversely, the core-shell structure was clearly identifiable in the nanosystems synthesized using high amount of TEOS, Fe_3O_4@SiO_2 MNPs sample C; in this sample the presence of materials with diverse electron densities producing different contrast in the image, such as silicon and iron, was evident. As shown in Figure 3.3-16, the thickness of the SiO_2 shell in these MNPs was estimated of 8 nm.

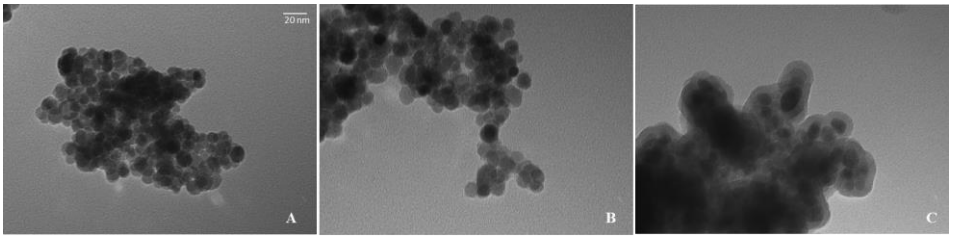

Figure 3.3-15: TEM images corresponding to Fe_3O_4 MNPs (A) and Fe_3O_4@SiO_2 MNPs synthesized using the lowest (B) or the highest (C) quantity of TEOS. Samples A and B were comparable while the core-shell structure was detectable in sample C.

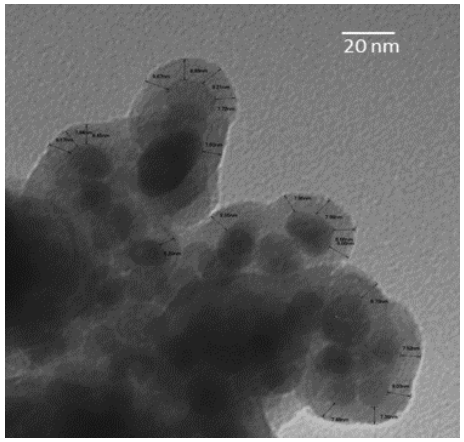

Figure 3.3-16: TEM image of Fe_3O_4@SiO_2 MNPs sample C reporting the experimental measures of the silica shell thickness.

Since the experimental data highlighted the core-shell structure in the sample corresponding to Fe_3O_4@SiO_2 MNPs synthesized with the high concentration of TEOS, only these nanosystems were selected for the further functionalization and biomedical applications.

3.4 CHAPTER CONTRIBUTIONS

- Core-shell superparamagnetic Fe_3O_4@Cu@Au MNPs and Fe_3O_4@SiO_2 MNPs were synthesized and characterized by means of different spectroscopic and microscopic techniques. The chemical composition and the crystal structure were confirmed by XRPD and/or FT-IR analysis while data about the nanometric dimensions, shape and internal structure were collected by AFM and TEM analysis.

3.5 ACKNOWLEDGMENTS

Dr. Alessandro Latini and Dr. Carmen Cavallo of Sapienza University of Rome for XRPD. Dr Francesca Anna Scaramuzzo of Sapienza University of Rome for AFM. Dr. Sergio Brutti of University of Basilicata for TEM. Prof. Maria Pia Donzello of Sapienza University of Rome for FTIR.

3.6 MATERIALS AND METHODS

Reagents, materials and equipment: All the chemical reagents were purchased by Sigma-Aldrich (Merck KGaA, Darmstadt, Germany) and used without further purification. Permanent magnets made of Neodymium-Iron-Boron alloy, having a magnetic field of 0.3 T, were used for magnetic separations. Sonication was performed with UNISET-AC characterized by 45 W power and 38 KHz maximum frequency. The diffractometer RIGAKU-MINIFLEX II, with a θ-2θ Bragg-Brentano geometry and Cu anti-cathode (Cu $K_{\alpha 1}$ λ= 1.5405 Å), was used for XRPD analysis on solid MNPs. Infrared spectra were recorded from 200 to 4000 cm^{-1} using the spectrometer VARIAN 660-IR FT-IR and preparing the IR tablets

mixing 1 mg of sample with 200 mg of anhydrous KBr. AFM analysis were performed using the microscope MULTIMODE VEECO equipped with the software Nanoscope IIIa; the topographical images of the sample, deposited as diluted aqueous solution on Si slices, were collected in tapping mode using a RTESP Bruker tip (nominal parameters r = 8mm, f = 300 kHz, k = 40 N/m) and recorded with a 512x512 pixel resolution, corrected by polynomial background filters using the software Gwyddion 2.31. TEM images were collected with the microscope Philips ECM-200 KV.

Synthesis of the magnetite core - Fe_3O_4 MNPs: 200 mL of an aqueous solution containing $(NH_4)_2Fe(SO_4)_2$*$6H_2O$ (3.8 mmol), $Fe_2(SO_4)_3$ (3.8 mmol) and PVP (MW 10 000, 19.1 mmol) were added dropwise in argon atmosphere to 600 mL of NH_4OH (0.7 M) dissolving the same amount of PVP. After 30 min reacting at rt under mechanical stirring, the mixture was heated at 80°C and stirred 30 min. Once cooled, Fe_3O_4 MNPs were magnetically separated from the mixture and dialyzed 24 h against bi-distilled H_2O. After drying under vacuum, about 700 mg of Fe_3O_4 MNPs were obtained.

Synthesis of the Cu shell - Fe_3O_4@Cu MNPs: 100 mg of Fe_3O_4 MNPs (0.43 mmol) were dispersed in 48 mL of bi-distilled H_2O and sonicated 10 min. The molar ratio between Fe_3O_4 : Cu^{II} used was 1.5:1. 10 mL of an aqueous solution of $Cu(NO_3)_2$ (0.29 mmol) and, after 5 min, 2 mL of an aqueous solution of L-ascorbic acid (0.58 mmol) were added dropwise to the dispersion. The reaction was mechanically stirred for 1 h at 50°C. Fe_3O_4@Cu MNPs were magnetically separated, washed with bi-distilled H_2O and then used for the second covering.

The second covering reaction was performed as the previous one, using the same amount of L-ascorbic acid and changing the molar ratio between Fe_3O_4 and Cu^{II} to 4:1. After 1 h stirring at 50°C, the product Fe_3O_4@Cu MNPs was washed with saturated NaCl solution and then dialysed 24 h against bi-distilled H_2O and finally dried in the stove overnight at 120°C.

Synthesis of the Au shell - Fe_3O_4@Cu@Au MNPs: 100 mg of Fe_3O_4@Cu MNPs (0.82 mmol of Cu) were dispersed in 45 mL of bi-distilled H_2O. 5 mL of a aqueous solution of $HAuCl_4*3H_2O$ (0.21 mmol), neutralized to pH 6.5 with saturated $NaHCO_3$ solution, were added dropwise to the dispersion. The mixture was mechanically stirred for 45 min at 60°C. Fe_3O_4@Cu@Au MNPs were magnetically separated from the mixture, washed with saturated $NaHCO_3$ solution and then bi-distilled H_2O and finally covered with the second Au shell.

For the second gold deposition reaction, Fe_3O_4@Cu@Au MNPs achieved from the first covering reaction were dispersed in 43 mL of bi-distilled H_2O and 5 mL of a neutralized aqueous solution of $HAuCl_4*3H_2O$ (0.10 mmol, pH 6.5) were added to the dispersion. After adding 2 mL of an aqueous solution of L-ascorbic acid (0.50 mmol) the mixture was mechanically stirred at 60°C for 2 h. Fe_3O_4@Cu@Au MNPs were collected by magnetic separation, washed with EDTA solution (1 mM; pH 7) and then dialysed 24 h against bi-distilled H_2O. Fe_3O_4@Cu@Au MNPs were desiccated overnight in the stove at 120°C.

Synthesis of the SiO_2 shell - Fe_3O_4@SiO_2 MNPs: 100 mg of Fe_3O_4 MNPs were dispersed in 6 mL of bi-distilled H_2O and sonicated for 15 min. Under mechanical stirring, 20 mL of a solution of TEOS in isopropyl alcohol (at the concentration of 1 mg/mL or 2,5 mg/mL) and 1 mL of NH_4OH (0.7 M) were added slowly to the dispersion. After reacting 3h at rt, Fe_3O_4@SiO_2 MNPs were magnetically separated from the solution, washed with isopropyl alcohol and bi-distilled H_2O and then dried overnight under vacuum.

4. Fe_3O_4@Cu@Au NANOPARTICLES LOADING ACTIVE TARGETING LIGANDS AND *IN VITRO* EXPERIMENTS ON HUMAN BREAST CANCER CELL LINES

4.1 INTRODUCTION

The development of new nanosystems suitable for theranostic applications in cancer treatment is the focus of the research work presented in this chapter. The basic metallic structure of Fe_3O_4@Cu@Au MNPs has been used for the conjugation of bioactive molecules also known to be active targeting ligands, like the vitamin folic acid and the chemotherapeutic drug methotrexate. To reach this goal, the preliminary activation of the Au surface with molecules suitable for the further modification has been carried out. To evaluate the therapeutic effect of the synthesized nanosystems, biological studies on breast cancer cell lines have been performed in collaboration with the research group led by Prof. Laura Masuelli at the Department of Experimental Medicine - Sapienza University of Rome.

4.1.1 Tumour targeting using nanosystems

Since the spread of cancer is rapidly increasing, causing millions of deaths worldwide, the development of new therapeutic strategies based on NPs and the improvement of the imaging techniques can contribute to early diagnosis and more efficient treatments, preventing the lethal outcomes of cancer.[106-108] Several kinds of nanoparticles, especially liposomes and polymeric nanoparticles, have already been approved or submitted to clinical trials for the treatment of several primary tumours and/or metastasis: for instance Myocet® (Sopherion Therapeutics Inc., USA), non-PEGylated liposomes loading Doxorubicin, or NK105, PEG-poly(aspartic acid) carriers loading Paclitaxel (Phase III)[109] have been proposed for the treatment of breast cancer.[107]

Fe_3O_4 MNPs can also be useful for cancer therapy and imaging, as previously described in section 1.3. In addition to their exploitation as contrast agents in MRI or in hyperthermia, Fe_3O_4 MNPs can be functionalized in order to carry proper

molecules with pharmaceutical or targeting activity, such as anti-cancer drugs or proteins. A great advantage of engineered Fe_3O_4 MNPs, compared to other modified NPs, comes from the magnetic core which offers the possibility to remotely focusing them in the pathological area by using external magnetic fields.[110]

Generally in cancer therapy two different strategies can be used to increase the accumulation of nanocarriers into tumours.[111] They are known as passive and active targeting and their general mechanism is shown in Figure 4.1-1 from ref [112].

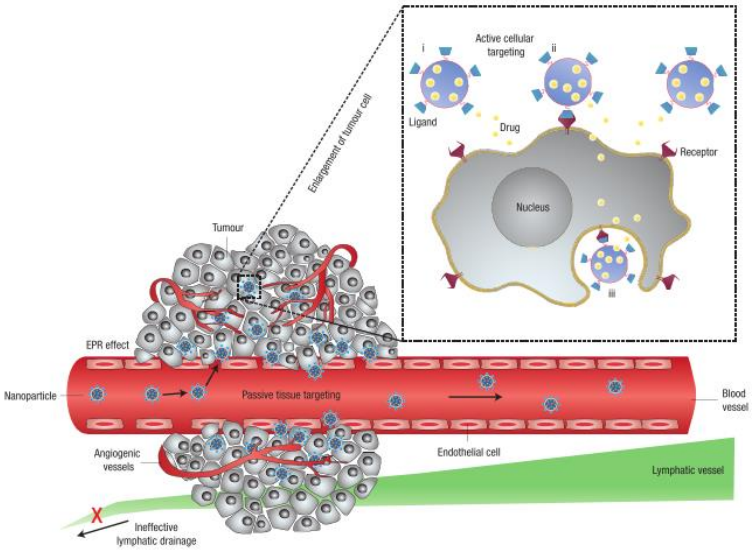

Figure 4.1-1: Schematic representation of passive and active targeting strategies for accumulating nanoparticles in tumours (from ref. [112]). The passive targeting consists in exploiting the enhanced permeability and retention effect of the tumoural mass due to ineffective lymphatic drainage and fenestrations in blood vessels of the affected tissue. The active targeting involves the use of active targeting ligands or specific antibodies which can address the nanosystems preferentially to malignant cells.

Since the tumoral mass needs oxygen and other nutrients to support its intense growth, the generation of new vasculature structures rapidly occurs. The speed of this process, defined as angiogenesis, leads to the formation of imperfect and irregular blood vessels which are characterized by a reduced density of endothelial cells and large gaps among them. In addition to the poor and defective lymphatic

drainage of the tumoral area, these fenestrations allow the passive diffusion of nanomaterials into the pathological area. This phenomenon is known as Enhanced Permeation and Retention effect (EPR) and is commonly exploited for improving accumulation of nanocarriers into tumoral tissue, providing an increase in the local distribution of drugs.[111,113] However, EPR cannot be exploited for all kinds of tumours since it depends on several features, such as the position and the size of the tumour or the pore dimensions of the fenestrations; for instance, tumours presenting necrotic areas characterized by hypoxic environment cannot be reached by exploiting this passive accumulation phenomenon and, moreover, EPR is often compromised by the increased intratumor pressure.[114]

The use of specific ligands for cancer cell which can act as targeting molecules can help overcoming the limitations of the passive drug-delivery strategy.[115] The active targeting compounds include specific antibodies, proteins, nucleic acids, peptides or other small molecules such as vitamins. They can actively interact with some elements, such as surface molecules or receptors, present in the affected organ, tissue or cell. Thanks to this specific interaction, the drug delivery nanosystems loading active targeting ligands are preferentially directed to the pathological tissues, enabling a more efficient therapeutic activity. Furthermore, if the active targeting concerns a membrane receptor able to trigger the internalization process and that is overexpressed in cancer cells, the uptake of the functionalized nanosystem can be facilitated.[116] Some examples of active targeting molecules are antibodies or their fragments consisting in the hypervariable region, proteins such as transferrin, peptides with RGD sequence (arginine-glycine-aspartic acid) or vitamins like folic acid.[117,118]

4.1.2 Folic acid and methotrexate

Folic acid (FA) is an essential vitamin belonging to the B group (vitamin B9). As shown in Figure 4.1-2, a pteridine ring (in black), a p-aminobenzoic acid moiety (PABA, in red) and a γ- glutamic acid residue (γ-Glu, in blue) compose its chemical structure. In nature it can be found in several forms differing in the oxidation state of the pteridine ring, or in the N(5) or N(10) substituents or in the number of glutamate residues; all these compounds belong to the folate family. Folates are converted by the enzyme dihydrofolate reductase (DHFR) in the active form tetrahydrofolate (THF), using NADPH as cofactor. THF acts as coenzyme in many biochemical processes concerning the one-carbon transfer at different oxidation state, for example in the metabolism of purine, pyrimidines and some AA. Due to its biological importance, a deficiency of FA is correlated to pathologies affecting especially nervous system, such as spina bifida.[119]

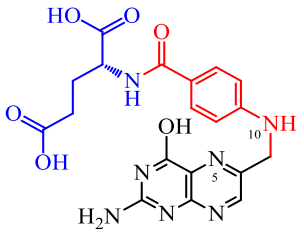

Figure 4.1-2: Chemical structure of folic acid; the pteridine ring, the p-aminobenzoic acid and the γ-glutamic acid residue are highlighted respectively in black, red and blue.

Due to the involvement of DHFR in cell growth, several chemotherapeutic drugs have this enzyme as their biological target. Among those, methotrexate (MTX) is a folate structural analogue since -NH_2 group is present in the pteridine ring instead of -OH and -CH_3 instead of -H in the PABA moiety, as shown in Figure 4.1-3. These structural differences allow MTX to act as antagonist of FA (antifolate), binding to the active site of DHFR and inhibiting it.[120] This process leads to a leakage of THF, blocking the nucleic acid synthesis and causing cell death. Due to its cytotoxic activity, MTX is commonly used for the treatment of several kinds of cancer, especially lung and breast cancer.[121,122]

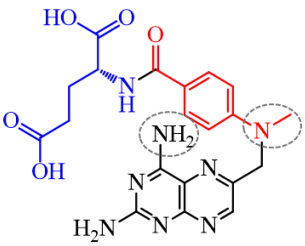

Figure 4.1-3: Chemical structure of methotrexate; the pteridine ring, PABA and γ-Glu are highlighted in black, red and blue respectively, while the substituents differing from FA are circled.

4.1.3 Folate receptors and cancer cells

The need of FA occurs particularly in rapidly dividing cells, including cancer cells, and for this reason the antifolates are of great interest in cancer therapy. In this context, the sensitivity of some cancer cell lines to antifolate drugs derives from the overexpression of folate receptors on their cellular membranes, needed for allowing high uptake of FA to support their rapid growth.[123]

The absorption of folates occurs in the intestinal villi thanks to specific folate transporters: folate receptors (FRs), reduced folate carriers (RFC) and proton coupled folate transporters are involved in this mechanism.[124] Folate receptors are trans-membrane proteins anchored by glycosylphosphatidylinositol molecules, existing in different isoforms and showing nanomolar binding affinity for FA. The α isoform of FRs (α-FR) has become an important tumoral marker since it is overexpressed in many tumours affecting especially brain, liver, ovary and breast.[125] Although it is mainly present in macrophages, it is almost absent or hardly accessible in healthy organs, such as liver, lung and placenta. Moreover, the amount of folate receptors seems to increase during the worsening of the stage of the cancer.[126] This protein is thus becoming an interesting biological target for the selective treatment of some tumours.[123] Because of the high structural similarity between FA and MTX, this drug is able to bind to RFC and FR with lower affinity than FA but entering into the binding site with the identical geometry and orientation of FA.[127]

Once bound FA or an antifolate, the folate receptors transport the ligand in intracellular environment by a receptor-mediated endocytosis. As shown in Figure 4.1-4 from ref. [128], after the receptor-ligand complex formation the internalization occurs through the intracellular compartment called endosome. The endosome acidification produces the detachment of the folate from the protein, since the binding is pH dependent and, consequently, its release in the cytoplasmic environment together with the recycling of the receptor.[128]

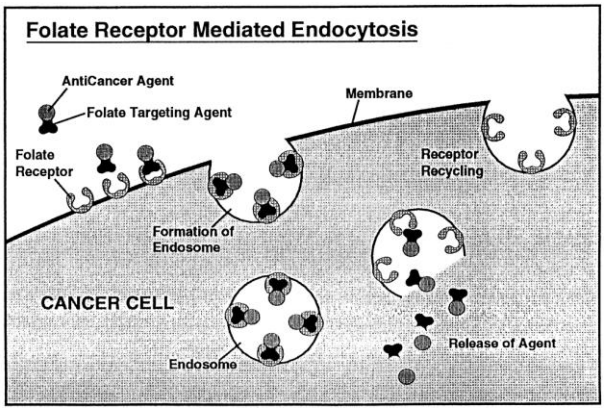

Figure 4.1-4: Mechanism of the folate receptor-mediated endocytosis exploited as active targeting strategy in cancer treatment (from ref. [128]). The interaction between the folate-loaded system and the membrane folate receptors triggers the internalization process which starts with the production of the endosomes. Once reached the cytoplasm, the acidification of the endosome causes the intracellular release of the folate-functionalized system and the recycling of the folate receptors.

However, some cancer cells often show resistance to antifolate drug since they are able to develop a defence mechanism, such as the amplification of the gene encoding for DHFR or the decrease in the receptor-mediated transport mechanism.[129] To better exploit the promising features of folate active targeting, the conjugation of FA or antifolates to nanocarriers seems to be a good strategy; in fact, combining the peculiar features of NPs with those of folates the accumulation of the nanosystems in targeted tissues can be improved together with the internalization into malignant cells.[118] In this way, the nanosystems can be able to perform a more selective cytotoxic action limiting the side effects on healthy tissues. Several metal and polymeric nanosystems have been synthesized loading FA for targeting cancer cells [130,131] or loading MTX and using it both as targeting and therapeutic agent.[127,132] Examples of MNPs functionalized with FA or MTX for cancer theranostics can be found in the literature, generally exploiting the magnetic core for MRI or performing multimodal strategies.[54,133]

The design and development of new nanosystems able to overcome the cellular defence strategies, exploiting the active targeting ability of FA or MTX and being effective in cancer treatment remain interesting research topics.

4.2 CHAPTER OBJECTIVES

Due to the interesting features of the bioactive molecules FA and MTX in directing a nanosystem preferentially to cancer cells, the development of Fe_3O_4@Cu@Au MNPs loading those molecules is the topic of this chapter. This section represents a continuation of a previous research work reported in ref. [99], carried out in the same research group, demonstrating the internalization of the same nanosystems into human granulocytes and human breast cancer cell lines. The optimization of the synthetic protocol, the quantification of the loaded bioactive molecule and the evaluation of the cytotoxic effects on the cancer cell lines remained unsolved topics which have to be investigated.

To engineer Fe_3O_4@Cu@Au MNPs, the activation of the Au surface by soft-soft interactions with the vitamin lipoic acid can be a good strategy to allow the further binding of the cationic homopolymer poly-L-Lys; in this way the conjugation of the vitamin or the drug can be easily achieved. The synthesis and physicochemical characterization of the nanosystems, shown in Figure 4.2-1, are the main objectives of this work. These nanoplatforms can represent multitasking nanosystems suitable for theranostic application due to the contemporary presence of different functionalities; in addition to the magnetic core, active in focusing and revealing the nanosystems by magnetic-based techniques, the specific features of the bioactive molecules can allow their use as drug delivery systems, targeting cancer cells in a more selective way.

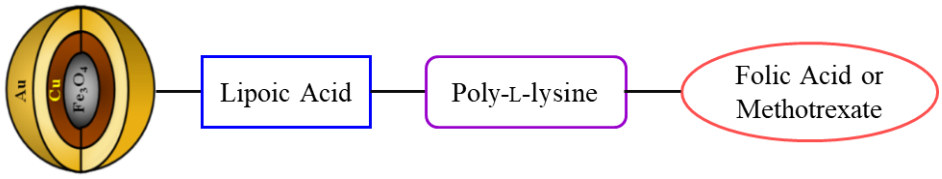

Figure 4.2-1: Schematic representation of Fe_3O_4@Cu@Au MNPs loading the bioactive molecules folic acid or methotrexate thanks to the activation of their surface with lipoic acid and poly-L-lysine.

Moreover, the performance of biological experiments on cancer cell lines can help understanding the real applicability of those nanosystems; for this reason, *in vitro* experiments on the human breast cancer cell lines MCF-7 and MDA-MB-231, shown in Figure 4.2-2, can give information concerning the cytotoxic effects of the developed nanosystems.

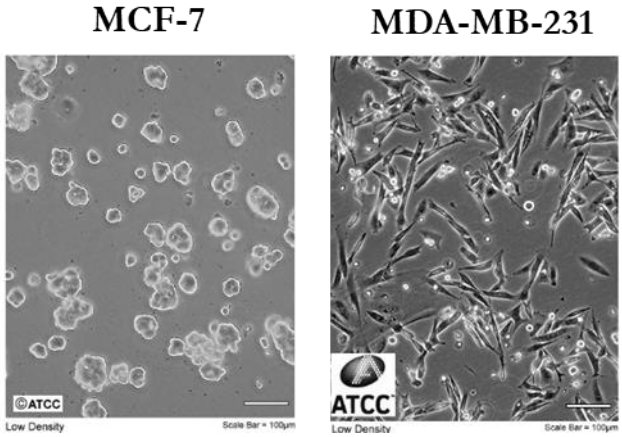

Figure 4.2-2: Images of the breast cancer cell lines MCF-7 and MDA-MB-231 (from ATCC) selected for the *in vitro* biological experiments.

4.3 RESULTS AND DISCUSSION

In this section the development of Fe_3O_4@Cu@Au nanosystems functionalized with FA or MTX is described, including the intermediate activation steps with the vitamin lipoic acid, and the homopolymer poly-L-lysine. The study of the interactions among the synthesized nanosystems and the breast cancer cell lines, MCF-7 and MDA-MB-231, is also reported and discussed.

4.3.1 Functionalization with lipoic acid

In order to achieve nanosystems active in theranostics, the Fe_3O_4@Cu@Au MNPs were activated with a heterobifunctional compound able to bind the surface of the nanoplatforms and allow the further conjugation of molecules or biomolecules.

Lipoic acid (LA) was selected to play this role of linker thanks to its chemical and biological features. As shown in Figure 4.3-1, the disulfide bond could interact with the Au surface, according to the Au-S chemistry, while the -COOH group could be exploited for the further conjugation of other molecules. Moreover, LA showed high biocompatibility since it is involved in many biochemical pathways concerning the transfer of acyl group. It acts as cofactor of important enzymes, such as the pyruvate dehydrogenase multi-enzyme complex, and it plays an antioxidant role by contrasting reactive oxygen species and chelating heavy metals.[134]

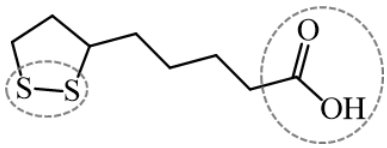

Figure 4.3-1: Chemical structure of lipoic acid in which the disulfide bond and the carboxyl group are highlighted.

4.3.1.1 Esterification of lipoic acid

LA was previously derivatized in a more reactive form by an esterification reaction on the -COOH group, as shown in Figure 4.3-2, introducing a good leaving group for the subsequent reactions. After reacting 24h at rt with N,N'-Dicyclohexylcarbodiimide (DCC) and N-hydroxysuccinimide (NHS) in DCM, the reaction mixture was filtered to remove the coproduct dicyclohexylurea. The NHS-lipoate was purified by crystallization using the mixture ethyl acetate : hexane – 1:1, as reported in the literature [135], and obtaining the product with 61% yield as yellow crystals needles-shaped.

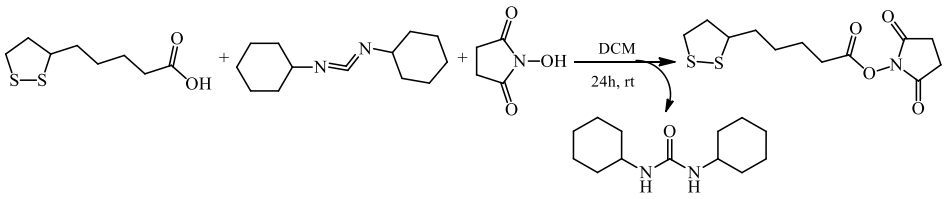

Figure 4.3-2: Scheme of the esterification reaction of lipoic acid using DCC and NHS.

4.3.1.2 Anchorage on Fe_3O_4@Cu@Au MNPs: MNPs-LA-NHS

The NHS-lipoate was used for the anchorage on Fe_3O_4@Cu@Au MNPs, mechanically stirring overnight the nanosystems in the ester solution in ethyl acetate, as reported in Figure 4.3-3.

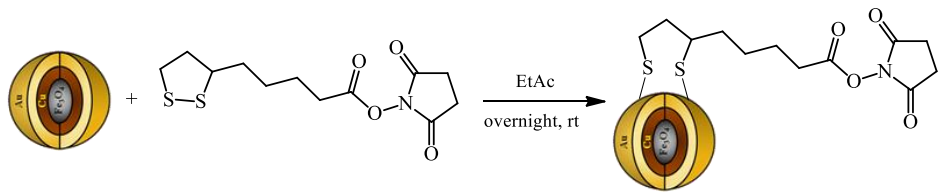

Figure 4.3-3: Reaction scheme of the anchorage of NHS-lipoate on Fe_3O_4@Cu@Au MNPs.

The reaction was monitored by UV-Vis spectroscopy, comparing the spectra recorded before (start - dashed line) and after (stop - solid line) the reaction with

Fe_3O_4@Cu@Au MNPs, that were magnetically separated from the reaction mixture. As shown in Figure 4.3-4, the decrease in the intensity of the absorption band centred at λ 334 nm, corresponding to lipoate, after the reaction with MNPs confirmed the anchorage of NHS-LA on Au surface.

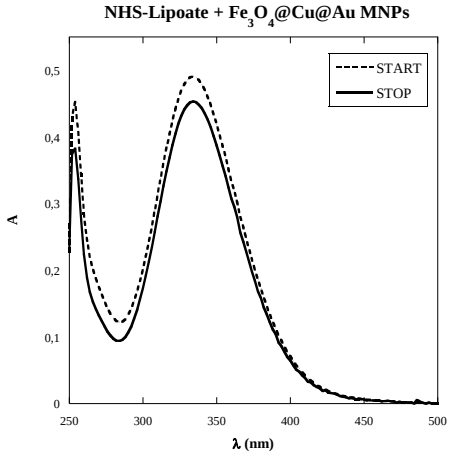

Figure 4.3-4: UV-Vis spectra recorded before (start, dashed line) and after (stop, solid line) the reaction between NHS-lipoate and Fe_3O_4@Cu@Au MNPs, confirming the anchorage of the linker.

The nanosystems Fe_3O_4@Cu@Au-Lipoate-NHS MNPs, referred to as MNPs-LA-NHS, were washed, dried and used for the further conjugation reactions.

4.3.2 Functionalization with poly-L-lysine

The homopolymer poly-L-lysine (PLL), which structure is shown in Figure 4.3-5, was selected for the binding of FA and MTX due to the presence of several amine groups exploitable for the drug conjugation. Moreover, these groups were suitable for the anchorage on nanosystems, through the reaction with NHS-lipoate, or for the labelling with a fluorescent probe. Furthermore, the hydrophilic and cationic

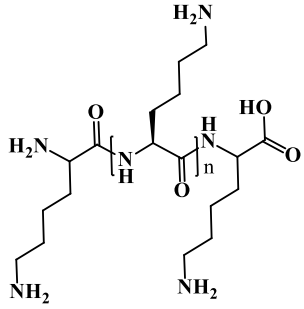

Figure 4.3-5: Chemical structure of poly-L-lysine.

nature of PLL can enhance the dispersibility of nanoparticles in aqueous solution.[136] The presence of the polymer on nanosystems or in simple drug-PLL conjugates can improve the interactions with cell membranes and the absorption of the bound drug.[137,138]

4.3.2.1 Anchorage on MNPs-LA-NHS: MNPs-PLL

The activated carboxyl groups of LA on MNPs-LA-NHS were used for the reaction with the nucleophilic -NH_2 groups of PLL, leading to the formation of amide bonds. As shown in Figure 4.3-6, the reaction was performed in bicarbonate buffer since the slightly basic pH was selected as a compromise among deprotonating the amine groups and minimizing the hydrolysis of the active ester.

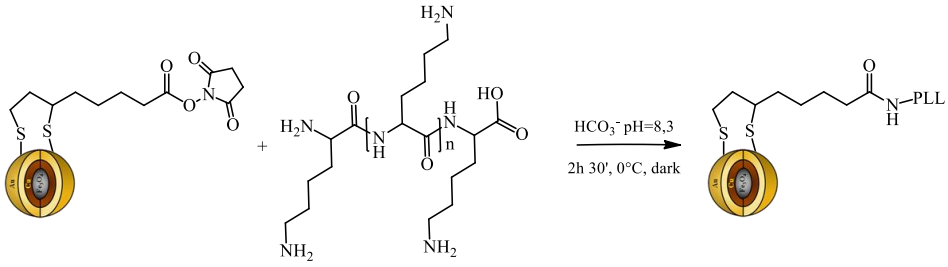

Figure 4.3-6: Reaction scheme of the functionalization of MNPs-LA-NHS with PLL.

The reaction was monitored by UV-Vis spectroscopy to confirm the conjugation (data not shown). UV-Vis spectra were recorded before and after the reaction between MNPs-LA-NHS and PLL; the increase in the absorption band at λ_{max} 270 nm and the decrease in that at λ_{max} 220 nm, belonging to NHS and PLL, in the sample corresponding to the supernatant after the reaction with the nanosystems proved the PLL anchorage. MNPs-PLL were magnetically separated, washed several times with H_2O and used for the binding of the bioactive molecules.

4.3.3 Functionalization with FA or MTX

The bioactive molecules FA and MTX were first activated by an esterification reaction and then conjugated to the free amine groups of PLL bound to the nanosystems.

4.3.3.1 Esterification of FA and MTX

The activation of the -COOH groups of the two molecules was achieved by an esterification reaction with 1-Ethyl-3-(3-dimethylaminopropyl)carbodiimide (EDC) and NHS, in order to obtain the isolable esters NHS-AF and NHS-MTX. The reactions, shown in Figure 4.3-7, were performed in anhydrous DMSO to dissolve the bioactive molecules, using triethylamine (Et_3N) as the catalyst. They were carried out overnight at rt in closed systems to avoid the evaporation Et_3N and protected from light due to the photosensitivity of FA and MTX.

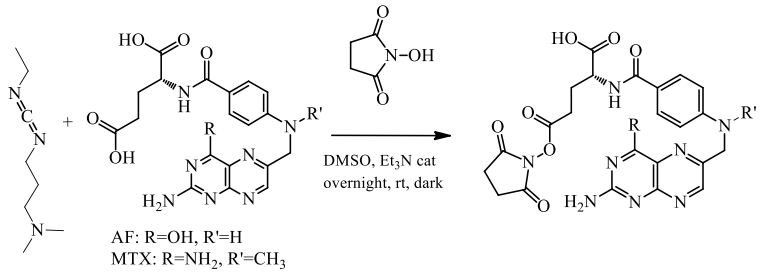

Figure 4.3-7: Scheme of the esterification reaction of FA or MTX using EDC and NHS.

The NHS-esters were purified by precipitation adding ethyl ether to the concentrated DMSO solutions.[139] The yellow-orange precipitates were filtered, washed with ACN to remove the DMSO and dried under vacuum. Unfortunately, this purification method did not remove completely the unreacted FA and MTX which remained in significant amount in the final product (from ^1H NMR analysis NHS-FA:FA ratio 1:1, NHS-MTX:MTX ratio 2:1). However, the conjugation on PLL was performed without further purification.

The first idea was to try binding NHS-FA and NHS-MTX directly on free PLL to allow a better quantification of the loaded drug. This strategy was assessed using NHS-FA, since it was more easily available. The reactions were performed solubilizing the reagents in DMSO and using different concentrations of FA (FA moles at 1.5%, 5%, 10% and 20% of PLL moles, calculated on Lys monomers). The solutions were stirred overnight at rt and protected from light to avoid FA photodegradation. Unfortunately, after drying the reaction mixture, the solubilization with H_2O of all the conjugates PLL-FA led to completely insoluble orange compounds with macroscopic tubular shape, as those shown in in Figure 4.3-8.

Figure 4.3-8: Photo of tubular structures corresponding to PLL-FA conjugate, achieved using 10% of FA.

Further investigation by 1D and 2D ^1H and ^{13}C NMR, like DOSY, TOCSY and NOESY were performed dispersing PLL-FA conjugates in H_2O:D_2O mixture at 90:10 ratio (data not shown). From DOSY experiments DMSO and H_2O molecules resulted involved in the formation of the secondary structure of the PLL-FA conjugate but remaining unstructured since they had logD values < logD of PLL and FA (logD = -8.92 for DMSO, -8.56 for H_2O, -10,1 for PLL and -9.7 for FA). From TOCSY analysis two spin systems for the PABA moiety of FA were found, justifiable by the presence of a fraction of FA covalently bound to PLL and another interacting only by stacking. NOESY experiments did not show dipolar correlations among ^1H of FA and PLL. All these studies suggested a complex secondary structure based on β-sheets, but the structural complexity of the PLL-FA conjugates needed further investigation by solid state techniques.

However, the insolubility of PLL-FA in all the solvent mixtures tried, differing in polarity, pH or ionic strength, drastically limited their use. For this reason, NHS-FA and NHS-MTX were conjugated on PLL already bound to the nanosystems, avoiding the solubilization problems.

4.3.3.2 Conjugation on nanoparticles: MNPs-PLL-FA and MNPs-PLL-MTX

The free amine groups of PLL, anchored on the nanosystems, were used for the reaction with the NHS-esters of FA or MTX. The reactions, reported in Figure 4.3-9, were performed dispersing MNPs-PLL in a solution of NHS-AF or NHS-MTX in DMSO, stirring the mixture overnight at rt and protected from light.

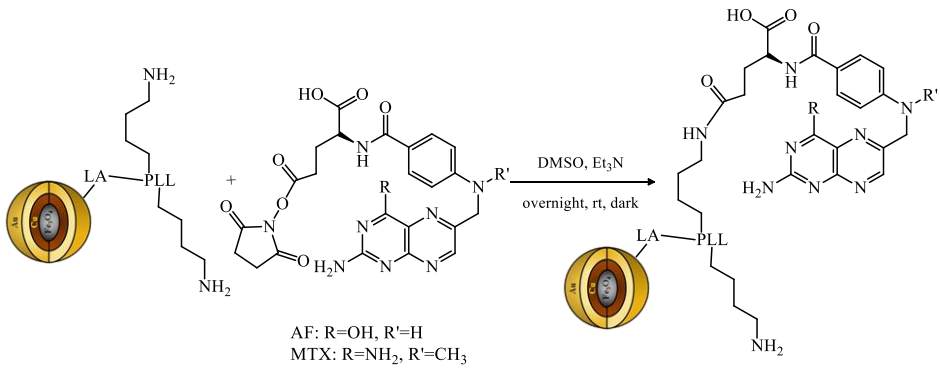

Figure 4.3-9: Reaction scheme of the functionalization of MNPs-PLL with NHS-FA or NHS-MTX.

Since UV-Vis spectroscopy was used for monitoring the reaction and quantify the drug loading, Et_3N was needed to maintain stable the protonation degree of the pteridine moiety of the bioactive molecules during the reaction; in this way it was possible to avoid shifts and profile changes in the absorption bands of FA and MTX in the UV-Vis spectra.[140] The UV-Vis spectra, shown in Figure 4.3-10, demonstrated the conjugation of the bioactive molecules on MNPs-PLL. In fact, the significant decrease in the absorption bands corresponding to FA or MTX in the spectra recorded after the reaction with MNPs-PLL (stop - solid line) compared to the starting solutions of NHS-AF or NHS-MTX (start - dashed line) proved the functionalization of the nanosystems. The loading was therefore estimated in 0.8 mg FA or 0.6 mg of MTX on 50 mg of MNPs, using ε values obtained by calibration curves of NHS-FA and NHS-MTX solutions, dissolved in the same solvent of the reaction.

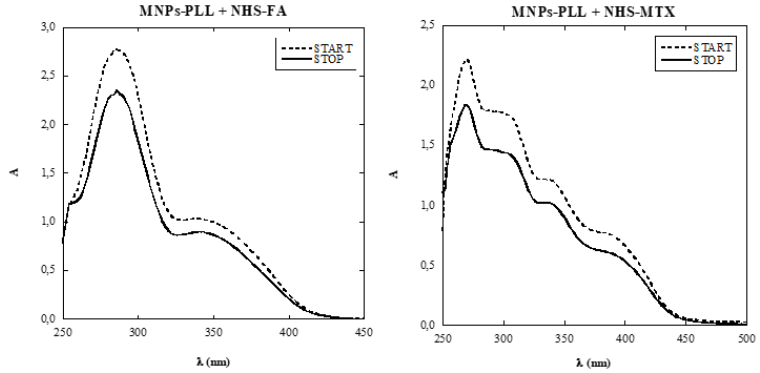

Figure 4.3-10: UV Vis spectra recorded before (start, dashed line) and after (stop, solid line) the reactions between MNPs-PLL and NHS-esters of folic acid (left) or methotrexate (right) which confirmed the binding of the bioactive molecules due to the decrease in their absorption bands.

After magnetic separation and washings, the MNPs-PLL-FA and MNPs-PLL-MTX nanosystems were characterized by several spectroscopic techniques. FT-IR and fluorescence spectra of the MNPs, reported in Figure 4.3-11, confirmed the conjugation of the bioactive molecules; in the FT-IR spectra, in fact, characteristic vibrational bands belonging to FA, MTX and PLL, especially those assigned to amide bonds and pteridine moiety, were detected and the corresponding frequencies were indicated. The strong vibrational band around ν 570 cm^{-1} belonged to Fe-O-Fe bond of the magnetite core.

Furthermore, the fluorescence spectra of MNPs-PLL-AF and MNPs-PLL-MTX, recorded using λ_{exc} at 278 nm, showed the emission bands corresponding to the PABA and pteridine moieties of the bioactive molecules, at λ_{max} at 350 nm and λ_{max} at 440-460 nm, respectively.[141]

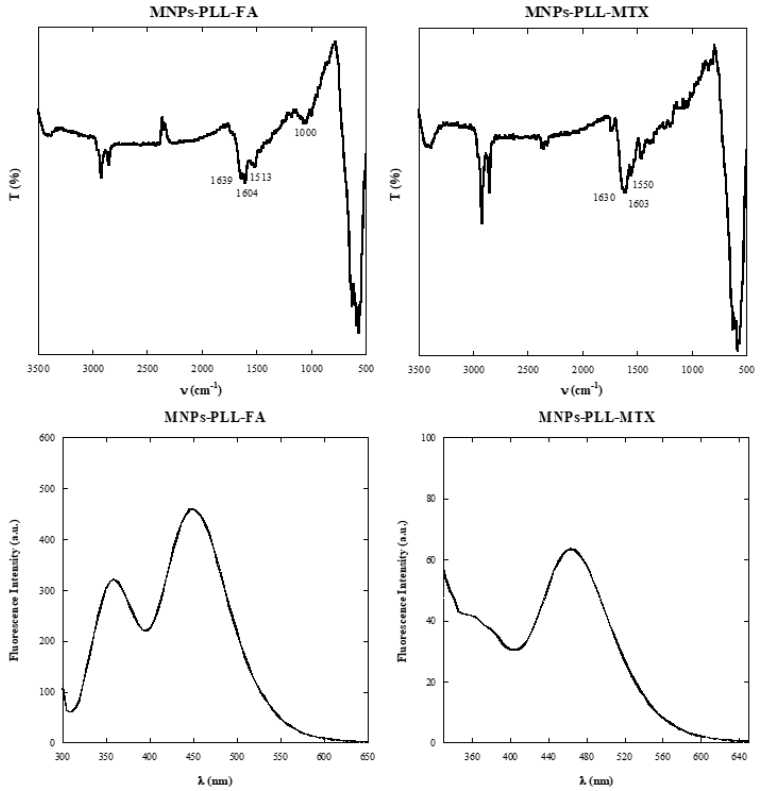

Figure 4.3-11: Top: FT-IR spectra corresponding to MNPs-PLL-FA (left) and MNPs-PLL-MTX (right). The peaks of the vibrational bands belonging to the bioactive molecules were indicated. **Bottom:** fluorescence spectra, recorded using λ_{exc} at 278 nm, of to MNPs-PLL-FA (left) and MNPs-PLL-MTX (right). The emission bands correspond to the PABA and pteridine moieties of FA and MTX.

4.3.4 *In vitro* experiments on human breast cancer cell lines

Once achieved the MNPs-PLL-FA and MNPs-PLL-MTX, *in vitro* biological experiments on cancer cell lines were performed. As introduced previously in section 4.1.3, FA or MTX are considered active targeting ligands for nanosystems due to the overexpression of folate receptors in many cancer cells; in fact, they might help in directing the functionalized nanoplatforms towards cancer cells, accumulating inside them and preserving the healthy ones.

The stabilized human breast cancer cell lines MCF-7 and MDA-MB-231 were selected for the *in vitro* studies on the biological effects of the nanosystems. Both those cell lines correspond to breast adenocarcinoma and literature data confirm their upregulation of α-FR expression.[142] According to previous results, achieved in the same research group in which this thesis was developed, these cell lines were sensitive to MTX, especially MDA-MB-231, as demonstrated by cell viability assay. Moreover, the internalization of those nanosystems was qualitatively confirmed by fluorescence microscopy experiments since the nanosystems loading FA and MTX, labelled with the fluorescent probe Texas Red (TR), were located in intracellular environment compared to the nanosystems functionalized with PLL-TR only.[99] Starting from those experimental data, *in vitro* biological experiments on these cell lines were carried out in order to evaluate the cytotoxic effects of functionalized MNPs by performing cell proliferation assays.

MCF-7 and MDA-MB-231 were incubated with MNPs-PLL-MTX, MNPs-PLL-AF or MNPs-PLL upon different experimental conditions, such as cell amount, incubation time, culture medium and nanoparticles-administration method, and Sulforhodamine B proliferation assays were performed.[143] Cells incubated with free MTX and FA were used as controls, in addition to the negative control consisting of not treated cells. According to the loading quantification of MTX on MNPs, the comparable amount of free MTX, corresponding to 2 μg/mL, was selected for the assays.

The proliferation assays were performed plating 10 000 cells/well or 25 000 cells/well in DMEM and, the next day, incubating them for 24 h or 48 h with the nanosystems. Cells were treated with different amounts of functionalized nanoparticles dispersed in medium, both filtered or not filtered on 0.45 μm filters. A medium without folate, RPMI w/o FA, was selected to remove the presence of basal FA and facilitate the internalization process of MNPs-PLL-FA or MNPs-PLL-MTX due to the vitamin cell need.[133] Since cells might suffered for the absence of FA, the complete RPMI medium was also used. The cell incubation

with MNPs dispersed in PBS was selected as other experimental condition. Serum percentage was also assessed from 0.1% to 10%; low FBS concentration minimized the interactions among nanoparticles and proteins while the high one corresponded to the standard concentration ensuring a good cell viability.

The experiments carried out without filtrating the MNPs presented many problems due to early cell death; in fact, the nanometric and micrometric aggregates had deadly effects on cells, causing their disruption, as shown in Figure 4.3-12. For this reason, the filtration of the MNPs solutions was necessary; however, although this process ensured cell viability, enabling the performance of the proliferation assay, it led to low and unknown drug concentrations in the samples of MNPs, hindering the comparison with free drug.

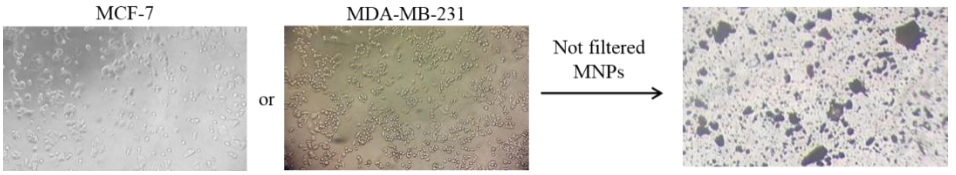

Figure 4.3-12: Images of MCF-7 and MDA-MB-231 before (left) and after (right) the treatment with not-filtered solutions of MNPs.

The best, but not promising, results achieved from these *in vitro* experiments are reported in Figure 4.3-13. These results corresponded to Sulforhodamine B assays performed on MCF-7 and MDA-MB-231 after 24 h of treatment in three experimental conditions. Cells were incubated with different volumes of filtrated solutions of MNPs-PLL or MNPs-PLL-MTX (50 μL or 100 μL) in three media: in PBS, replacing the medium with DMEM complemented with 10% FBS after incubating for 3h, or in RPMI w/o folate + 0.1% FBS or in complete RPMI (w/o the pH indicator phenol red) + 1% FBS. Untreated cells and samples incubated with MTX 2 μg/mL or FA 0.2 μg/mL were used as controls. According to the experimental results, a slight cytotoxic effect of MNPs was detected on both cell lines but without significant differences among cell samples treated with MNPs-PLL and those incubated with MNPs-PLL-MTX. Unfortunately, also free MTX

for 24 h in the same medium was not effective in causing cell death at the concentration of 2 µg/mL since cell viabilities were comparable to those achieved in samples treated with FA 0.2 µg/mL. These data suggested that drug amount in filtered samples was indeed too low to produce cytotoxic effects. These not promising results suggested the need of finding a strategy to reduce the aggregation process of MNPs, to avoid filtration, since it affected the successful performance of the *in vitro* experiments.

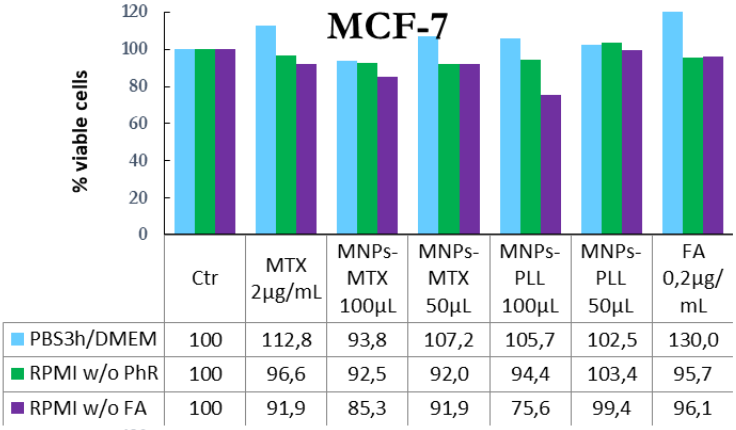

	Ctr	MTX 2µg/mL	MNPs-MTX 100µL	MNPs-MTX 50µL	MNPs-PLL 100µL	MNPs-PLL 50µL	FA 0,2µg/mL
PBS3h/DMEM	100	112,8	93,8	107,2	105,7	102,5	130,0
RPMI w/o PhR	100	96,6	92,5	92,0	94,4	103,4	95,7
RPMI w/o FA	100	91,9	85,3	91,9	75,6	99,4	96,1

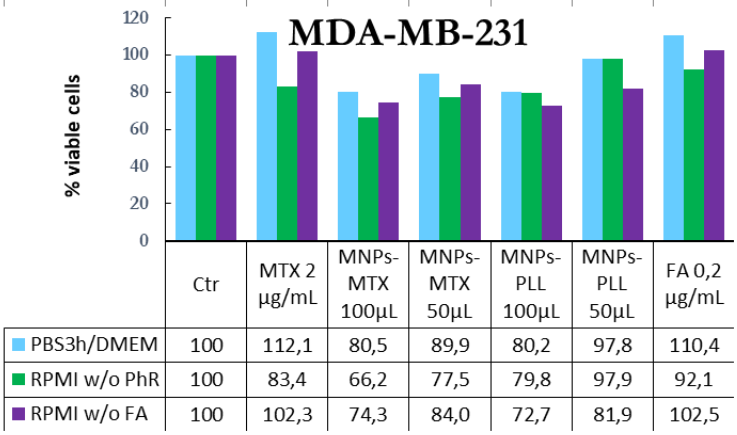

	Ctr	MTX 2 µg/mL	MNPs-MTX 100µL	MNPs-MTX 50µL	MNPs-PLL 100µL	MNPs-PLL 50µL	FA 0,2 µg/mL
PBS3h/DMEM	100	112,1	80,5	89,9	80,2	97,8	110,4
RPMI w/o PhR	100	83,4	66,2	77,5	79,8	97,9	92,1
RPMI w/o FA	100	102,3	74,3	84,0	72,7	81,9	102,5

Figure 4.3-13: Results of the 24 h Sulforhodamine B proliferation assays on MCF-7 (**top**) and MDA-MB-231 (**bottom**). The experimental conditions corresponded to untreated cells (ctr) and cells incubated with free MTX, FA or MNPs-PLL and MNPs-PLL-MTX at two concentrations in volume. The treatments were performed in PBS, replacing after 3 h the medium with DMEM + 10% FBS, or in RPMI w/o folic acid (RPMI w/o FA + 0.1% FBS) or w/o phenol red (RPMI w/o PhR + 1% FBS).

4.3.5 Ball milling process

Several methods were tried in order to minimize the dimensions of the aggregates of MNPs, increasing their dispersibility in solution. The use of surfactants such as cetrimonium bromide or polysaccharides, like xanthan gum, were not helpful. Sonication processes might success in this purpose, but it led to the breaking of S-Au bond, producing coating release in solution, monitored by UV-Vis spectroscopy. Filtration was a good strategy to remove aggregates, but it caused high loss of nanomaterial, and consequently of drug amount, as previously described.

Since the previous strategies were not resolutive, mechanical breaking of MNPs using ball milling technique was tried. This process consists in grinding materials, in this case nanoparticles, by steel balls that moved during the rotation and vibration of the entire mill, as illustrated in Figure 4.3-14.

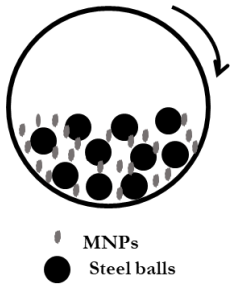

Figure 4.3-14: Scheme of the ball milling process; during the rotations and vibrations of the mill steel balls grind MNPs.

Ball milling was carried out on bare Fe_3O_4 MNPs, setting up the system in inert atmosphere to avoid the oxidation of the magnetite. The effects of this treatment were evaluated by means of AFM analysis. As reported in Figure 4.3-15, the average diameter of Fe_3O_4 MNPs after mechanical grinding was estimated of 12-14 nm. The same analysis was performed after covering the Fe_3O_4 MNPs with Cu and Au shells; AFM images of Fe_3O_4@Cu@Au MNPs and the related statistical analysis suggested the maintenance of the average diameter around 12-14 nm, and

the decrease in the presence of aggregates compared to the same nanosystems not subjected to ball milling (Figure 3.3-10). Moreover, the enhance of the dispersibility of the nanosystems in aqueous solutions was detected.

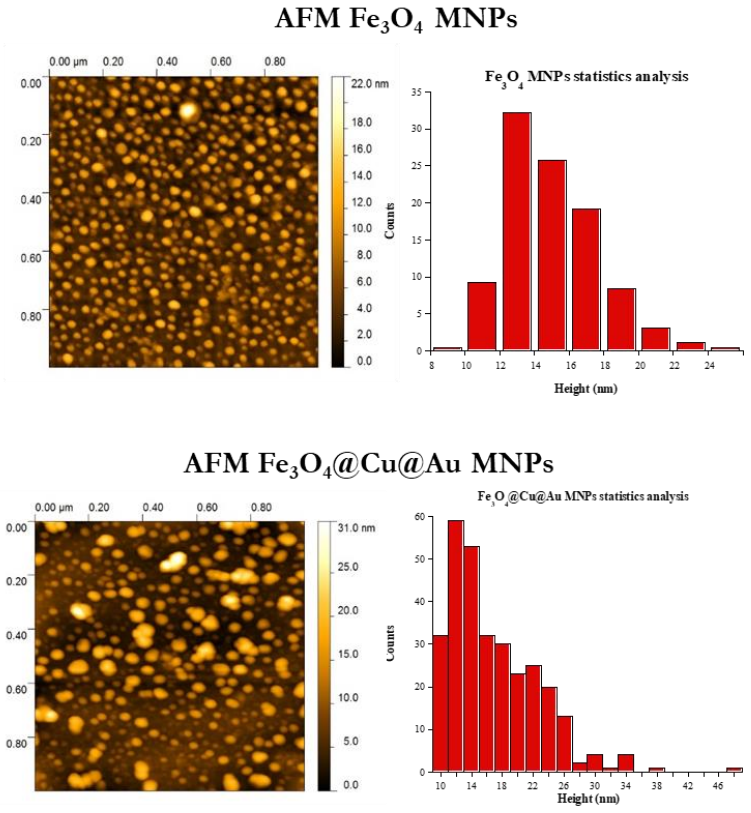

Figure 4.3-15: AFM analysis of Fe_3O_4 MNPs subjected to ball milling before (top) and after the deposition of copper and gold shells (Fe_3O_4@Cu@Au MNPs - bottom). AFM images of the samples are reported on the left while the corresponding statistical analysis on the right.

According to these results, the mechanical grinding by ball milling could be a good option to minimize the amount of aggregates of MNPs in the sample and avoid the filtration of the corresponding solutions. In this way, *in vitro* biological experiments might be performed using functionalized MNPs samples with a known drug concentration and enabling the comparison on cytotoxic effects with the free drug.

4.4 CHAPTER CONTRIBUTIONS

- The Fe_3O_4@Cu@Au MNPs were used for the development of nanosystems carrying the active targeting molecules FA or MTX; to enable the binding of the bioactive molecules, the previous activation of the Au surface with LA and the conjugation of PLL were performed. The drug loading quantification was carried out by means of UV-Vis spectroscopy while the physicochemical characterization of the nanosystems was achieved by FT-IR and fluorescence techniques.
- Since MTX is commonly used as chemotherapeutic drug, the cytotoxic effects of functionalized nanosystems were evaluated on the breast cancer cell lines MCF-7 and MDA-MB-231. Sulforhodamine B proliferation assays suggested a slight cytotoxicity of MNPs, regardless of the presence of the drug. The experimental evidences could be explained as the drug amount was too low to produce toxic effects due to the necessary filtration of the MNPs dispersions. Aggregates, in fact, dramatically affected the success of the experiments, causing early cell death.
- To minimize the presence of big aggregates in the samples, ball milling treatment may be a solution.

4.4.1 Future perspectives

- Functionalize the Fe_3O_4@Cu@Au MNPs, subjected to ball milling process, with the bioactive molecules FA and MTX and try to improve the drug loading, optimizing the reaction conditions.
- Perform the *in vitro* experiments without filtrating the MNPs samples thus knowing the drug concentration and comparing the effects with free drug.

4.5 ACKNOWLEDGMENTS

Dr. Fabio Sciubba and Prof. Maurizio Delfini for NMR studies. Prof. Maria Pia Donzello for FTIR analysis. Prof. Laura Masuelli for the biological experiments. Dr. Maria Assunta Navarra and Dr. Luca Farina for ball milling process. Dr. Francesca Anna Scaramuzzo for AFM analysis. All of them are working at Sapienza University of Rome.

4.6 MATERIALS AND METHODS

Reagents, materials and equipment: All the chemical reagents were purchased by Sigma-Aldrich (Merck KGaA, Darmstadt, Germany) and used without further purification. All the material used in in vitro biological experiments were purchased from Corning (Corning, USA). Permanent magnets made of Neodymium-Iron-Boron alloy, having a magnetic field of 0.3 T, were used for magnetic separations. Sonication was performed with UNISET-AC characterized by 45 W power and 38 KHz maximum frequency. Infrared spectra were recorded from 200 to 4000 cm^{-1} by the spectrometer VARIAN 660-IR FT-IR, preparing the IR tablets mixing 1 mg of sample with 200 mg of anhydrous KBr. Steady-state fluorescence spectra were collected by Varian Cary Eclypse spectrofluorometer, equipped with the Xe lamp using Suprasil® Quartz cuvette. NMR analysis were performed by means of the BRUKER AVANCE 400 MHz spectrometer, using TSP (stock solution in D_2O at 20 mM) as the chemical shift reference. AFM analysis were performed using the microscope MULTIMODE VEECO equipped with the software Nanoscope IIIa; the topographical images of the sample, deposited on Si slice, were collected working in tapping mode using a RTESP Bruker tip (nominal parameters r = 8mm, f = 300 kHz, k = 40 N/m) and recorded with a 512x512 pixel resolution, corrected by polynomial background filters using

the software Gwyddion 2.31. A Vibromulino MM400 (Retsch, Haan, Germany) was used for the ball milling process.

Esterification of Lipoic Acid: NHS-Lipoate: Lipoic acid (4.9 mM) and N-hydroxysuccinimide (NHS 2 eq, 9.8 mM) were dissolved at rt in 50 mL of anhydrous DCM and N,N'-Dicyclohexylcarbodiimide (DCC 2 eq, 9.8 mM) was added after cooling the mixture at 4°C. After stirring 6 h at rt, 1 eq of NHS and 1 eq DCC were added to the solution. After 24 h reacting, the dicyclohexylurea was removed filtered the solution and the work up with a Na_2CO_3 (x3) and NaCl saturated solution (x1) was performed. The organic phase was dried and the crystallization with a mixture of ethyl acetate : hexane - 1:1 was carried out. The final product NHS-Lipoate was achieved as yellow crystals needles-shaped with 61% yield. ^{1}H NMR (300 MHz, $CDCl_3$, 25°C): δ=3.47 (m, 1H, H-3), δ=3.04 (m, 2H, H-1), δ=2.72 (s, 4H, H-8, H-9), δ=2.52 (t, 2H, H-7), δ=2.35 (m, 1H, H-2), δ=1.82 (m, 1H, H-2), δ=1.64 (m, 4H, H-4, H-5), δ=1.44 (m, 2H, H-6).

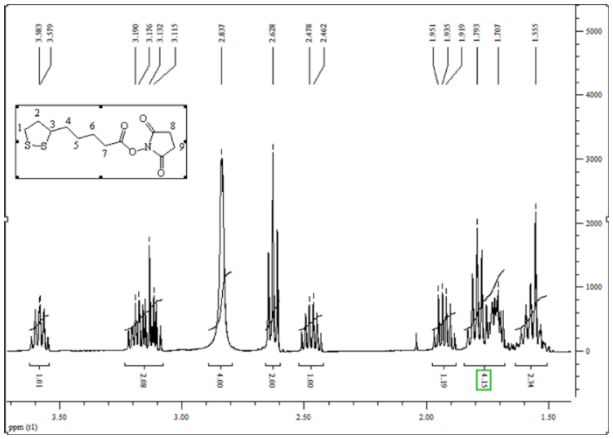

Functionalization with NHS-Lipoate: MNPs-LA-NHS: 100 mg of Fe_3O_4@Cu@Au MNPs were dispersed in 10 mL of NHS-Lipoate in EtAc at 1 mg/mL. After reacting overnight at rt, MNPs-LA-NHS were magnetically collected. UV-Vis spectra of the solutions corresponding to the reaction supernatant, centrifuged 10

min at 10 000 rpm, and to an aliquot of NHS-Lipoate starting solution, maintained in the same reaction conditions, were recorded. MNPs-LA-NHS were washed with EtAc and then dried under vacuum.

Functionalization with poly-L-Lysine: MNPs-PLL: 100 mg of MNPs-LA-NHS were dispersed in 10 mL of a solution of PLL*HBr at 1 mg/mL in HCO_3^- buffer (0.1 M, pH 8.3, filtered on 0.2 μm). After mechanical stirring 2 h 30 min at 4°C, MNPs-PLL were magnetically collected, washed several times with bi-distilled H_2O and dried under vacuum.

Esterification of FA and MTX: NHS-FA and NHS-MTX

EDC (3 eq, 0.6 mmol) and NHS (3 eq, 0.6 mmol) were added to a solution of MTX or FA (0.2 mmol) dissolved in 5 mL of anhydrous DMSO containing 4% Et_3N. The reaction was stirred overnight at rt protected from light. After concentrating the solution under vacuum heating at 40°C, ethyl ether was added dropwise to the solution under stirring, in order to precipitate the NHS-ester. The solution was then filtered under vacuum washing the precipitate with CH_3CN (ACN) and finally drying under vacuum, achieving orange-yellow products. ^1H NMR (400 MHz, d^6 DMSO, 25°C) spectra of NHS-FA and NHS-MTX were compared to those of FA and MTX monitoring the shifts of the reference doublets corresponding to ^1H of PABA moieties, at δ 7.73 ppm (2H) and δ 6.73 ppm (2H) for FA and at δ 7.62 ppm (2H) and δ 6.76 ppm (2H) for MTX.

Functionalization with NHS-FA or NHS-MTX: MNPs-PLL-FA and MNPs-PLL-MTX: 5 mL of a solution of NHS-MTX or NHS-FA at 1 mg/mL in anhydrous DMSO containing 4% Et_3N were added to 5 mL containing 50 mg of MNPs-PLL in the same solvent. The reaction was carried out at rt overnight in systems closed and protected from light. The next day, MNPs-PLL-FA or MNPs-PLL-MTX were magnetically collected and UV-Vis spectra of the solutions corresponding to the reaction supernatants, centrifuged 10 min at 10000 rpm, and to the aliquot of the NHS-MTX or NHS-FA starting solution, maintained in the reaction conditions,

were recorded. The drug loading was calculated as the average Δc corresponding to A values at λ 269 nm, 300 nm and 386 nm for MTX and λ 288 nm and 326 nm for FA. The ε at the same λ were obtained using calibration curves of NHS-MTX and NHS-FA dissolved in the DMSO + 4% Et_3N. For NHS-FA ε_{288}=4.04 mg^{-1} mL cm^{-1} and ε_{360}=1.83 mg^{-1} mL cm^{-1} while for NHS-MTX ε_{269}=4.28 mg^{-1} mL cm^{-1}, ε_{300}=3.48 mg^{-1} mL cm^{-1} and ε_{386}=1.35 mg^{-1} mL cm^{-1} were used. The estimated loading was 0.6 mg MTX on 50 mg MNPs-PLL-MTX and 0.8 mg of FA on 50 mg MNPs-PLL-FA. MNPs-PLL-MTX and MNPs-PLL-FA were washed several times with bi-distilled H_2O and dried under vacuum.

In vitro experiments on MCF-7 and MDA-MB-231 - Sulforhodamine B proliferation assays: 25 000 cells/well in DMEM supplemented with 10% FBS and 1% pen strep were plated in 96-wells plate for 24 h. MNPs-PLL and MNPs-PLL-MTX were dispersed at 2 mg/mL in sterile PBS buffer, in RPMI 1640 w/o folate + 0.1 % FBS or in RPMI 1640 w/o Phenol Red + 1% FBS. The MNPs dispersions were filtered on 0.45 μm filters and 200 μL of the 1:2 or 1:4 dilutions in the corresponding medium were added to the plate. FA at 0.2 μg/mL and MTX at 2 μg/mL solutions in the same RPMI media or in DMEM + 10% FBS were used as controls, in addition to untreated cells in the four media. Cells were incubated at 37°C and 5% CO_2; only in the sample treated with MNPs in PBS the buffer was replaced by DMEM + 10% FBS after 3 h incubating. After 24 h of treatment, Sulforhodamine B proliferation assay was performed as described in the standard protocol[143] and the A values at λ=492 nm and 620 nm were measured. The corresponding ΔA is related to cell viability, considering 100% the ctr sample.

Ball Milling Process: Fe_3O_4 MNPs were subjected to ball milling treatment, assembling the system in a glove box in inert atmosphere. 1,44 g of Fe_3O_4 MNPs and 3 steel balls, with a total weigh of 12.5g were mixed. 8 grinding cycles, lasting 1 h each, were performed working at ν 25 Hz.

5. Fe_3O_4@Cu@Au NANOPARTICLES COATED WITH MACROMOLECULES FOR THE ENGULFMENT OF HUMAN IMMUNE CELLS

5.1 INTRODUCTION

Cell-based delivery of nanosystems using immune cells is becoming a very interesting strategy to transport and release engineered NPs inside the body.[48] The design of nanosystems which can be efficiently internalized leading to a good percentage of engulfed cells is already a challenge in this field. The development of nanosystems coated with different macromolecules for the engulfment of macrophages is the topic of this research work.

5.1.1 Transferrin

Transferrin (Tf) has gained great interest for biomedical applications involving nanosystems thanks to its physiological importance in transporting and regulating the iron concentration in biological environment and its specific intracellular uptake. The glycoprotein Tf, which structure is shown in Figure 5.1-1 from ref [144], is characterized by a Mw of ≈80 KDa and it is divided in two lobes linked by a short spacer. Each lobe presents two domains interacting together to form the deep hydrophilic iron binding site; there, four amino acids (Asp 63, Tyr 95, Tyr 188 and His 249), arranged in a distorted octahedral geometry, coordinate Fe^{3+} with an affinity constant of K_{ass} 10^{20} M^{-1} at physiological pH. During this process the synergistic collaboration of two O atoms of a carbonate anion occurs.

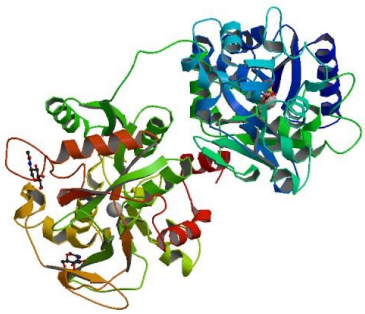

Figure 5.1-1: Structure of the Diferric bound human serum transferrin (from PDB 3QYT).

The efficient uptake mechanism of iron-loaded Tf by endocytosis is mediated by the specific transferrin membrane receptors (TfR).[145] The transferrin binding protein TfR1 is expressed in almost all cells of the body, especially in blood cells

such as macrophages, and it is often upregulated in rapidly proliferating cells, including in cancer cells.[146] For this reason, Tf-drug conjugates or nanosystems functionalized with Tf can more easily reach and enter into their biological targets thanks to the active targeting ability of Tf.[147] Several examples of nanosystems including transferrin can be found in the literature. For instance, polymeric or lipid nanosystems loading drugs, DNA or radioisotopes, complexed or conjugated to Tf, can be actively directed to the pathological area for therapeutic applications while metal nanoparticles loading Tf can be used for targeting and imaging brain tumours, such as glioma.[117,148,149]

5.1.2 Streptavidin

Streptavidin (Stv) is a protein commonly used in biological and biotechnological applications due to its high affinity for biotinylated molecules. In fact, together with Avidin, Stv is classified as a biotin-binding protein.[150] Produced by the bacterium *Streptomices avidinii*, Stv is a homo-tetramer able to bind with high affinity four molecules of biotin, also known as vitamin H, per mole of protein. This binding occurs by the strongest non-covalent interaction known in nature, leading to the formation of Stv-biotin complex characterized by K_d value of $\approx 10^{-15}$ M. As shown in Figure 5.1-2 from ref [151], the secondary structure of Stv is characterized by high amount of β-sheets, involved in the formation of the biotin binding site.

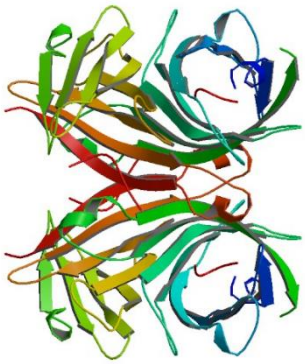

Figure 5.1-2: Structure of Streptavidin complexed with the peptide FSHPQNT (from PDB 1VWA).

Due to this extraordinary affinity, Stv has been therefore exploited in many biotechnological and nanobiotechnological applications based on the binding of biotinylated molecules and macromolecules;[152,153] Stv-biotin complexes are commonly used in several bioanalytical techniques, especially immunoassays and

biosensors.[154-156] Moreover, the derivatization of drugs or proteins, especially enzymes or antibody, with biotin can ensure the strong binding to Stv-coated nanosystems which can be employed for diagnostic or therapeutic purposes.[157-159]

5.1.3 Cell-mediated delivery: Trojan Horse Approach

Cell-mediated delivery of nanoparticles is a new and promising option in addition to the standard passive and active targeting strategies, already described in section 4.1.1. It is based on the exploitation of immune cells, especially neutrophils, monocytes and macrophages, for the transport and delivery of engineered nanoplatforms inside the body.[160,161] In this way, the overcoming of several limits of the other drug delivery strategies especially reaching deep affected tissues, can be achieved. In fact, in addition to their high innate biocompatibility and stealth features, immune cells are naturally able to reach all the tissues in the organism, also crossing hardly permeable barriers, such as the brain-blood barrier.[162] They are involved in many fundamental physiological processes: in fact, the organism surveillance and defence against external pathogens, such as bacteria and viruses, and the elimination of cellular debris and dead cells depend on them. Since many of these cells are also directly involved in accelerating or contrasting several pathological processes, especially cancer, infections and inflammations, their use as carriers of medicated nanosystems can be a good strategy to achieve a more efficient *in loco* drug delivery.[163-165]

Generally, the loading of nanosystems on cells can be achieved by covalent modification or non-covalent interactions among cell membrane and NPs or by exploiting the phagocytic activity of some kinds of immune cells that leads to the internalization of the nanosystems.[166] The internalization of engineered nanoparticles in *ex vivo* cells, especially monocytes and neutrophils, extracted from the patient and incubated with the medicated nanoparticles, produce MNPs-loaded cells. These cells can act as Trojan Horses once reintroduced in the patient,

migrating to the pathological focus thanks to innate chemoattraction, reaching for instance the hypoxic areas of tumours.[167] Once there, they can release their cargo by physiological or external inputs.[168] This promising strategy reported in Figure 5.1-3, is known as Trojan Horse approach and it can help improving the effectiveness of therapeutic treatments based on nanotechnological approaches.[167] Macrophages, albeit adherent cells, can also be selected as Trojan horses thanks to their high phagocytic activity.

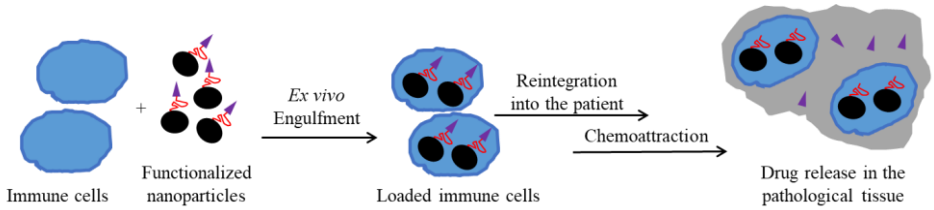

Figure 5.1-3: General scheme of the Trojan Horse approach based on the *ex vivo* incubation of immune cells with engineered nanoparticles and their migration into pathological area by natural chemoattraction mechanism once reintroduced in the patient.

Notwithstanding the great advantages, this technique presents some limits; for instance, the need of loading high number of cells in order to achieve a huge population of cells migrating to the pathological focus. Moreover, the drug must remain active inside the immune cell, without undergoing degradation, and be released once reached the target.[160]

5.1.3.1 Macrophages

Macrophages, together with neutrophils and monocytes, may be suitable for internalizing engineered nanosystems as they possess innate phagocytic capability that they use for their physiological actions.[169] Macrophages are located in almost all tissues and they derive from monocytes. Monocytes, instead, are circulating cells which can differentiate into macrophages once crossed the endothelial barrier and penetrated deeply in the organs. Two phenotypes of macrophages can be distinguished depending on their metabolism: the activated pro-inflammatory (M1) and the activated anti-inflammatory (M2) macrophages. These cells are involved in several diseases, especially cancer and inflammation disorders, playing different roles depending on their polarization; in fact, M1 can exhibit tumoricidal activities while M2 tumorigenic ones.

Due to their physiological and/or pathogenic roles and their phagocytic ability, macrophages have been selected for imaging and therapeutic applications using nanoparticles.[170,171] Several engineered nanoparticles have been incorporated into macrophages via phagocytosis, thus exploiting these engulfed cells as Trojan Horses. For instance, Au nanoshells, NPs or liposomes loading doxorubicin were successfully internalized in macrophages or monocyte-differentiated macrophages for *in vitro* or *in vivo* applications for cancer treatments.[172,173] Moreover, in this context the accumulation of macrophages carrying functionalized MNPs into deep tumour sites by applying pulsed magnetic field has been demonstrated, since the cells acquired magnetic field responsiveness.[174]

5.2 CHAPTER OBJECTIVES

Since macrophages are involved in the organism defence and are infiltrated in affected organs, they can be exploited as Trojan Horses for cell-mediated delivery of engineered nanosystems. Their phagocytic ability can be useful for facilitating the internalization of the nanosystems which can be transported and released also in hardly accessible areas of the body through natural chemoattraction mechanisms.

A study of the internalization of differently coated nanosystems could help to understand the coating features needed for the achievement of high percentage of NPs-loaded cells, since this is the main limit to the real applicability of this strategy. For this reason, the evaluation of the intracellular uptake of Fe_3O_4@Cu@Au MNPs functionalized with three macromolecules is the aim of this work. In this study, transferrin, streptavidin and poly-L-lysine are selected for coating the activated MNPs-LA-NHS thanks to their biological and/or chemical properties. The protein labelling with the red fluorescent probe Texas Red and the physicochemical characterization of the conjugates are the first objectives of this research. As shown in Figure 5.2-1, after the synthesis of the engineered nanosystems, *in vitro* experiments incubating them with macrophages, achieved by a differentiation process of human leukemic monocytic cells (THP-1 cell line), can allow to select the most promising nanosystem for biomedical applications based on Trojan Horse method.

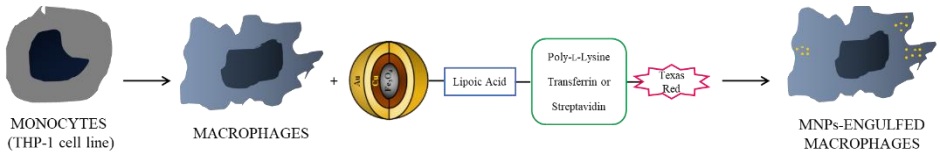

Figure 5.2-1: Scheme of the aim of this research work concerning the internalization of differently coated nanoparticles in macrophages, achieved by differentiation of monocytic THP-1 cell line.

5.3 RESULTS AND DISCUSSION

The internalization studies on human immune cells of Fe_3O_4@Cu@Au nanosystems functionalized with PLL, Tf or Stv are presented and discussed in this section. The synthesis and characterization of the engineered nanoparticles have been firstly addressed.

5.3.1 Functionalization of MNPs-LA-NHS with macromolecules

Three different macromolecules were selected for the coating of MNPs-LA-NHS; the two proteins Tf and Stv were chosen due to the active targeting ability and the possibility of further binding of biotinylated molecules, respectively. PLL, instead, was selected as synthetic polymer model according to its chemical features and biocompatibility. In order to reveal the nanosystems during biological experiments, the macromolecules needed to be labelled. The red fluorescent dye Texas Red (TR) was selected for the labelling of PLL and Tf, while Stv was bought already conjugated to the same probe.

5.3.1.1 Labelling of PLL and Tf with TR

The labelling of PLL and Tf with TR was needed for monitoring the nanosystems during the *in vitro* experiments with macrophages, thus the functionalized MNPs displayed red fluorescent and could be detected by fluorescence microscopy. TR is the Sulforhodamine 101 chloride, a more reactive derivative of the rhodamine due to the presence of the $-SO_2Cl$ group. The nucleophilic $-NH_2$ groups of Lys residues of the macromolecules, in fact, could easily react with the $-SO_2Cl$ functionality of the dye, as shown in Figure 5.3-1, leading to covalent sulfonamide

bonds. The reactions were performed mechanically stirring the solutions for 1 h in HCO_3^-/CO_3^{2-} buffer at pH 9 in order to improve the deprotonation of $-NH_2$ groups. The T was maintained at 0°C to slow down the spontaneous hydrolysis of the $-SO_2Cl$ group to sulfonate while the reaction system was protected from light to avoid the dye photobleaching.

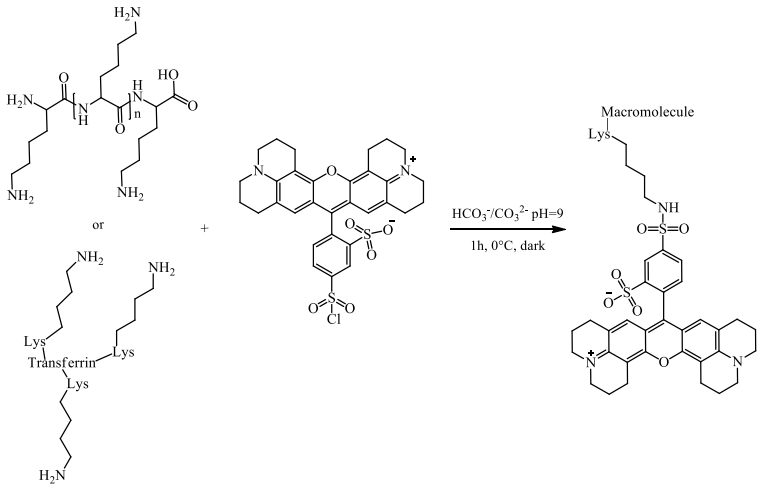

Figure 5.3-1: Scheme of the labelling of poly-L-lysine and Transferrin with the dye Texas Red**.**

The PLL-TR and Tf-TR conjugates were purified by gel permeation chromatography, as shown on the left in Figure 5.3-2, eluting the solutions on the Sephadex® stationary phase with H_2O and selecting by UV-Vis spectroscopy the fractions containing the conjugate. Once purified, the conjugates PLL-TR and Tf-TR were lyophilized obtaining spongy pink-purple compounds which were characterized by fluorescence spectroscopy. As shown on the right in Figure 5.3-2, in the fluorescence spectra, recorded using λ_{exc} at 588 nm, the emission bands at λ= 604 nm and λ= 611 nm for PLL-TR and Tf-TR conjugates, respectively, belonged to the fluorescent probe. The blue-shift of the bands comparing to free TR (λ=615 nm) was probably related to the change in the local environment of the dye due to the presence of the macromolecules and it confirmed the success of the conjugation process.[175]

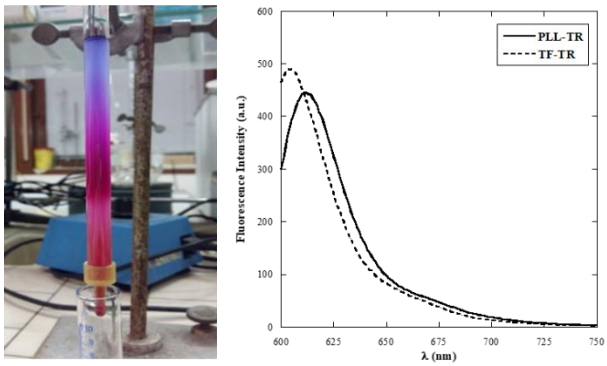

Figure 5.3-2: Left**:** PLL-TR purification by gel permeation chromatography. Right: Fluorescence spectra, recorded using λ_{exc} at 588 nm, corresponding to PLL-TR (solid line) and Tf-TR (dashed line) aqueous solution. The emission bands belong to the TR bound to the macromolecules.

5.3.1.2 Anchorage on MNPs-LA-NHS

The labelled macromolecules PLL-TR, Tf-TR and Stv-TR were conjugated on MNPs-LA-NHS. As shown in Figure 5.3-3, the formation of the covalent amide bonds was achieved by the reaction among the free deprotonated -NH_2 groups of the Lys residues of the macromolecules and the NHS moiety of the lipoate anchored on the nanosystems.

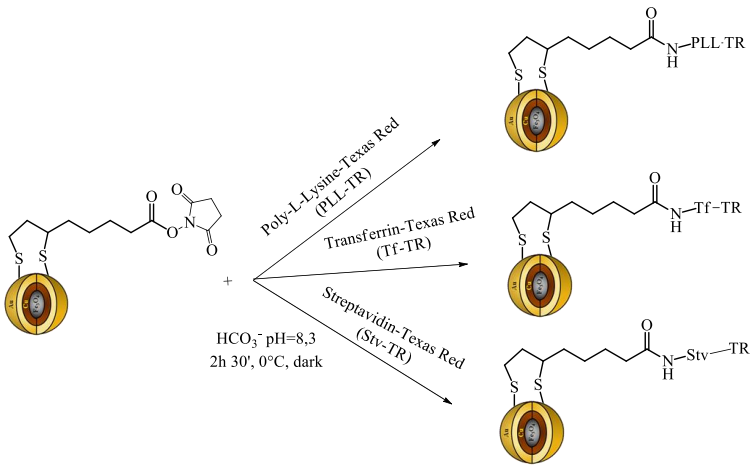

Figure 5.3-3: Reaction scheme of the functionalization of MNPs-LA-NHS with the labelled macromolecule PLL-TR, Tf-TR or Stv-TR.

The monitoring of the functionalization reaction of MNPs-LA-NHS was performed recording UV-Vis spectra of the reaction solutions before and after the reactions with the nanosystems, magnetically separated from the mixture. As shown in Figure 5.3-4 only for the reaction between MNPs-LA-NHS and PLL-TR on representative purposes, the functionalization was confirmed; in fact, comparing the absorption spectra before (start - dashed line) and after (stop - solid line) the reaction with MNPs-LA-NHS, the decrease of the absorption band at λ≈590 nm, belonging to TR bound to the macromolecule, and the contemporary increase of that at λ=280 nm, corresponding to the free NHS released during the reaction, proved the conjugation.

MNPs-PLL-TR, MNPs-Tf-TR and MNPs-Stv-TR were magnetically collected, washed and characterized by fluorescence spectroscopy after drying under vacuum. Emission bands, centred around λ=600-612 nm, were achieved for all the nanosystems (data not shown).

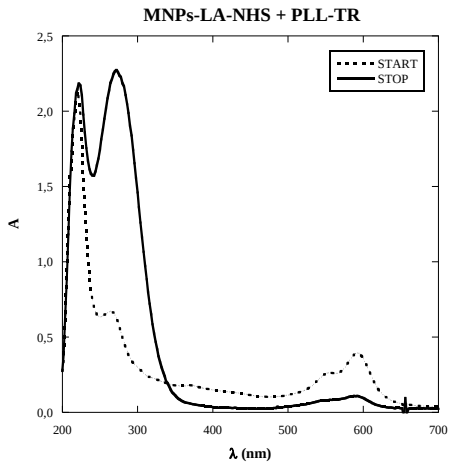

Figure 5.3-4: UV-Vis spectra collected before (start - dashed line) and after (stop - solid line) the reaction between MNPs-LA-NHS and PLL-TR. The decrease in the absorption band at λ≈590 nm and the increase in that at λ=280 nm, belonging to TR and NHS respectively, confirmed the functionalization.

5.3.2 *In vitro* biological experiments on human immune cells

In vitro biological experiments on monocyte-differentiated macrophages were performed in order to study the internalization of the differently functionalized nanosystems; the principal aim of this work was to identify the coating leading to the highest number of MNPs-loading cells. The achievement of a high percentage of MNPs-engulfed cells, in fact, is the main challenging topic in Trojan Horse approach since it limits the real applicability.

5.3.2.1 THP-1 cell line: monocyte-differentiated macrophages

Macrophages were achieved by differentiation from THP-1 cell line, derived from a human monocytic leukaemia.[176] This cell line was selected since it can be considered a model of native monocyte/macrophages system and it is commonly used for NPs-uptake studies.[177]

The differentiation was induced incubating for 48 h the monocytic cells with Phorbol 12-myristate 13-acetate (PMA) at nanomolar concentration in culture medium. As shown in Figure 5.3-5, the significant changes from the round-shaped monocytes to the ramified and adherent macrophages confirmed the successful of the differentiation. After 24 h resting, macrophages were ready to be used in MNPs uptake studies.

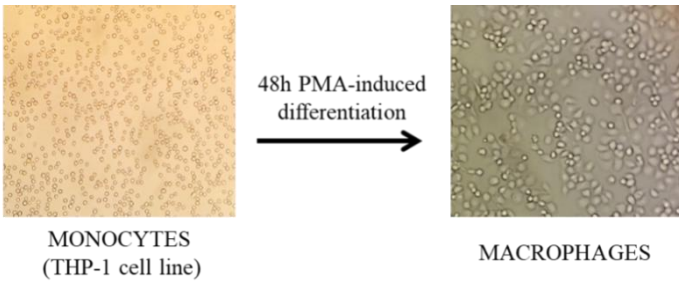

Figure 5.3-5: Images of the PMA-induced differentiation of THP-1 monocytes to macrophages. Adherent ramified cells (right) were achieved from suspension round-shaped cells (left).

5.3.2.2 MNPs-internalization experiments

Macrophages were incubated with MNPs-PLL-TR, MNPs-Tf-TR or MNPs-Stv-TR assessing several parameters such as incubation time, culture medium and mood of administration of nanosystems. The incubation times were varied from 15 min to 6 h, to obtain uptake information on short and long time. Good results were achieved incubating cells for 2 h, since shorter times led to low uptake while longer time to the worsening of cell conditions. One or several administrations of MNPs-macromolecules were performed; the repeated administrations slightly enhanced the MNPs internalization but causing higher cell stress, revealed by cell detachment. Incubation medium was also assessed; MNPs-macromolecules were dispersed in PBS buffer or in RPMI w/o PhR, complemented with 1% FBS only for long incubation times. The culture medium was finally preferred to maintain a good cell viability. Nanoparticles were administered to the cells as unfiltered or filtered dispersions, achieving better results in the second case; the filtration on 3 μm filters allowed to maintain a high concentration of nanosystems removing the bigger aggregates which affected cell viability.

The best results confirming the internalization of the MNPs-macromolecules were achieved incubating monocyte-differentiated macrophages for 2 h at 37°C in 5% CO_2, administering the filtered dispersion of nanosystems only once. Untreated cells, incubated in the same conditions as the treated ones, were used as negative controls. Different methods or techniques were employed for the characterization of MNPs-engulfed macrophages.

A simple, quick and reliable evidence of the MNPs internalization was achieved by Prussian Blue Staining. In this way it was possible to highlight the presence of iron deposits inside cells. In fact, as shown in Figure 5.3-6 for macrophages incubated with MNPs-Tf-TR, intracellular blue spots, absent in the control sample, demonstrated the presence of the nanosystems inside the cells, which were identified by nuclear staining with neutral red. The ferric ions of Fe_3O_4 core,

reacted with potassium ferrocyanide forming a deeply blue coloured complex ferric ferrocyanide known as Prussian Blue. This staining could work regardless of MNPs coating, since the positivity derived from the magnetic core of the nanosystems.

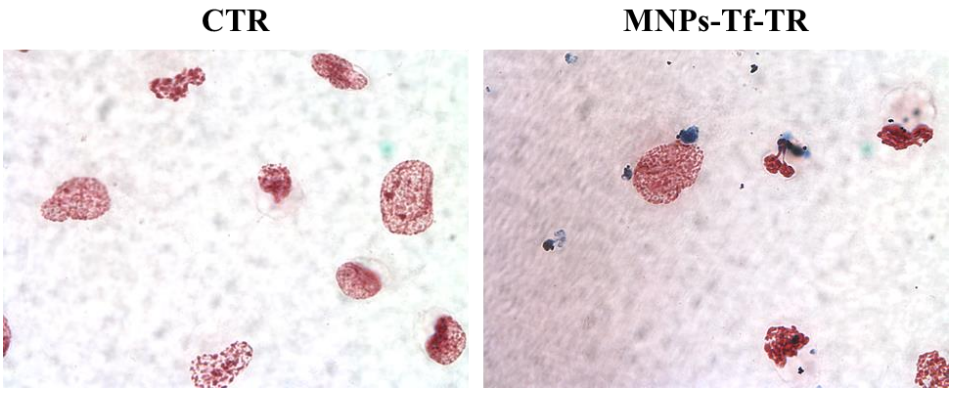

Figure 5.3-6: Prussian Blue staining of monocyte-derived cells untreated (ctr on left) or incubated with MNPs-Tf-TR (on right). Intracellular blue spots, corresponding to ferric ferrocyanide complex, proved the presence of iron deposits produced by internalized nanoparticles.

A qualitative evidence, not reported, was achieved by applying an external permanent magnet under the cell plates after incubating macrophages with MNPs-macromolecules and removing the not internalized nanoparticles by several washings. During this experiment, some cells moved following the magnetic field and accumulating around the magnet. This phenomenon could be explained by the presence of magnetic materials inside the macrophages, corresponding to internalized MNPs, which acquired magnetic field responsiveness.[49]

By confocal fluorescent microscopy the evidence of MNPs-macromolecules uptake was achieved. Fluorescence images of fixed samples of untreated cells or cells incubated with the differently coated nanosystems are shown in Figure 5.3-7. Z-stack acquisitions were performed on each sample, virtually sectioning the entire cell volume in planes and collecting fluorescent images from each plane. Here, the images corresponding to a central plane (23-27/40 planes) were reported.

The red fluorescence spots in intracellular compartments of macrophages, corresponding to cell samples incubated with MNPs-macromolecules, derived from TR conjugated to the nanosystems. Blue fluorescence, instead, derived from cell nuclei stained with Hoechst. According to these experimental evidences, the uptake of MNPs-Tf-TR, MNPs-PLL-TR and MNPs-Stv-TR was achieved, and the internalization occurred for all nanosystems regardless from coating. However, the percentage of MNPs-engulfed cells was not high, since many cells did not show any intracellular red-fluorescent spots.

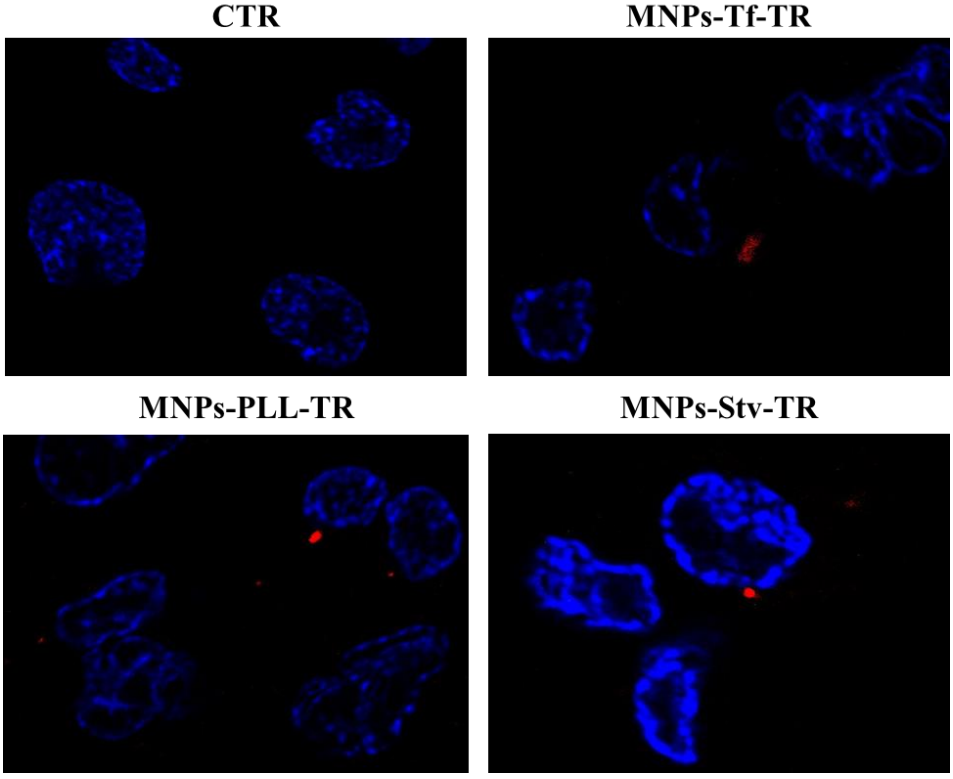

Figure 5.3-7: Fluorescence images of monocyte-differentiated macrophages incubated 2h without (ctr – top left) MNPs or with filtered dispersions of MNPs-Tf-TR (top right), MNPs-PLL-TR (bottom left) or MNPs-Stv-TR (bottom right). Cell nuclei were stained with Hoechst while the internalized nanoparticles were identified by red spots due to the Texas Red labelling. Images were collected by means of a confocal fluorescence microscope with a 100 X immersion objective. The images correspond to central planes (23-27/40 planes) of the z-stack acquisitions.

Quantitative information about the internalization process were achieved by flow cytometry analysis. After 2 h incubation, monocyte-differentiated macrophages were detached and fixed with paraformaldehyde solution at 4%, without performing the nuclear staining. The samples were analyzed monitoring the red-fluorescence emission and the quantification of the MNPs-engulfed cells was performed comparing the data with the control cell sample. As shown in Figure 5.3-8, the % of macrophages producing red fluorescent signals, due to internalized nanosystems, was estimated of 12%, 9% and 33% for MNPs-PLL-TR, MNPs-Stv-TR and MNPs-Tf-TR, respectively. These data suggested a preferential uptake of MNPs-Tf-TR, although the degree of internalization for all samples was not very high. The preference of Tf-coated nanoparticles might be explained as the transferrin receptors are usually widely present on macrophage membranes, thus facilitating the internalization of that kind of nanosystems by receptor-mediated endocytosis.[178] The low general uptake could instead derive from experimental conditions that might be optimized.

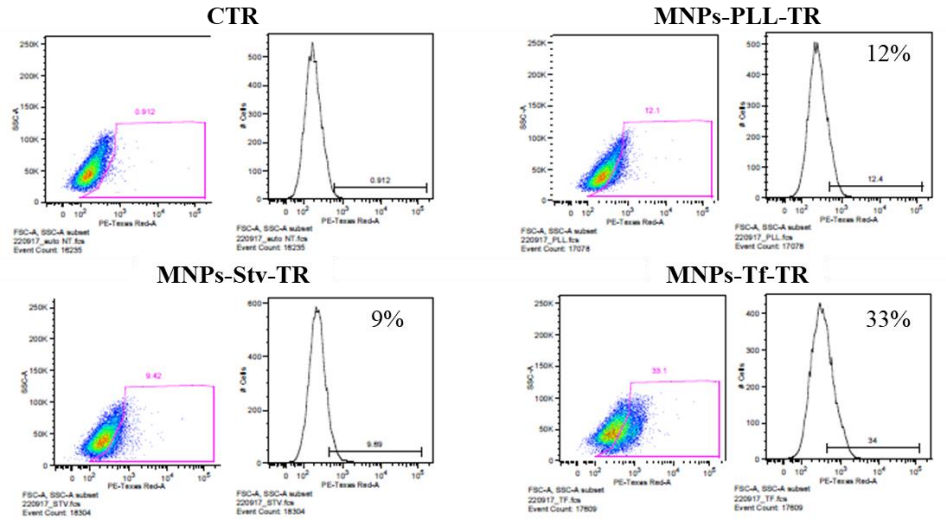

Figure 5.3-8: Flow cytometry analysis of monocyte-differentiated macrophages incubated 2h with MNPs-PLL-TR (top right), MNPs-Stv-TR (bottom left) or MNPs-Tf-TR (bottom right). The percentage of red-fluorescent cells, due to MNPs uptake, was quantified compared to untreated cell sample (CTR – top left).

5.4 CHAPTER CONTRIBUTIONS

- A study on the preferential uptake of differently coated nanosystems by phagocytic cells was performed by *in vitro* experiments incubating monocyte-differentiated macrophages, achieved THP-1 cell line, with Fe_3O_4@Cu@Au MNPs functionalized with the macromolecules PLL, Tf and Stv. By labelling the macromolecules with TR, the internalization of the nanosystems was confirmed by fluorescence microscopy, in addition to the Prussian Blue Staining used for revealing iron intracellular deposits. The MNPs-uptake was successfully achieved, preferentially for MNPs-Tf-TR, leading to 33% of engulfed cells as measured by flow cytometry.
- MNPs-Tf-TR might be promising nanosystems for cell-mediated drug delivery purposes based on Trojan Horse method.

5.4.1 Future perspectives

- Optimize the experimental conditions in order to enhance the loading and assess the stability, cytotoxicity and degradation of the internalized nanosystems.
- Try to internalize the nanosystems into other cell lines, including native phagocytic cells and evaluate the response of MNPs-engulfed cells to external magnetic fields in order to exploit magnets for their collection and focusing.
- Functionalize the MNPs-Tf nanosystems with drugs or explore other molecules or macromolecules more specific for activated macrophages and evaluate the real applicability of monocytes-derived macrophages as Trojan Horses for the delivery of bioactive compounds to malignant cells *in vitro* and *in vivo*.

5.5 ACKNOWLEDGMENTS

Prof. Laura Masuelli of Sapienza University of Rome for Prussian blue staining. Dr. Valeria de Turris, Dr. Giovanna Peruzzi and Prof. Giancarlo Ruocco of Centre for Life Nanoscience@Sapienza– Istituto Italiano di Tecnologia - for confocal fluorescence microscopy and flow cytometry analysis.

5.6 MATERIALS AND METHODS

Reagents, materials and equipment: All the chemical reagents were purchased by Sigma-Aldrich (Merck KGaA, Darmstadt, Germany) and used without further purification. All the material used in in vitro biological experiments were purchased from Corning (Corning, USA). Sephadex G-25 fine was used as stationary phase in gel permeation chromatography. Permanent magnets made of Neodymium-Iron-Boron alloy, having a magnetic field of 0.3 T, were used for magnetic separations. Sonication was performed with UNISET-AC characterized by 45 W power and 38 KHz maximum frequency. Fluorescence spectra were collected by Varian Cary Eclypse spectrofluorometer, equipped with the Xe lamp. Prussian Blue staining images were collected by Olympus BX53 equipped with an 100x oil immersion objectives lens. The fluorescence confocal microscopy and the flow cytometer were at the Centre for Life Nanoscience IIT@Sapienza. The fluorescence images were collected z-stack mode acquiring 40 planes, 0.2 μm distant one from each other, by means of the inverted microscope Olympus X73 equipped with 100x oil immersion objectives lens. The flow cytometer BD LSRFortessa® with a green laser at 532 nm (600 LP) was used for the quantification of the MNPs-loaded macrophages, counting ≈17000 events for each sample.

Labelling of poly-L-Lysine and Transferrin: PLL-TR and TF-TR: 20 mg of PLL or Human Apo-Transferrin dissolved at the concentration of 0.1 mg/mL in carbonate buffer (0.1 M, pH 9) were mixed with 1 mg of TR dissolved in 50 μL of ACN. After 1 h stirring the reactions in dark at 0°C, the purification was performed by gel permeation chromatography on Sephadex® G 25-fine stationary phase eluting the solutions with bi-distilled H_2O. Fractions containing PLL-TR or TF-TR, selected by UV-Vis spectra, were collected and lyophilized. Pink-purple products were achieved with 67 and 72% yield.

Conjugation of the macromolecules on MNPs-LA-NHS:MNPs-PLL-TR, MNPs-Tf-TR and MNPs-Stv-TR: 100 mg of MNPs-LA-NHS were dispersed in 10 mL of PLL-TR, TF-TR or STV-TR solutions at 0.5 mg/mL in bicarbonate buffer (0.1 M, pH 8.3). After 2h 30 min mechanically stirring the solutions at 4°C protecting from light, MNPs were magnetically separated and UV-Vis spectra of the supernatants before and after the reactions were collected. MNPs-PLL-TR, MNPs-Tf-TR and MNPs-Stv-TR were washed several times with bi-distilled H_2O and dried under vacuum.

PMA-induced differentiation of THP-1 cell line: Monocyte-differentiated macrophages: 10^6 monocytes/well of THP-1 cell line in RPMI 1640 w/o PhR, supplemented with 10% FBS and 1% Pen Strep, were plated in 6-wells plate and treated with PMA 100 ng/mL (2mL/well). After 48h incubating at 37°C and 5% CO_2, cells were washed with PBS (3x 1mL/well) and incubated in complete RMPI w/o PMA. After 24h resting monocyte-differentiated macrophages were used for internalization experiments.

MNPs internalization: Monocyte-differentiated macrophages were incubated with MNPs-PLL-TR, MNPs-Tf-TR or MNPs-Stv-TR dispersions in RPMI w/o PhR and w/o FBS (2 mL/well), at starting concentrations of 1 mg/mL, filtered on 3 μm filters. Cells incubated in the same condition w/o MNPs were used as negative

controls. After 2h incubating, not internalized MNPs were removed by three washings with PBS.

Confocal Fluorescence Microscopy analysis: Cells were fixed for 10 min at rt with paraformaldehyde and sucrose solution at 4% in PBS (1mL/well). After 3 washings with PBS, cells were treated 10 min with glycine aqueous solution (200 mM, 1 mL/well) and, after washings with PBS, the cell nuclei were stained with Hoechst solution (5 μg/mL in bi-distilled H_2O) for 5 min at rt. Coverslips, contained in each well, were mounted on slides with a glycerol solution at 90% in PBS and confocal fluorescence analysis were performed.

Prussian Blue staining: After fixing cells in cooled MeOH, 2 mL of an aqueous solution containing potassium ferrocyanide (4%) and HCl solution (4%) were added to each well (1mL/well). After 15 min, three washings with bi-distilled H_2O were performed and cell nuclei were stained for 2 min with Nuclear Red aqueous solution at 2%. After washings with bi-distilled H_2O, coverslips were mounted on slides using Entellan® mounting medium and microscopic images were collected.

Quantification of MNPs-engulfed macrophages by flow cytometry: 2 mL of Accutase® solution were added to each well. After incubating 20 min, detached cells were moved to falcon tubes and centrifuged 10 min at 1200 rpm. Pellets were dispersed in 200 μL of paraformaldehyde solution at 4% in PBS and flow cytometry analysis were performed.

6. Fe_3O_4@SiO_2-LIPODEPSIPEPTIDE NANOSYSTEMS WITH ANTIMICROBIAL ACTIVITY

6.1 INTRODUCTION

This research work is focused on the development of new nanosystems for the treatment of infectious diseases. The introduction of bioactive compounds, deriving from bacterial secondary metabolism, on the magnetite-based nanoparticles can lead to the achievement of multifunctional tools for fighting pathogenic microorganisms. Two molecules belonging to the lipodepsipeptides family, syringomycin E and syringopeptin 22A, have been selected as the antimicrobial compounds for the development of these nanosystems. This work has been carried out in collaboration with the research group led by Prof. Ingeborg Grgurina at the Department of Biochemical Sciences - Sapienza University of Rome.

6.1.1 Lipodepsipeptides from *Pseudomonas syringae* pv. *syringae*

Lipodepsipeptides represent a class of phytotoxic secondary metabolites produced by some bacteria, including the phytopathogenic Gram-negative bacteria *Pseudomonas syringae* pv *syringae*. These compounds act as virulence factors for the bacteria since they increase the disease severity in the affected plants, inducing cell necrosis.[179] These molecules are synthesized via the non-ribosomal mechanism of peptide synthesis.[180] A lipid tail linked to a peptide moiety is the general feature of a lipopeptide. The presence of a macrocycle, composed of a variable number of residues, closed with an ester bond characterizes the structure of the cyclic lipodepsipeptides produced by *P.s* pv. *syringae*.[181] The peptide moiety contains amino acids differing from the canonical ones, modified either in the side chain or in the stereochemistry or both. According to the number of residues composing the peptide moiety, two subgroups can be distinguished.

Lipodepsinonapeptides present nine residues involved in the formation of the lactone macrocycle; they include syringomycins (SRs), syringotoxin, syringostatin and pseudomycin. The other group is characterized by a peptide moiety of 19 to 25 residues and includes syringopeptins (SPs). Most of the AA have hydrophobic features and the lactone macrocycle is composed of eight residues.[180,181]

Lipodepsipeptides have attracted great interest for medical applications due to their high biological activity against several pathogenic and non-pathogenic microorganisms; particularly, these compounds have shown fungicidal and bactericidal activity.[182] The peculiar amphiphilic character of the lipodepsipeptides is the basis of the antimicrobial activity since it allows the interaction with cell membranes; the insertion of lipopeptides into the lipid bilayer causes pore formation, leading consequently to membrane depolarization and cell death.[183] The haemolytic activity of red blood cells of some of these compounds, especially SRs, limits the *in vivo* applicability; however, this phenomenon probably does not represent a serious health risk due to the enzymatic degradation of SRs during the digestive process which reduces their bloodstream circulation.[184]

6.1.1.1 Syringomycin E

Syringomycins belong to the cyclic lipodepsinonapeptide class since they are composed of a lactone macrocycle, containing nine amino acids, bound to a hydrophobic 3-hydoxy fatty acid. The length of the lipid tail differentiates three forms of SRs, named SRA_1, SRE and SRG; SRE represents the most abundant one and it is characterized by the 3-hydroxydodecanoyl side chain bound to the N-terminal L-Ser residue. This AA is also involved in the macrocycle formation since it is linked by an ester bond with the C-terminal L-Thr(4-Cl) residue, which plays an important role in the biological activity, but it is sensitive to hydrolysis.

As shown in the SRE structure depicted in Figure 6.1-1, several D-residues and modified amino acids form the peptide moiety, such as the 2,4-diaminobutyric acid (Dab), 2,3-dehydroaminobutyric acid (z-Dhb) and L-3-hydroxyaspartic acid (L-Asp (3-OH)).

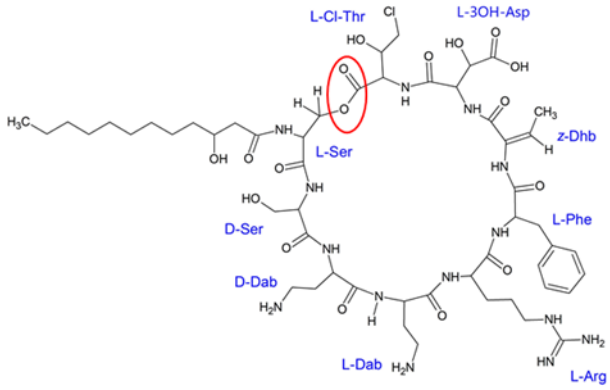

Figure 6.1-1: Chemical structure of syringomycin E, highlighting in red the lactone.

The antimicrobial activity of syringomycin is due to its insertion into the cell membrane which causes the formation of cell pores, freely permeable to monovalent and bivalent cations. Particularly, an increased flux of K^+, H^+ and Ca^{2+} has been demonstrated. This process produces both the collapse of the pH gradient through cell membrane and the activation of intracellular signalling pathways, consequently leading to cell death.[185] The ion-pore forming properties of SRE are influenced by the amount and the type of sterols in the target membrane and they are triggered by the aggregation process of SRE monomers in six-membered self-assembled structures which form the membrane channels.[186]

Concerning the antimicrobial activity, SRE has shown high antifungal activity towards filamentous fungi, such as *Geotrichum candidum*, and yeasts, such as *Rhodotorula pilimanae*; it also causes growth-inhibitory effects against the clinically important fungi *Candida spp* and *Aspergillus spp.*[187]

6.1.1.2 Syringopeptin 22A

Syringopeptins are characterized by a peptide moiety made up of 22 (SP22) or 25 (SP25) amino acids, predominantly Val and Ala. The lipid tail of 3-hydroxylated fatty acid chain, containing 10 or 12 carbon atoms, differentiates the two forms of SP22, respectively referred to as A and B. In SP22A, whose structure is shown in Figure 6.1-2, the N-terminal residue z-Dhb is acylated by the 3-hydroxydecanoic acid while the C-terminal Tyr residue is involved in the formation of the eight-membered lactone ring with a D-*allo*-threonine (D-a-Thr) residue.

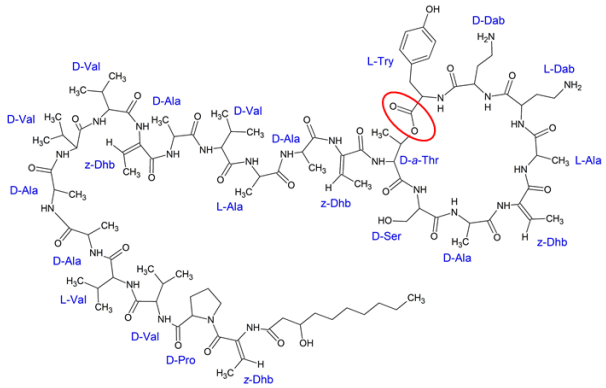

Figure 6.1-2: Structure of syringopeptin 22A highlighting the lactone in the macrocycle.

The basic mechanism of the biological activity of SP22A is similar to that of SRE: the amphiphilic character of SP22A allows the insertion into the cell membrane, forming pores and promoting the transmembrane ionic flux, especially Ca^{2+}, which causes cell death.[188] SP22A displays antibiotic activity against several Gram-positive bacteria and fungi, for instance *Bacillus megaterium* and *Botrytis cinerea*, presenting some differences in the antimicrobial spectrum as compared to SRE. Actually, SP22A is a very interesting bioactive compound since it shows antimycobacterial properties inhibiting the growth of *Mycobacterium smegmatis*, which is a non-pathogenic surrogate of *Mycobacterium tuberculosis*.[188,189]

6.2 CHAPTER OBJECTIVES

The development of new tools with antimicrobial effects is always a challenge in the perspective of fighting pathogenic and resistant microorganisms. Due to their biological activities, lipodepsipeptides can be interesting compounds for this purpose.[182] However, their chemical lability, due to the presence of the lactone macrocyclic moiety, and their haemolytic action have limited their medical applications. The immobilization of these compounds on nanoparticles could help to protect them and increase their stability. Moreover, the conjugation to nanoparticles could enhance the biological activity of antimicrobial drugs thanks to the physicochemical properties of nanomaterials, as already demonstrated for other bacterial antimicrobial peptides.[190] Thus, a lower concentration of the bioactive molecules can be utilized, consequently reducing the side effects. Furthermore, the peculiar properties of MNPs make them interesting carriers of the antimicrobial compounds for the achievement of multitasking nanosystems. For instance, these nanoparticles can be used *in vitro* for targeting and separating the microorganisms while *in vivo* they might allow the magnetic focusing into the infected area, enabling the imaging and the treatment of the infection.

For these reasons, the development of new nanosystems based on Fe_3O_4@SiO_2 MNPs functionalized with the two compounds, SRE and SP22A is the main aim of this research work. Moreover, there are no examples in the literature concerning the conjugation of these compounds on nanosystems, despite their interesting and promising biological activity.

To perform the conjugation of SRE and SP22A exploiting their peptide moiety, Fe_3O_4@SiO_2 MNPs can be first activated with the amino silane APTES and the polyelectrolyte poly-L-aspartic acid. The antimicrobial activity of the functionalized nanosystems can be estimated by preliminary *in vitro* growth inhibition assays on yeast cultures of *Rhodotorula pilimanae*.

At the same time, the internalization of the engineered nanosystems into human immune cells might be an interesting objective. In fact, although immune cells are involved in defending the organism, destroying the pathogens by engulfing them, several microorganisms can survive inside those cells.[191] Hidden into the immune cells, pathogens become hard to treat by using standard therapy. The uptake of medicated nanoparticles inside the infected immune cells can facilitate the therapeutic applications, resulting a good strategy for fighting pathogens.[192] In this context, preliminary internalization experiments on monocyte-differentiated macrophages of MNPs-lipopeptides can help paving the way for treating pathogens directly inside the cells where they are hidden.

Figure 6.2-1 shows a schematic representation of the aims of this research work.

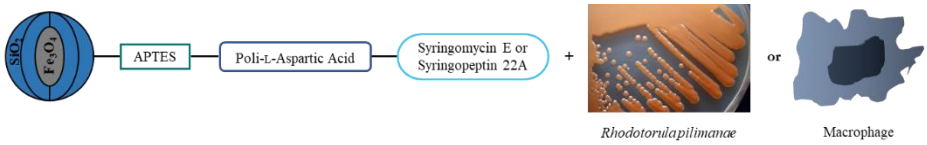

Figure 6.2-1: Representation of the nanoparticles Fe_3O_4@SiO_2 MNPs activated with APTES and poly-L-aspartic acid, functionalized with syringomycin E and syringopeptin 22A and used for *in vitro* experiments on *R. pilimanae* cell culture and monocyte-differentiated macrophages.

6.3 RESULTS AND DISCUSSION

The design and development of new promising nanosystems based on Fe_3O_4@SiO_2 MNPs for therapeutic applications towards fungal infections are illustrated in this section. The production of the nanosystems loading two bioactive molecules belonging to the lipodepsipeptide family represented the starting point of this research work. The *in vitro* biological experiments on fungal cell cultures and monocyte-differentiated macrophages allowed to evaluate the antimicrobial activity and the potential applicability of the nanosystems.

6.3.1 Surface activation of Fe_3O_4@SiO_2 MNPs with APTES

The surface of Fe_3O_4@SiO_2 MNPs was activated with the heterobifunctional compound 3-aminopropyltriethoxysilane (APTES) exploiting the hard-hard interactions between silica shell and silicon, as already explained in section 3.1.1.1. As shown in Figure 6.3-1, nanosystems were stirred overnight at rt in an aqueous-alcohol solution containing APTES using ammonia as catalyst.[193] In this way, primary amino groups were introduced on the Fe_3O_4@SiO_2 MNPs enabling the further functionalization with a polymer exploiting APTES as the linker. After washing with EtOH, MNPs-APTES were dried and characterized.

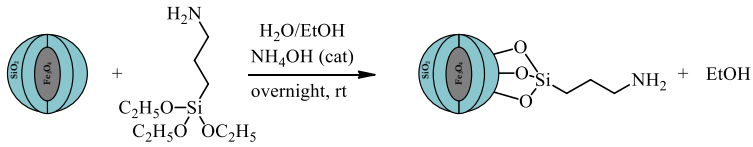

Figure 6.3-1: Scheme of the functionalization of Fe_3O_4@SiO_2 MNPs with APTES.

According to the FT-IR spectrum of MNPs-APTES shown in Figure 6.3-2, compared to that of bare Fe_3O_4@SiO_2 MNPs reported in Figure 3.3-12, the increase in the band at $\nu \approx 1180$ cm^{-1} and the presence of that at $\nu \approx 660$ cm^{-1} confirmed the conjugation of APTES on Fe_3O_4@SiO_2 MNPs. In fact, these vibrational bands were assigned to the stretching vibrations of Si-O and Si-C bonds, respectively.

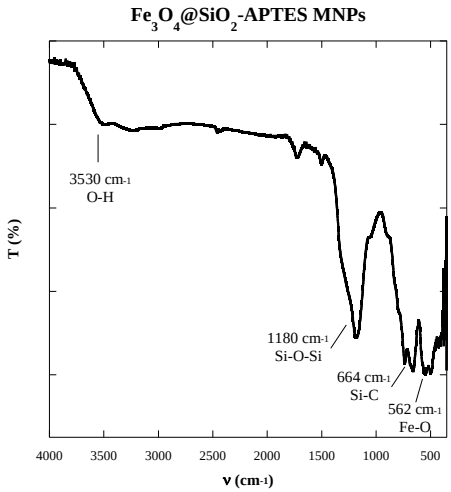

Figure 6.3-2: FT-IR spectrum of MNPs-APTES in which the vibrational bands were assigned to Si-O, Si-C and Fe-O bonds.

6.3.2 Functionalization with poly-L-aspartic acid

After the surface activation, MNPs-APTES were functionalized with the polyelectrolyte poly-L-aspartic acid (PLA). By introducing anionic groups, the colloidal features of the nanoparticles could be increased, enhancing their water dispersibility and minimizing the aggregation process among nanoparticles. Moreover, PLA could improve the biocompatibility and biodegradability of the entire nanosystem, being a low cytotoxic polymer.[194,195] Compared to the modification with single carboxylic acid molecules, the presence of several -COOH groups increased the numbers of suitable binding sites for the modification of MNPs with the bioactive molecules. The carboxyl groups could, therefore, be exploited for both the anchorage on nanoparticles and the functionalization with the lipodepsipeptides. Moreover PLA resulted an interesting polymer for biomedical application both as metal chelator and drug carrier, alone or in combination with other polymers like PEG and poly-ethylene oxide.[196-198]

As shown in Figure 6.3-3, the reaction was performed stirring the MNPs-APTES in PLA solution overnight at rt. The activation of the -COOH groups of PLA with EDC/NHS was carried out in PBS solution at slightly basic pH to improve the deprotonation of APTES ammine groups, thus facilitating amide bonds formation.

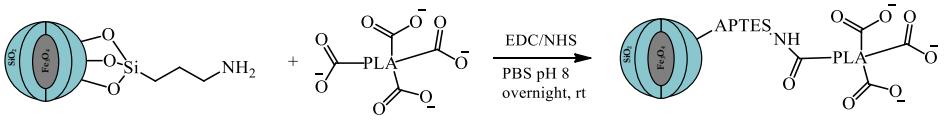

Figure 6.3-3: Reaction scheme of the functionalization of MNPs-APTES with PLA activating the -COOH with EDC/NHS.

The physicochemical characterization of the MNPs-PLA was performed by means of FT-IR. Analysing the spectrum shown in Figure 6.3-4, in addition to the vibrational bands belonging to the inorganic structure of the nanosystems, those at ν 3270 cm^{-1}, 1739 cm^{-1} and 1515 cm^{-1} could be assigned to the -OH and C=O groups of the free carboxylic groups and of the amide bonds, confirming the conjugation of the polymer.

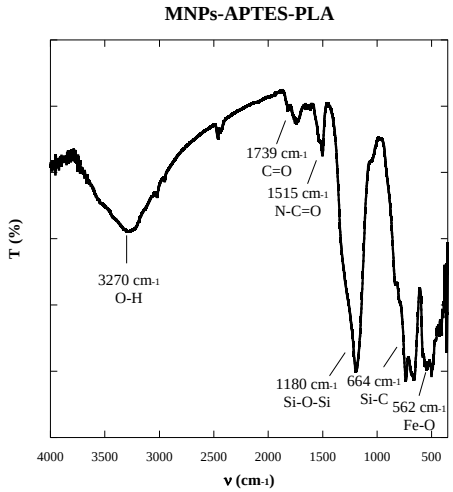

Figure 6.3-4: FT-IR spectrum of poly-L-aspartic acid, addressing the vibrational bands to the corresponding bonds.

6.3.3 Conjugation of syringomycin E or syringopeptin 22A

SRE and SP22A were selected for the modification of the nanoparticles due to their antibiotic activities; in fact, these lipodepsipeptides could act as therapeutic agents for the treatment of bacterial or fungal infections. Combining these properties with the diagnostic tool represented by the magnetic core of the Fe_3O_4@SiO_2 MNPs, multifunctional nanosystems could therefore be developed. SRE and SP22A were supplied by the group of Prof. Grgurina.

The peptide moieties of both lipodepsipeptides contained basic Dab residues, that could be exploited for the conjugation on MNPs-PLA. Since the functionalization reaction should be performed at basic pH, preliminary studies were planned to evaluate the stability of the compounds in these experimental conditions. In fact, the hydrolysis of the macrocyclic lactone and/or of the L-Thr (4-Cl) residue at basic pH could occur, compromising the antimicrobial activity of SRE and SP22A.[181]

6.3.3.1 Evaluation of SRE and SP22A chemical stability

The maintenance of the cyclic structure of SRE and SP22A in conditions similar to the experimental ones (120 min, pH 8, T 0°C), was evaluated by means of circular dichroism (CD) technique. In fact, a variation of the conformation of these compounds, derived from the lactone hydrolysis, could cause modifications in the CD spectrum due to the change in the intramolecular conformational constrains.

CD spectrum, recorded in the far-UV region, of SP22A aqueous solution maintained at 4°C is shown in Figure 6.3-5; it is characterized by optical bands at λ_{min} 213 nm and λ_{max} 233 nm. CD spectrum of SP22A - start (black line) corresponded to the starting aqueous solution of SP22A at pH 6.5. After increasing the pH to 8, CD spectra were recorded at times ranging from 0 min to 3 days. Analysing the experimental results, no significant differences could be found in

the CD spectra corresponding to SP22A solutions until 24h at pH 8. This result shows that the native conformation of SP22A in solution was maintained. Slight modification of the curve profile could be seen comparing the samples before (SP22A – start) and after (SP22A – 0 min) the pH increase; these modifications could be related to the change in the ionic strength [199] or to the beginning of the formation of tiny amounts of the open form of the peptide, confirmed by microbiological assays. After three days at pH 8, the CD spectrum of SP22A changed significantly, suggesting the opening of the lactone ring.

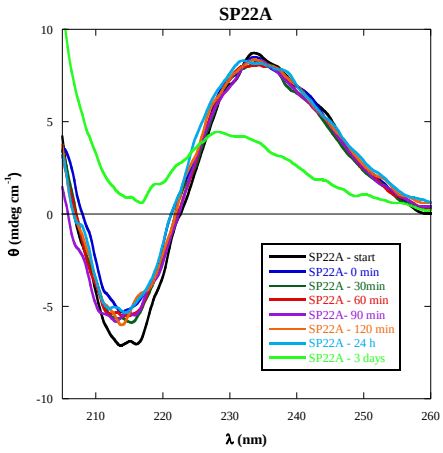

Figure 6.3-5: CD spectra of a SP22A solution maintained at 4°C recorded before (black line) and after increasing the pH. Blue line corresponded to SP22A – 0 min, acquired upon the addition of the buffer. The other CD spectra were recorded at 30 min (green line), 60 min (red line), 90 min (purple line), 120 min (orange line), 24 h (light blue line) and 3 days (light green line). The slight modifications in the CD spectrum of SP22A at 0 min compared to the start sample were due to the change of solvent while the variation of the curve profile in the CD spectrum of SP22A – 3 days was related to the lactone hydrolysis.

Conformational changes of SRE were evaluated in a similar way by means of CD spectra recorded in the far-UV region, maintaining the SRE solution at 4°C and increasing the pH to 8. The spectra, shown in Figure 6.3-6, were characterized by a broad negative band centered at λ_{min} 230 nm, in agreement with data reported in the literature.[200] The starting solution (pH 6.5) corresponding to sample SRE start produced a slightly different curve compared to those obtained after adding PBS buffer, due to the change of the solvent, as already reported in the literature for

other antimicrobial peptides.[199] Until 120 min from pH modification, the CD spectra were all comparable, suggesting the maintenance of the native conformation in these experimental conditions. The SRE solution was then heated at 37°C to facilitate the macrocycle opening; the CD spectrum recorded after 90 min presented significant differences in terms of intensity and λ_{min} shift attributable to conformational changes caused by lactone hydrolysis.

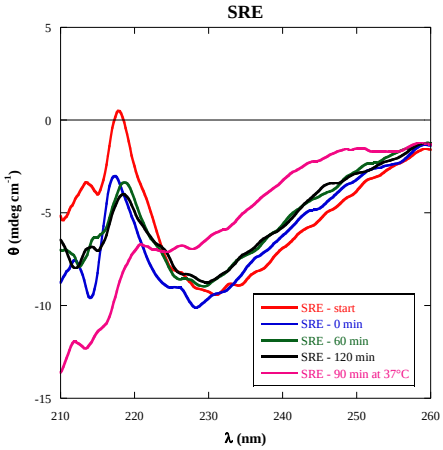

Figure 6.3-6: CD spectra of SRE solution maintained at 4°C recorded before (red line) and after increasing the pH. Blue line corresponded to SRE – 0 min, acquired upon the addition of the buffer. The other CD spectra were recorded at 60 min (green line) and 120 min (black line). The pink line corresponded to the SRE solution heated 90 min at 37°C (pink line). The slight modifications in the CD spectrum of SRE at 0 min compared to the start sample were due to the change of solvent while the variation of the curve profile in the CD spectrum of SRE – 90 min at 37°C was related to the lactone hydrolysis.

These experimental results suggested the maintenance of the conformational structure of SRE and SP22A in the conditions corresponding to 120 min at pH 8 and 0°C, planned for the conjugation reactions. However, in SRE at basic pH the hydrolysis of L-Thr (4-Cl) could also occur; this process could not be detected by CD analysis, but it could be evaluated by microbiological assays since it affected the antimicrobial activity of SRE, together with the lactone hydrolysis.

For these reasons, the further confirmation of the stability of SRE and SP22A was achieved by evaluating the antimicrobial effect of the solutions, used for CD analysis, by biological *in vitro* experiments on yeast cultures of *R. pilimanae*.

6.3.3.2 Functionalization of nanosystems with SRE and SP22A

The functionalization of the nanosystems was therefore carried out in a one-step reaction, stirring the MNPs-PLA with EDC/NHS solution, for the activation of -COOH groups, and SRE or SP22A solution, as shown in Figure 6.3-7. The reactions were performed in PBS solution at pH 8, maintaining the T at 0°C for 2 h, to allow the formation of amide bonds. The covalent bonds were formed in addition to the spontaneous ionic interactions occurring among negatively charged MNPs-PLA and positively charged lipodepsipeptides.

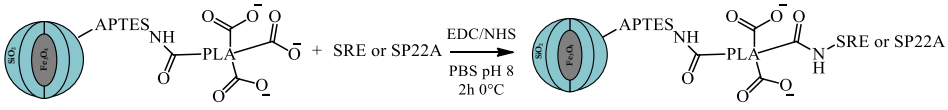

Figure 6.3-7: Scheme of the functionalization of MNPs-PLA with SRE or SP22A activating the -COOH groups with EDC and NHS.

After separating the nanosystems, the solutions corresponding to the supernatants and the following three washings with H_2O were used for the further quantification of the loading. The products MNPs-SRE and MNPs-SP22A were finally dried under vacuum. The quantification of the immobilization yields, by evaluating the residual amount of the lipodepsipeptides in the supernatants was performed by the group of Prof. Grgurina. Briefly, the supernatants were applied on a Sep-Pak C_{18} Cartridge conditioned according to the manufacturer's instructions. EDC and NHS were removed eluting with the mixture MeOH:H_2O 5:95 containing 0.1% TFA while the SP22A and SRE were eluted with the mixture acetonitrile:isopropyl alcohol 80:20 containing 0.1% TFA. Their amounts were estimated by means of UV-Vis spectroscopy using ε_{280}=1280 M^{-1} cm^{-1} and ε_{240}=9940 M^{-1} cm^{-1} for SP22A and SRE, respectively. The immobilization yields

resulted in 36.5% for MNPs-SP22A and 55% MNPs-SRE, corresponding to 36 μg SP22A/mg of MNPs-SP22A and 18 μg SRE/mg of MNPs-SRE.

6.3.3.3 Evaluation of the covalently and ionically bound SRE and SP22A

To study the nature of the binding among the lipodepsipeptides and the nanosystems, MNPs-SRE and MNPs-SP22A were treated with KCl 0.2 M. In this way, the estimation of the amount of covalently bound and electrostatically interacting lipodepsipeptides can be achieved; in fact, the fraction of SRE and SP22A bound by ionic interactions could be detached using the high ionic strength solution. After the treatment, MNPs-SRE and MNPs-SP22A were separated and the lipodepsipeptides present in the supernatants were quantified by UV-Vis spectroscopy, as previously described. The ionically bound amount was estimated of 1% and 25% for SP22A and SRE respectively.

6.3.4 In vitro growth inhibition assays on *R. pilimanae*

The antimicrobial effects of MNPs-SRE and MNPs-SP22A were evaluated by *in vitro* growth inhibition assays on *R. pilimanae* cell cultures. This yeast is commonly used to assess the antifungal activity of the compounds since it is a non-pathogenic microorganism easily to growth. The experiments, performed by the group of Prof. Grgurina, were carried out plating the yeast in Petri dishes covered by PDA medium. The plates were treated with serial 1:1 dilutions of SRE or SP22A, free or bound to the nanosystems, or of MNPs-PLA and the yeast cultures were growth for 48 h at 25°C. For the assays, concentrations of free antibiotic compounds comparable to those of SRE and SP22A bound to the nanosystems, quantified as described in section 6.3.3.2, were used. Moreover, calibration curves correlating the diameter of the inhibition halos with the

concentration of free SRE and SP22A were used for estimating the antibiotic activity of the nanosystems.

The results of the growth inhibition assays on *R. pilimanae* are shown in Figure 6.3-8. The bare nanoparticles MNPs-PLA did not produce any antimicrobial effect on yeast growth, proving the biocompatibility of these nanosystems. The dilutions of free SRE and free SP22A caused growth inhibition and also MNPs-SRE and MNPs-SP22A inhibited yeast growth, especially the first nanosystem. In fact, around the deposition points of free compounds or nanoparticles, yeast colonies were not able to growth, as demonstrated by the presence of inhibition halos. Since the absence of antimicrobial effects of MNPs-PLA, the antibiotic activity of MNPs-SRE and MNPs-SP22A could only be derived from the bound lipodepsipeptides. These experimental evidences, on one hand, confirmed the success of the functionalization process of the nanosystems and, on the other hand, proved their antifungal activity.

Comparing the inhibition halos produced by MNPs-SRE with those of free SRE, an improvement in the antifungal activity was achieved after immobilization; in fact, serial dilutions of MNPs-SRE, up to the ninth one, caused growth inhibition while the free SRE displayed antimicrobial activity up to the seventh serial dilution. Once bound to the nanoparticles the antibiotic activity of SRE was three times increased. This evidence agreed with the already reported *in vitro* enhancement of the biological effects for other bacterial antimicrobial peptides after conjugation on nanoparticles, for instance vancomycin.[190] In fact, the extended surface area of NPs allowed to concentrate the bioactive molecules, increasing its local amount, which could act in a more effective way, resulting in the enhancement of the antimicrobial activity compared to the free compound.

Concerning MNPs-SP22A, the antimicrobial activity on *R. pilimanae* was not so evident as for MNPs-SRE, since only the most concentrated solution, deposited on the point M in the plate, produced growth inhibition effects. Compared to free

SP22A, the immobilization did not improve the antimicrobial activity of the lipodepsipeptide. However, preliminary results on liquid cultures of *Candida albicans* confirmed good antifungal activity of MNPs-SP22A; in fact, the estimated minimum inhibitory concentration (MIC) values were 8 μM and 32 μM for MNPs-SP22A and SP22A respectively.

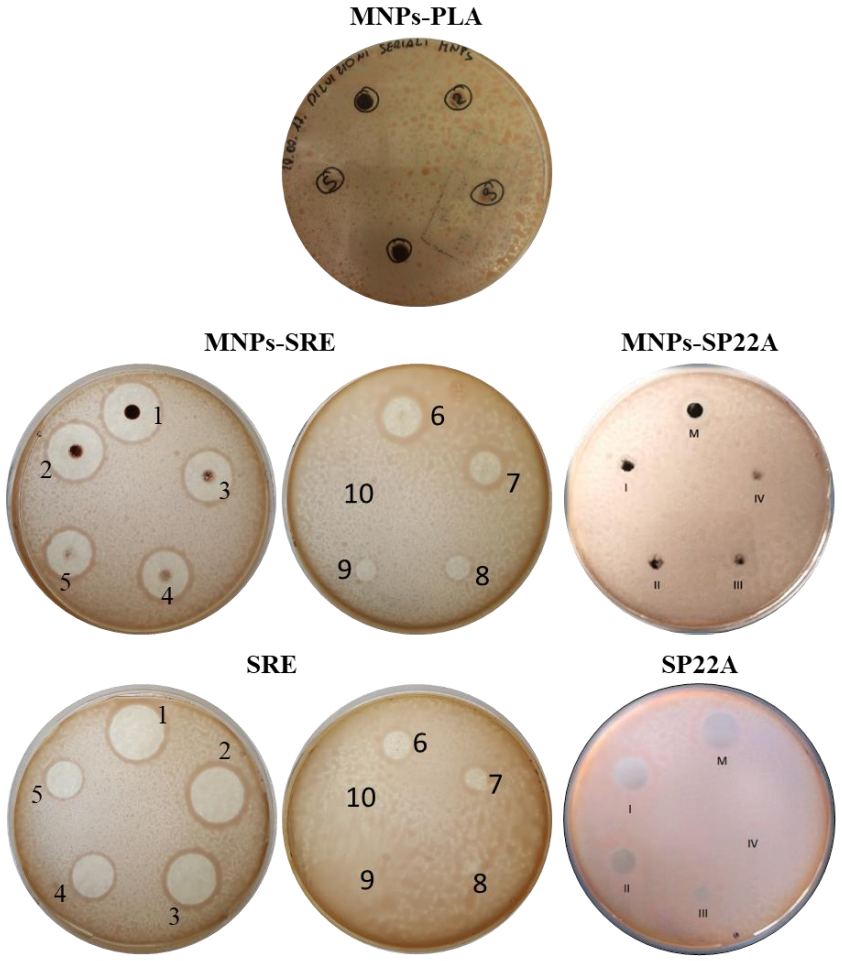

Figure 6.3-8: Growth inhibition assays on *R. pilimanae*. Free SRE and SP22A and the nanosystems MNPs-PLA, MNPs-SRE and MNPs-SP22A were tested, incubating the plates for 48 h at 25°C. The numbered points correspond to serial dilutions of the free or MNPs-bound compounds (decreasing concentration from 1 to 10 for SRE or from M to IV for SP22A). Inhibition halos were clearly visible in the plates treated with SRE, SP22A and MNPs-SRE. For MNPs-SP22A only the most concentrated solution (M) had growth-inhibitory effects while MNPs-PLA were not cytotoxic.

Supernatants and washings, collected during the functionalization reactions, were also assessed by microbiological assays on *R. pilimanae*. The results confirmed the presence of unreacted bioactive molecules in the reaction supernatants and their absence in the washing solutions; in fact, the first produced yeast growth inhibition, while the second did not show antimicrobial effects.

The antifungal activity of MNPs-SRE could derive from lipodepsipeptide both ionically interacting and covalently bound to MNPs-PLA. After the detachment of the ionically bound SRE treating the nanosystems with KCl solution, the MNPs-SRE were still active. Even if covalent functionalization ensured higher stability to the nanosystems, avoiding the undesired release of the bioactive molecules in physiological environment, the ionically interacting fraction could be more easily accessible; this binding, in fact, could provide the compound readily available for the interactions with membranes, allowing a more effective performance of the antimicrobial activity.

Therefore, MNPs-SRE and MNPs-SP22A showed interesting antimicrobial activity paving the way to new promising nanosystems for the treatment of fungal infections. According to the biological effects of SRE and SP22A against other microorganisms, in addition to the imaging properties of the magnetite core, those nanosystems might be suitable for both diagnosis and treatment of other kinds of infection diseases, involving for instance bacteria or mycobacteria.

6.3.5 *In vitro* internalization in human immune cells

Considering that MNPs-SP22A displayed antifungal activity it was reasonable to hypothesize that the applicability of these bioactive nanosystems could be extended to other microorganisms, including pathogenic ones. Since some microorganisms, once phagocyted by immune cells like macrophages, are able to survive inside them in a latent state, the internalization of medicated nanoparticles

into the infected cells could allow *in loco* therapeutic treatments.[191,201] The uptake of the nanosystems loading antimicrobial drugs by immune cells might, in fact, lead to the intracellular co-localization of the therapeutic tool and the pathogens, enabling their treatment where they are safely hidden. In this context, some studies on medicated nanoparticles performing a therapeutic action into infected immune cells can be found in the literature; particularly, the examples concern nanosystems functionalized with commercially available antimycobacterial drugs internalized into *M. tuberculosis*-infected macrophages.[192,202]

For these reasons, studies on the internalization of the MNPs-SP22A nanosystems into human immune cells were performed. These internalization experiments were carried out on monocyte-differentiated macrophages starting from THP-1 cell line, using the differentiation protocol already reported in 5.3.2.1. To reveal the nanoparticles during the *in vitro* experiments, the labelling with a fluorescent probe was first accomplished.

6.3.5.1 Labelling of MNPs-PLA with Texas Red-cadaverine

The polyelectrolyte PLA was labelled with a derivative compound of TR presenting a cadaverine moiety which enabled the formation of covalent amide bonds. The reaction, shown in Figure 6.3-9, was carried out for 1 h at rt, stirring the MNPs-PLA in a fluorescent probe solution using the carbodiimide chemistry. The conjugation of the dye to the nanoparticles conferred them red fluorescence, as confirmed by the spectrofluorometric analysis of MNPs-PLA-TR which exhibited an emission band centred at λ=608 nm.

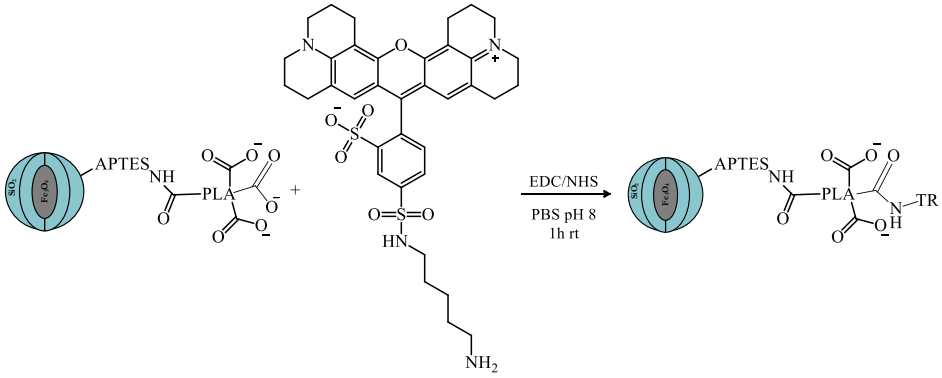

Figure 6.3-9: Reaction scheme of the labelling of MNPs-PLA with Texas Red-cadaverine.

After the labelling, SP22A was conjugated on MNPs-PLA-TR following the protocol previously described in section 6.3.3.2. SP22A was selected instead of SRE for its well-known cytotoxic effect towards *M. smegmatis*, belonging to *Mycobacteriaceae* family. This group contains several pathogens hard to treat, particularly *M. tuberculosis* which is able to hide and survive inside macrophages.

6.3.5.2 Internalization in monocyte-differentiated macrophages

In vitro biological experiments were performed to demonstrate the uptake of MNPs-PLA-TR and MNPs-SP22A-TR by monocyte-differentiated macrophages. THP-1 cell line was first differentiated treating the monocytes with PMA, as described in section 5.3.2.1. The macrophages were then incubated for 2 h at 37°C with dispersions of MNPs-PLA-TR or MNPs-PLA-SP22A-TR, filtered on 3 μm filters. The filtration was performed in order to remove big aggregates of nanosystems which can endanger cell vitality. Untreated cells, maintained in the same experimental conditions, were used as negative control. After incubation, cells were washed several times with buffer solution and fixed with paraformaldehyde solution. After staining cell nuclei, cells were analysed by confocal fluorescence microscopy.

The fluorescence images of cell samples are shown in Figure 6.3-10. Cells were identified by the nuclear blue staining with Hoechst, while nanosystems by the red spots deriving from TR conjugated to PLA. Comparing the images with control sample, it was possible to confirm that macrophages internalized MNPs-PLA-TR and MNPs-PLA-SP22A-TR since in both cell samples red fluorescent spots were detected. The intracellular localization of the nanosystems was confirmed by z-stack acquisition. According to the experimental evidences, the cells treated with MNPs-PLA-SP22A-TR showed red-fluorescence emission higher than macrophages incubated with MNPs-PLA-TR; several explanations could justify this result. For instance, a higher internalization of the lipodepsipeptide-functionalized MNPs could have happened, facilitated by the interactions between cell membrane and SP22A. Otherwise, the presence of the bioactive molecule could have increased the basal autofluorescence emission of the immune cells, triggering some metabolic pathways. However, the phenomena explaining this significant fluorescent enhancement need to be further investigated, evaluating the effect of free SP22A on the same cells.

Figure 6.3-10: Fluorescence images of monocyte-differentiated macrophages untreated (CTR, left) and treated with MNPs-PLA-TR (center) or MNPs-PLA-SP22A-TR (right) for 2 h at 37°C. Blue spots corresponded to cell nuclei stained with Hoechst, while intracellular red spots derived from TR of internalized MNPs. Images were collected by means of a confocal fluorescence microscope with a 100x oil immersion objectives lens. The images correspond to central planes (20-25/40 planes) of the z-stack acquisitions.

The successful internalization of nanosystems loading the antimicrobial compound SP22A into human immune cells could help developing new and efficient strategies for the *in loco* treatment of pathogens.

6.4 CHAPTER CONTRIBUTIONS

- Nanosystems loading the lipodepsipeptide SRE and SP22A were developed for the first time, conjugating the bioactive molecules to Fe_3O_4@SiO_2 MNPs activated with APTES and PLA.
- The immobilization of SRE and SP22A did not cause the loss of their biological activity since the MNPs-SRE and MNPs-SP22A produced growth inhibitory effects on *R. pilimanae* cell cultures; actually, the immobilization of SRE on MNPs-PLA increased three-times the antimicrobial activity, compared to free SRE.
- MNPs- SP22A labelled with the fluorescent probe TR-cadaverine were internalized by monocyte-differentiated macrophages, paving the way to promising treatments with medicated nanoparticles against pathogens directly inside cells.

6.4.1 Future perspectives

- Evaluate the antimicrobial activity of MNPs-SRE and MNPs-SP22A against other microorganisms, such as pathogenic bacteria, to extend the applicability of these novel nanosystems. Estimate the MIC values by microbiological assays in liquid batch cultures.
- Perform internalization experiments of MNPs-SP22A and free SP22A by monocyte-differentiated macrophages to understand the internalization mechanisms and evaluate the release/degradation of the nanosystems inside the cells.

6.5 ACKNOWLEDGMENTS

Prof. Ingeborg Grgurina and her group at Sapienza University of Rome for microbiological experiments. Prof. Maria Pia Donzello at Sapienza University of Rome for FTIR analysis. Dr. Valeria de Turris of centre for life nanoscience@Sapienza – Istituto Italiano di Tecnologia – for confocal fluorescence microscopy.

6.6 MATERIALS AND METHODS

Reagents, materials and equipment: All the chemical reagents were purchased by Sigma-Aldrich (Merck KGaA, Germany) and used without further purification. All the material used during *in vitro* biological experiments were purchased from Corning (Corning, USA). Permanent magnets made of Neodymium-Iron-Boron alloy, having a magnetic field of 0.3 T, were used for magnetic separations. The spectropolarimeter Jasco J715 was utilized for the circular dichroism experiments, using Suprasil® quartz cell for kinetic measurement and acquiring the spectra with Spectra Manager™ software. Steady-state fluorescence spectra were collected by Cary Eclypse (Varian) spectrofluorometer, equipped with the Xe lamp using Suprasil® quartz cell. Sep-Pak C_{18} Cartridge was supplied by Waters (USA). The experimental data were elaborated with the software Kaleidagraph (Synergy Software, USA). The fluorescence confocal analysis was performed at the Centre for Life Nanoscience IIT@Sapienza by means of the inverted microscope Olympus X73 equipped with 100X oil immersion objectives lens. The fluorescence images were collected by z-stack mode acquiring 40 planes divided by 0.2 μm, and were elaborated by ImageJ software.

Surface activation with APTES: MNPs-APTES: 400 mg of Fe_3O_4@SiO_2 MNPs were dispersed in 16 mL of bi-distilled H_2O and 40 mL of EtOH dissolving 4 mL of APTES (17 mmol) and 40 μL of NH_4OH were added to the dispersion. The mixture was mechanically stirred overnight at rt. MNPs-APTES were magnetically separated, washed with EtOH and H_2O and dried under vacuum.

Conjugation of PLA:MNPs-PLA: 400 mg of MNPs-APTES were dispersed in 20 mL of PBS (0.1 M pH 8). 20 mg of PLA were dissolved in NaOH and diluted to 10 mL with PBS (0.1 M pH 6) containing EDC (0.3 mmol) and NHS (0.3 mmol). The reaction was mechanically stirred overnight at rt. MNPs-PLA were magnetically separated, washed with H_2O and dried under vacuum.

CD studies on SRE and SP22A: CD spectrum of 1 mL of an aqueous solution of SP22A (0.36 mg/mL in bi-distilled H_2O) at 4°C. After mixing with 1 mL of PBS (0.2 M pH 8) CD spectra were recorded in the far-UV range at time ranging from 0 min to 3 days maintaining the solution at 4°C.

CD analysis of 1 mL of an aqueous solution of SRE (0.125 mg/mL in bi-distilled H_2O) at 4°C was performed. After the dilution with 1 mL of PBS (0.2 M pH 8) CD spectra were recorded in the far-UV range at time ranging from 0 min to 2 h maintaining the solution at 4°C. The solution was then heated at 37°C and after 90 min a CD spectrum was recorded.

Conjugation of SRE or SP22A: MNPs-SRE and MNPs-SP22A: 40 mg of MNPs-PLA were dispersed in 2.4 mL of PBS (0.2 M pH 8) dissolving EDC ($4.6* 10^{-5}$ mol) and NHS ($4.6* 10^{-5}$ mol). 2.4 mL of an aqueous solution of SRE (1.2 mg) were added to the dispersion and the mixture was mechanically stirred for 2 h at 0°C. After magnetic separation, 3 washings with bi-distilled H_2O were performed (1 mL each) and the MNPs-PLA-SRE were finally dried under vacuum.

The same protocol was used for the conjugation of SP22A, dispersing the MNPs-PLA in 1.5 mL of PBS containing EDC/NHS and adding 1.5 mL of the SP22A (4 mg) aqueous solution.

Quantification of SRE or SP22A on MNPs-SRE and MNPs-SP22A: Sep-Pak C_{18} Cartridge was used for the chromatographic purification of the supernatants of the functionalization reaction of MNPs-PLA with SRE or SP22A. The cartridge was conditioned with MeOH:H_2O 90:10 containing 0.1% TFA (9 mL) and then equilibrated with H_2O + 0.1% TFA solution (3x6 mL). The supernatants (3 aliquots of 1mL) were eluted with the desalting solution (MeOH:H_2O 5:95 containing 0.1% TFA, 3x3 mL) to remove EDC and NHS while the lipodepsipeptides were eluted with the solvent mixture ACN:isopropanol 80:20 containing 0.1% TFA (3x3 mL). The quantification of the lipodepsipeptides present in the eluted fractions was performed by UV-Vis spectroscopy using ε_{280}=1280 M^{-1} cm^{-1} and ε_{240}=9940 M^{-1} cm^{-1} for SP22A and SRE, respectively.

Treatment with KCl solution: 11 mg of MNPs-SP22A or MNPs-SRE were treated for 5 min with 800 µL of KCl 0.2 M and centrifuged for 15 min at 14 000 rpm at 4°C, repeating three times the procedure. The ionically bound SP22A or SRE were quantified in the supernatants by UV-Vis spectroscopy using ε_{280}=1280 M^{-1} cm^{-1} and ε_{240}=9940 M^{-1} cm^{-1} for SP22A and SRE, respectively.

Labelling with Texas Red-cadaverine: MNPs-PLA-TR: 100 mg of MNPs-PLA were stirred for 30 min at rt in 5 mL of PBS (0.1 M pH 6) dissolving EDC (8.7* 10^{-5} mol) and NHS (8.7* 10^{-5} mol). After magnetic separation the supernatant was removed and replaced by 5 mL of PBS (0.1 M, pH 8) containing TR-cadaverine (7.2*10^{-7} mol in 100 µL ACN). After 1h stirring at rt in dark, the MNPs-PLA-TR were magnetically collected, washed first with DMF and then several times with bi-distilled H_2O and dried under vacuum.

PMA-induced differentiation of THP-1 cell line: the same protocol reported in section 5.6 was used to obtain adherent macrophages.

MNPs internalization: Monocyte-differentiated macrophages were incubated with MNPs-PLA-TR and MNPs-PLA-SP22A-TR dispersions in PBS at starting concentrations of 1 mg/mL, filtered on 3 μm filters. Cells incubated in the same condition w/o MNPs were used as negative controls. After incubating 2 h at 37°C, not internalized MNPs were removed by three washings with PBS. Cells were fixed for 10 min at rt with paraformaldehyde and sucrose solution at 4% in PBS (500 μL/well). After 3 washings with PBS, cells were treated 10 min with glycine aqueous solution (200 mM, 500 μL/well) and, after washings with PBS, cell nuclei were stained with Hoechst solution (5 μg/mL in bi-distilled H_2O) for 5 min at rt. Coverslips, present in each well, were mounted on slides with a glycerol solution (90% in PBS) and confocal fluorescence analysis was performed.

7. ANTIBODY-FUNCTIONALIZED MAGNETIC NANOPARTICLES FOR THE DETECTION OF EPINEPHRINE

7.1 INTRODUCTION

This chapter is focused on the development of *in vitro* diagnostic applications of magnetic nanosystems based on Fe_3O_4@Cu@Au MNPs and Fe_3O_4@SiO_2 MNPs for the detection of epinephrine. This research work was carried out in the Nanobiotechnology for Diagnostics group (Nb4D) at IQAC-CSIC in Barcelona, led by Prof. M.-Pilar Marco.

7.1.1 Epinephrine

Epinephrine (EPI), also known as (-)-epinephrine or adrenaline, is a neurohormone that belongs to the catecholamine family, including also other important neurotransmitters such as dopamine and norepinephrine (NorEPI). Structurally, EPI presents a catechol moiety and a *N*-methylaminoethanol system, as shown in Figure 7.1-1.

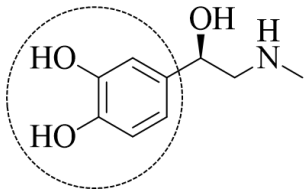

Figure 7.1-1: Chemical structure of epinephrine, highlighting the catechol moiety.

EPI is considered both a hormone and a neurotransmitter since it is a biogenic monoamine produced by the neuroendocrine cells in the adrenal medulla - chromaffin cells - and by certain neurons of the central nervous system, that have a primary role in the sympathetic nervous system.[203] Only the natural L-isomer is biologically fully active. Concerning its physicochemical properties, EPI is sensitive to light, high pH and heat; in fact, the first parameters causes its oxidation and degradation while high temperature produces racemization.[204]

The biosynthesis of EPI, as shown in Figure 7.1-2, starts from L-tyrosine and involves a series of enzymatic reactions and cofactors, that leads to the formation of the intermediate products L-DOPA, dopamine and NorEPI. The first step concerns the insertion of an -OH group into the aromatic ring to generate the catechol moiety and it is catalysed by the enzyme tyrosine hydroxylase. This reaction represents the rate limiting step because TH can be regulated by phosphorylation and by a feedback inhibition process of the final catecholamines.

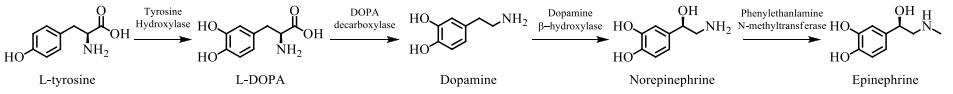

Figure 7.1-2: Epinephrine biosynthetic pathway.

Once EPI has been synthesized, it is stored in special granular structures in the chromaffin cells containing high amount of ATP or in dense core vesicles in nerve terminals and it is released after many physiological stimulations. EPI acts as a cellular messenger, circulating in the blood in free state, conjugated as sulphate or glucuronide or combined with albumin, and causes a wide variety of biological effects. Binding to its specific adrenergic receptors, situated in almost all body tissues and classified as α- and β- receptors depending on their localization, EPI can affect many metabolic pathways, particularly those related to lipid and glycogen. It can also act on blood pressure, smooth and skeletal muscle, peripheral nerves and hormone release. Moreover, its release controls the physiological reaction known as “fight-or-flight” response. EPI has a half-life of few minutes and it is metabolized by methylation or deamination through two major pathways involving the enzymes monoamine oxidase or catechol-O-methyltransferase. Its metabolites, vanillylmandelic acid, metadrenaline and vanillic acid, are excreted in urine and are often used as markers of alterations in catecholamine production caused by some pathologies.[203,205]

7.1.1.1 Clinical importance of epinephrine

Many diseases and altered physiological conditions are associated with elevated excretion of catecholamines, including EPI. It is known that the production of EPI increases in stressful conditions and, for this reason, it has been termed as an "emergency" hormone and it can be used for monitoring the stress level of a patient.

Several important diseases are correlated with alterations in EPI levels in biological fluids; the normal endogenous levels of EPI for healthy people are very low, <0.5 nM (100 pg/mL) in plasma and <190 nmol/day in 24h-urine.[206-208] Variations in its concentrations are caused by many factors such as, for instance, stress, exercise, smoking, pain and hypertension. The measurement of adrenaline levels is very helpful for the diagnosis of some pathologies, particularly catecholamine-secreting tumours. In fact, pheochromocytoma, paraganglioma, ganglioneuroma and neuroblastoma are tumours of the adrenal medulla normally associated with hyperproduction and excess of catecholamines in plasma and urine, including EPI and its metabolites. Some of these tumours are malignant and can lead to death, especially neuroblastoma for childhood.[209] The determination of biological levels of catecholamines, including EPI, is also important for the diagnosis of some neurodegenerative diseases, particularly Parkinson's disease, or mental disorders. Moreover, elevated excretion of EPI is associated with cardiovascular disease, for instance hypertension that can be related to the presence of pheochromocytoma. EPI has also an important role as drug; in fact, it is normally used to treat anaphylaxis and cardiac arrest.[207]

Since EPI triggers a variety of biological effects on all the body tissues and is involved in some important pathologies, its quantitative determination in biological fluids, such as plasma and urine, has become very important for clinical diagnosis.

7.1.1.2 Detection methods for EPI in the literature

Due to the low concentration of EPI in biological fluids, very sensitive analytical methods are required for its detection. Chromatographic techniques are the most sensitive techniques since high-performance liquid chromatography (HPLC) with electrochemical or fluorescence detection or HPLC coupled to tandem mass spectrometry (LC-MS/MS) can reach limit of detection (LOD) values ranging from pM to nM.[207,210,211] Electrochemical methods are mainly used for the detection of EPI thanks to the possibility of exploiting the electroactive behaviour of the catecholamine at certain potentials.[212] One limitation of this kind of readout is the presence of other compounds interfering during the detection process, especially ascorbic acid or drugs, such as paracetamol. Modifications of the electrode can improve the sensitivity of the electrochemical detection achieving LOD values ranging from nM to μM.[213]

For these reasons, sample pre-treatments, pre-concentration or derivatization are often needed. Liquid-liquid or solid-phase extractions with C18 column or Sephadex® G-10, cation-exchange resin and alumina are some of the techniques used for non-selective preparation of the sample.[207,214] More selective strategies concern the use of boronated gels or other platforms immobilizing boronic acid since this compound is able to form a stable complex with the catechol moiety of the catecholamines, allowing their almost selective extraction. Biosensors, especially based on amperometric detection, are also used for the detection of EPI; the immobilization of one or more enzymes able to oxidize the analyte - such as Horseradish Peroxidase (HRP) - and amplify the signal are used for the quantification of the analyte, leading to LOD values of few μM.[215]

Improvements in pre-treatment steps or in the detection methods are coming from nanotechnology. Some examples have been reported in the literature. Derivatization or modification of common measurement electrodes with nanomaterials, like noble metal nanoparticles or carbon nanotubes, are improving

the sensitivity of electrochemical detection, leading to LOD around 2-5 μM.[216,217] The use of functionalized nanoparticles for rapid and more selective extraction of the analyte has also been studied; for instance, MNPs modified with boronic acid derivatives are interesting tools to help the selective extraction process, achieving LOD around few ng/mL.[218,219] A more recent example concerns the use of magnetic nanoparticles functionalized with supramolecular molecules that could be used for loading EPI.[220] Also fluorescence detection of EPI can be more easily achieved using nanosystems; for instance, the quantification can be carried out monitoring the inhibition of the Fe_3O_4 nanoparticle-mediated production of a fluorescent compound in the presence of the analyte, leading to LOD values of few nM.[221]

7.1.2 Immunoassays and immunosensors

An immunochemical technique is based on the specific recognition phenomena between an antibody and an epitope, due to high chemical affinity that leads to the binding process. Usually, labels are needed in order to detect and monitor the immunochemical interaction, except for some label-free biosensors based on surface plasmon resonance (SPR) or impedance.[222,223] Chemiluminescent, fluorescent or enzymatic labels, like HRP or alkaline phosphatase, are the most common tools for revealing the antibody-epitope affinity. Among these bioanalytical methods, the ELISA and the immunosensors are widely used.

Concerning immunosensors, they are compact analytical devices in which the immunochemical interaction is detected and converted to an electrical signal by means of a transducer.[224] According to the sensing principle, the immunosensors can be distinguished in electrochemical, optical or piezoelectrical ones. In fact, the antibody-epitope binding can produce electroactive species or changes in the optical properties or in the total mass of the system; by means of a proper transducer, all these signals are finally converted in electric ones.

Among the electrochemical immunosensors, the amperometric ones are based on the measurements of current generated by electrochemical reaction and are promising tools for the detection and quantification of several kinds of analytes.[225,226] A common kind of amperometric immunosensor is based on an ELISA approach and utilizes screen-printed electrodes as the electrochemical system; the Ab is generally immobilized on the electrode or on another platform but maintained in intimate contact with the electrode. Due to the immunochemical reaction, electroactive species are produced, and the electric signal can be measured by amperometry.[227] Among the optical immunosensors, instead, those based on the SPR phenomenon are considered sensitive and powerful devices.[228]

Both label-free and labelled immunochemical methods usually rely on different formats depending on the molecular weight of the target. The most common configurations for ELISAs or other immunochemical techniques, such as electrochemical or optical immunosensors, are shown in Figure 7.1-3 from ref. [229]. The final measurable signal can be detected by different methods.

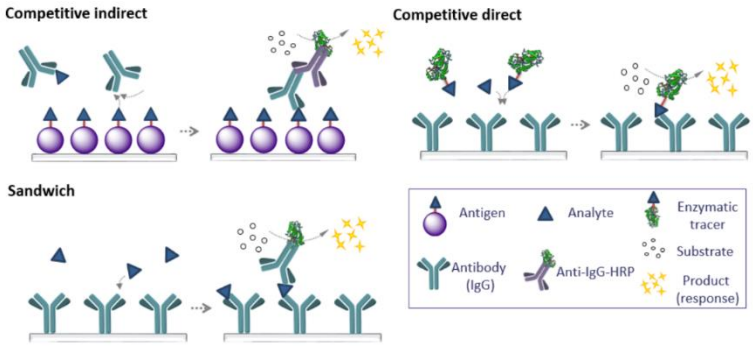

Figure 7.1-3 Schematic representation of the most common ELISA formats. **Competitive indirect assay**: the antigen, immobilized on the assay plate, competes with the free analyte for the binding site of the antibody. Adding the labelled secondary antibody, the spectrophotometric or electrochemical signal can be measured. **Competitive direct assay**: the immobilized antibody can recognize and bind the analyte or the enzymatic tracer competitor, which can catalyse the reaction of the substrate, giving the measurable signal. **Sandwich assay**: the analyte, presenting at least two epitopes, can be detected by a couple of antibodies, the capture one and the detection one, which produces the measurable signal [229].

Kinds of immunochemical assay:

1. For high molecular weight analytes, like proteins or whole bacteria, sandwich ELISA format is the most commonly used. Since the analyte presents at least two different epitopes and its dimensions are quite big, the detection can be achieved using a couple of antibodies: the capture antibody that is immobilized on the plate, and the detection antibody, that is added free in solution and produces the measurable signal proportional to the amount of the analyte, allowing its quantification.

2. For low molecular weight analytes, such as EPI, the sandwich format cannot be used. The detection can be achieved only using another molecule bigger than the analyte, that competes with it for the binding site of the antibody. Due to the presence of the competitor (generally named antigen (Ag)), that is usually a bioconjugate formed by a hapten and a protein, these immunochemical assays are referred to as competitive assays. Generally, a hapten can be defined as a small and not immunogenic molecule, with physicochemical properties similar to the target analyte, which can be bound to a different carrier protein according to the purpose. For the immunization step, highly immunogenic proteins like Keyhole Limpet hemocyanin (KLH) or Horseshoe Crab hemocyanin (HCH) are selected, while for the development of the immunochemical assays, other macromolecules such as proteins, polymers and enzymes are generally used.

The competitive immunoassays can be divided in direct and indirect formats. In the first one the competitor is a hapten covalently attached to a label, referred to as tracer, able to produce the signal. The indirect competitive assay requires the addition of a labelled secondary antibody, specific for the constant fraction of the primary antibody that produces the measurable signal.

Therefore, in the direct format the signal derives from the tracer while in the indirect one it is produced by the labelled secondary antibody. For these reasons, in both direct and indirect competitive immunochemical assays, the signal is

inversely proportional to the concentration of the analyte. This occurs because the analyte and the antigen compete for the binding site of the antibody, depending on their affinity constants (K_{aff}). The difference between the K_{aff} value of the analyte and the competitor determines the preferential formation of the analyte-antibody or competitor-antibody complex. $K_{aff\text{-}analyte}$ much higher than $K_{aff\text{-}competitor}$ means low amount of antibody binding the competitor and finally producing the measurable signal. For this reason, it is important to design and use competitors having K_{aff} similar to that of the analyte, in order to ensure a good competition between the Ag and the analyte, obtaining a significant signal.

The representation of the logarithm of the analyte concentration in front of the signal gives the typical sigmoidal curve of a competitive assay, as reported in Figure 7.1-4. Fitting the curve with a four-parameters equation, the analytical features of the immunochemical assay are obtained.

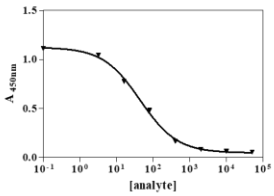

$$f(x) = Y_{min} + \frac{(Y_{max} - Y_{min})}{\left[1 - \left(\frac{x}{IC_{50}}\right)^{Hillslope}\right]}$$

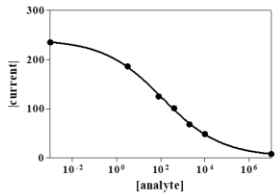

Figure 7.1-4: Inhibition curve typical of both direct and indirect competitive ELISA assays, measured by spectrophotometric (left side) or amperometric (right) techniques. In the curve fitting equation, the four parameters are IC_{50} (half maximal inhibitory concentration), Y_{max} (maximum value of absorbance or current), Y_{min} (minimum value of absorbance or current) and hillslope (slope of the linear part of the curve).

7.1.2.1 Immunochemical methods involving magnetic nanoparticles

Nanotechnology can bring improvements in the analytical features of immunochemical methods and practical advantages in the correlated experimental protocols too. The introduction of nanotechnology in bioanalytical techniques, in fact, can be very helpful to improve the reliability and the selectivity of immunoassays in the detection of some analytes, particularly those characterized by low molecular weight.[230] Using NPs, the performances of immunochemical devices can be enhanced thanks to the peculiar physicochemical features of nanomaterials. For instance, the high surface area can lead to the achievement of nanoplatforms with a high local quantity of biomolecules, such as antibodies, increasing the interactions with the analyte and facilitating the biorecognition process.

Among nanosystems exploitable in immunochemical assays, MNPs have received great attentions.[231] In fact, functionalizing MNPs with an antibody that specifically recognize an analyte might be a good idea to obtain a nanoplatform able to perform both the detection and the separation of the analyte from the matrix. The specific biorecognition element, as the antibody is, can be combined to the magnetic core of the nanosystems; after the analyte-antibody interaction, the application of the external magnetic field can lead to the separation and concentration of the target analyte. As reported in the literature, magnetic nanosystems have been used in immunochemical biosensors and assays for the detection of different kinds of analytes such as proteins, bacterial epitopes, viral antigens and small analytes like toxins, vitamins, biomarkers or drugs in complex matrices.[65,228,232,233]

For the immunochemical methods based on MNPs for the detection of small analytes the direct competitive format is easier to perform. As shown in Figure 7.1-5, the experimental procedure consists in mixing the MNPs functionalized with the appropriate specific Ab with the analyte and the enzymatic tracer. After

each step of the assay, the separation of the nanosystems can be achieved applying an external magnetic field.

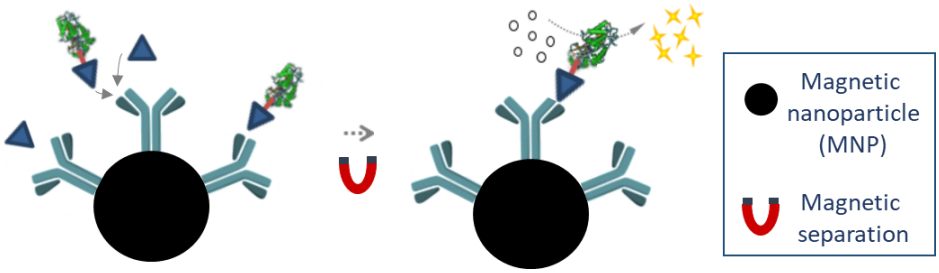

Figure 7.1-5: Scheme of the format of a direct competitive immunochemical assay based on antibody-functionalized magnetic nanoparticles. The nanosystems are separated after each step of the assay applying a permanent magnet.

In a magneto-ELISA format, the spectrophotometric detection can be achieved measuring the colorimetric signal produced in each well of the plate after 30 min MNPs and substrate solution reacting, separating magnetically the nanosystems. Concerning an amperometric magneto-immunosensor, instead, the electric signal can be obtained in few minutes; in fact, after depositing the MNPs on an electrode and holding them by means of a permanent magnet, a constant voltage (V) can be applied and the reduction current at a fixed time for all the samples can be measured immediately after the addition of the substrate solution. The inhibition curves achieved in these methods involving MNPs are the same as in the ELISA standard configurations, previously reported in Figure 7.1-4.

7.1.2.2 Available immunoassays for EPI

Immunochemical assays for the detection of EPI are not the most commonly used methods and are low discussed in the literature. Notwithstanding, many ELISA kits are commercially available for the determination of EPI alone or in combination with NorEPI. These competitive immunochemical assays are based on rabbit-antibodies recognizing the N-acyl derivative of EPI; therefore, the analyte needs to be first extracted using a cis-diol-specific affinity gel, then acylated to N-acyl adrenaline and finally enzymatically converted into N-acyl metanephrine. Although these assays are very sensitive, achieving for instance for Abnova EPI ELISA Kit (KA1882) LOD values < 1 ng/mL in urine and 0.01 pg/mL in plasma, they require a complex sample treatment.

Another example of commercially available ELISA kit (CatCombi ELISA – IBL International) is based on a sandwich format (rabbit anti-N-acyl metanephrine and alkaline phosphatase labelled antibody against biotin) able to detect both adrenaline and noradrenaline, after derivatization and biotinylating steps (sensitivity 0.3 ng/mL).[234]

It is described in the literature a patent concerning an immunochemical assay for the detection of EPI and NorEPI; it is based on an oxidation procedure converting the analytes into compounds that are not bound by the antibody. Therefore, the quantification can be achieved performing the immunoassay before and after the oxidation reaction.[235]

Immunochemical methods for EPI offer advantages compared to standard chromatographic techniques; they are easier to perform and more accessible to the laboratories since they required cheaper equipment. Moreover, they allow the simultaneous analysis of many samples or the contemporary detection of different kinds of analytes through multiplexed platforms.

7.2 CHAPTER OBJECTIVES

Considering the biological importance of the neurohormone EPI and its key role in many physiological and pathological conditions, the development of a sensitive, simple and rapid immunochemical method for its detection, avoiding sample pre-treatment and analyte derivatization, can be very useful.

The combination of the magnetic properties of MNPs, with the recognition ability of an Ab and the advantages of an electrochemical sensor might lead to the development of powerful analytical tools for this diagnostic purpose. The presence of an Ab able to recognize the free analyte without performing any modification or treatment could ensure the capture and the selective binding of the analyte, while the magnetic core of the nanoparticles could facilitate the separation and concentration steps. Moreover, a readout technique based on electrochemical detection could bring rapidity, reliability and simplicity to this kind of diagnostic system.

For all these reasons, the development of amperometric magneto-immunosensors for the detection of EPI is the aim of this research project. The diagnostic tools will be based on Fe_3O_4@Cu@Au MNPs and Fe_3O_4@SiO_2 MNPs functionalized with an antibody able to recognize and bind EPI. Rapidity, high simplicity and good sensitivity will represent the features of this analytical tool.

7.3 RESULTS AND DISCUSSION

In this section the experimental results concerning to the development of different kinds of immunochemical assays for the detection of EPI are presented and discussed. The evaluation of the immunoreagents, performed by standard ELISA configurations, was the starting point for the development of the MNPs-based amperometric immunosensors.

7.3.1 Development of the indirect competitive ELISA

7.3.1.1 Immunoreagents evaluation

EPI is a low molecular weight compound not immunogenic by itself. Thus, the preparation of an immunizing hapten is required. This hapten must be conveniently attached to an immunogenic protein to stimulate the immune response and to produce the specific antibodies against the selected molecule. The specific antibodies against EPI had been produced in the Nb4D group. Particularly, the designed and synthesized immunizing hapten for EPI had a nucleophilic group (X) at the spacer arm which was conjugated to the immunogenic protein HCH using *N*-succinimidyl iodoacetate (SIA) as a heterobifunctional crosslinker agent. The resulting bioconjugate HCH-SIA-EPI, known as immunogen, was used for immunizing three female New Zealand rabbits obtaining three different antisera: As334, As335 and As336. These antisera contain the pool of polyclonal antibodies developed against all the epitopes present in the immunogen.

In order to characterize the antisera produced against EPI, the preparation of competitor bioconjugates is required, as previously described. These compounds consist in binding the immunizing hapten, or other chemical compounds

structurally related with the target analyte known as competitor haptens, to carrier proteins different to the one used for immunizing. In this case, the immunizing hapten of EPI and a competitor hapten derived from NorEPI, which was chemically modified in the same way, were covalently attached to Bovine Serum Albumin (BSA) instead of HCH. The conjugates containing the hapten of EPI were considered homologous competitor conjugates, while those incorporating the hapten of NorEPI were heterologous ones. The degree of homology or heterology depends, on one hand, on the structure of the competitor hapten, and on the other hand, on the crosslinker agent used for the preparation of the bioconjugates. For some conjugates, a different heterobifunctional crosslinker agent was used, the *N*-succinimidyl 3-maleimidopropionate (N-SMP), increasing the structural differences between the immunogen and the corresponding competitor. Thus, four competitor conjugates, previously prepared in the Nb4D group, were selected for the development of the immunochemical assay for the detection of EPI. They were BSA-SIA-EPI, BSA-(N-SMP)-EPI, BSA-SIA-NorEPI and BSA-(N-SMP)-NorEPI and their structure is reported in Figure 7.3-1.

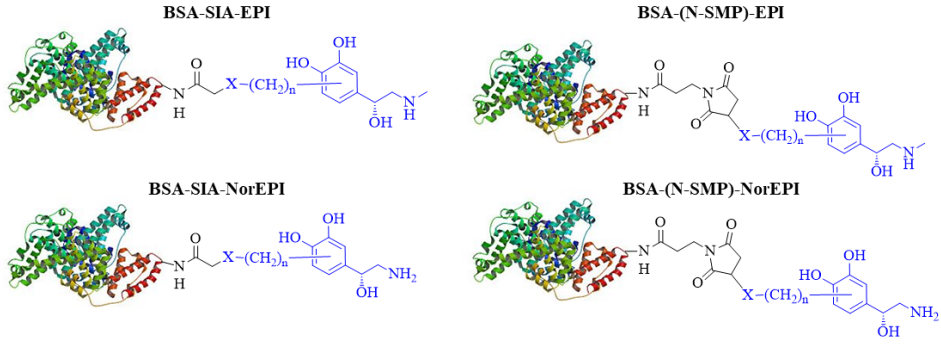

Figure 7.3-1: Structure of the homologous competitor conjugates BSA-SIA-EPI and BSA-(N-SMP)-EPI and heterologous ones BSA-SIA-NorEPI and BSA-(N-SMP)-NorEPI. The general structures of the haptens for EPI and NorEPI, in which X corresponds to a nucleophilic functional group, are highlighted in blue.

These conjugates were also previously characterized by spectrometric techniques, such as matrix assisted laser desorption ionization-time of flight mass spectrometry (MALDI-TOF-MS). The hapten density of the bioconjugates varied

from 8 to 23 residues of hapten per protein molecule. In this context, it is known that conjugates with lower hapten densities could lead to assays with better IC_{50} values [236]; therefore, this parameter should be considered in order to modulate the binding affinity between the antibody and the competitor conjugate or antigen.

The evaluation of the antisera raised against EPI was performed by different kinds of immunochemical assays. Firstly, two-dimensional (2D) ELISA assays were carried out for all the As-competitor combinations, varying the concentration of the Ag and the dilution of the As. The optimal As dilution and Ag concentration to be used subsequently in the competitive immunoassays were determined by performing the 2D checkerboard titration format. The typical curves obtained from a 2D ELISA are shown in Figure 7.3-2. The chosen combinations corresponded to those giving an A value close to 1 at 90% of the saturation curve.

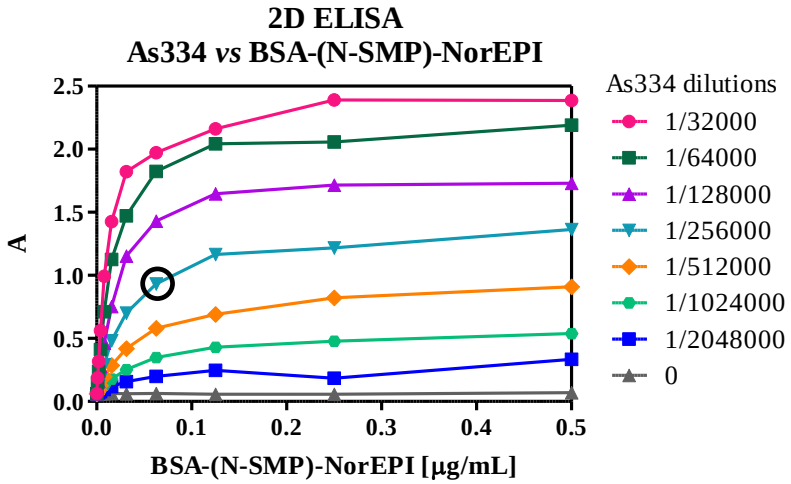

Figure 7.3-2: 2D-ELISA between As334 and the heterologous competitor BSA-(N-SMP)-NorEPI.

All the optimal As-Ag combinations were tested in competitive assays in which the analyte EPI was added in serial dilutions with concentrations ranging from 0 to 50 µM. The inhibition curves obtained in the competitive assays for As334, As335 and As336 with all the Ag are reported in Figure 7.3-3.

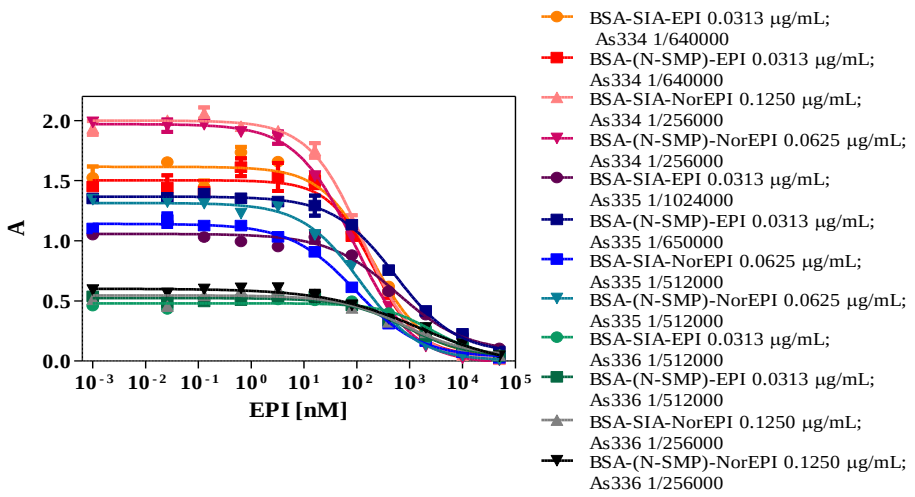

Figure 7.3-3: Sigmoidal inhibition curves achieved in the competitive ELISA assays performed among epinephrine, the four competitors - BSA-SIA-EPI, BSA-(N-SMP)-EPI, BSA-SIA-NorEPI and BSA-(N-SMP)-NorEPI - and As334, As335 or As336. At least three-well replicates were used for each assay.

Analysing the experimental data, As334 and As335 showed inhibition curves with better detectability of the analyte compared to As336, which was therefore discarded. After further optimization of As dilution and Ag concentration, the best results in terms of detectability were achieved using the As334 (dilution 1/256000) and the heterologous competitor conjugates BSA-SIA-NorEPI (40 ng/mL) and BSA-(N-SMP)-NorEPI (20 ng/mL). The corresponding inhibition curves are shown in Figure 7.3-4: while the analytical parameters are reported in Table 7.3-1. The values of IC_{50} obtained were both in the nanomolar range, but far from the concentration of EPI in biological samples, like urine or plasma [206,208].

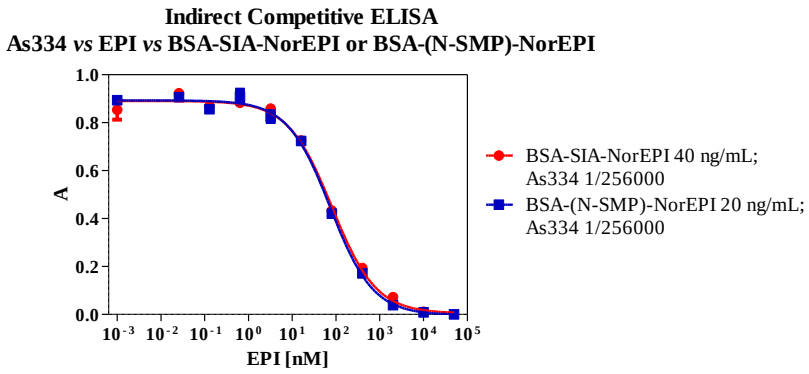

Figure 7.3-4: Inhibition curves obtained in the competitive indirect ELISAs among As334, epinephrine and BSA-SIA-NorEPI or BSA-(N-SMP)-NorEPI.

Table 7.3-1: Analytical parameters for the best As-Ag combinations in competitive ELISAs: absorbance values, hillslope, R^2 and IC_{50} are reported for the combinations As334 (dilution 1/256000) and BSA-SIA-NorEPI (40 ng/mL) or BSA-(N-SMP)-NorEPI (20 ng/mL).

	BSA-SIA-NorEPI 40 ng/mL As334 1/256000	**BSA-(N-SMP)-NorEPI 20 ng/mL As334 1/256000**
A_{max}	0.895 ± 0.015	0.893 ± 0.008
A_{min}	-0.004 ± 0.022	-0.002 ± 0.012
Hillslope	-0.757 ± 0.079	-0.889 ± 0.054
IC_{50} (nM)	72.5 ± 1.2	74.4 ± 1.1
R^2	0.991	0.997

Several physicochemical parameters were assessed with the aim of optimizing the features of the assay to improve its sensitivity.

7.3.1.2 Optimization of physicochemical parameters

Indirect competitive ELISA assays using EPI (0-20 μM), As334 (dilution 1/256000) and BSA-SIA-NorEPI (40 ng/mL) or BSA-(N-SMP)-NorEPI (20 ng/mL) were performed varying only one parameter of the competition step each time. The addition of a preliminary incubation step between As334 and the analyte and the variation of the competition time were initially studied. Then, the

modification of the buffer composition, assessing tween concentration, ionic strength and pH, was considered. In Figure 7.3-5 are reported the experimental results obtained changing these parameters.

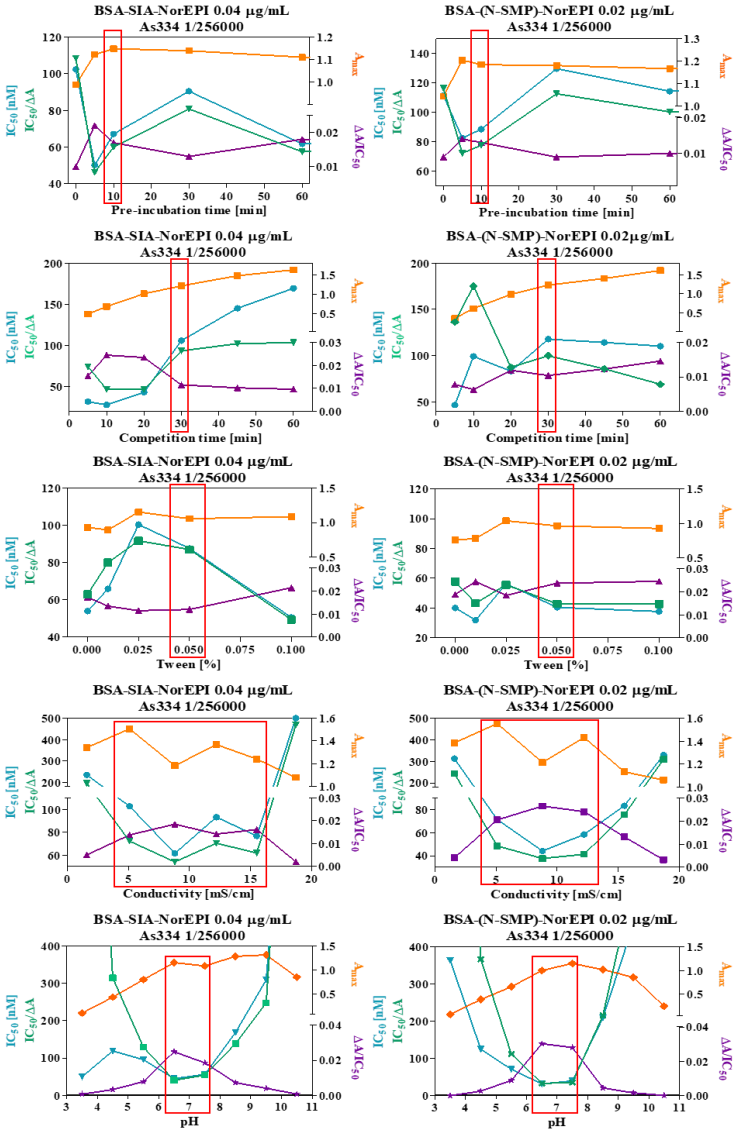

Figure 7.3-5: Effect of the variation of physicochemical parameters on indirect competitive ELISA of epinephrine and As334/BSA-SIA-NorEPI (left side) or As334/BSA-(N-SMP)-NorEPI (right side). In each graph the left axis indicates the value of IC_{50} (blue) and the $IC_{50}/\Delta A$ ratio (green) and the right axis the values of A_{max} (orange) and $\Delta A/IC_{50}$ (purple). Starting from the top the parameters are pre-incubation time, competition time, tween concentration, conductivity and pH.

The effect of the incorporation of a pre-incubation step of the As334 with EPI was evaluated from 5 min to overnight. According to the experimental results, the addition of a short pre-incubation step (10 min) improved the detectability of the immunoassay, comparing to the absence of pre-incubation (0 min). Overnight pre-incubation resulted in analyte degradation and, consequently, in the worsening of the analytical parameters of the immunoassay.

The competition time was assessed from 5 min to 60 min; short competition times caused a decrease in the maximum colorimetric signal, compared to long ones. Combining the 10 min preincubation step with competition, the best results were obtained maintaining the competition time at 30 min, as in the starting protocol.

The effect of changing the tween concentration was evaluated, using PBS solutions containing Tween 20 from 0% to 0.1%. Tween caused some variations in the analytical parameters of the immunoassay; however, considering that IC_{50} values were all in the nanomolar range, this parameter was maintained at 0.05%.

Ionic strength was assessed using PBST solutions with a conductivity value ranging from 5 mS/cm to 95 mS/cm. At conductivity higher than the reference value of 16 mS/cm there was a loss of the colorimetric signal and for this reason, the lower conductivity range from 2 mS/cm to 19 mS/cm was assessed. Both the immunoassays showed high stability at low conductivity and good detectability, particularly working in the range 5-16 mS/cm.

pH of the competition buffer was assessed using PBST solutions ranging from pH 2.5 to pH 11.5 and performing the ELISA experiments without the pre-incubation step. pH altered dramatically the detectability of the immunoassays in terms of both IC_{50} and A_{max}, probably due to the degradation of the analyte.[204] The stability of the immunoassays might be guaranteed working at almost neutral pH (6.5-7.5).

According to all experimental results an improvement on the IC_{50} value was achieved introducing a short pre-incubation step (10 min) and maintaining all the

other parameters at the reference values: 30 min for the competition step and PBST as the competition buffer, characterized by 0.05% Tween 20, conductivity of 16 mS/cm and pH of 7.5.

7.3.1.3 Optimized indirect competitive ELISA

Indirect competitive ELISA assays for EPI were developed using the As334 and BSA-SIA-NorEPI or BSA-(N-SMP)-NorEPI, as shown in Figure 7.3-6.

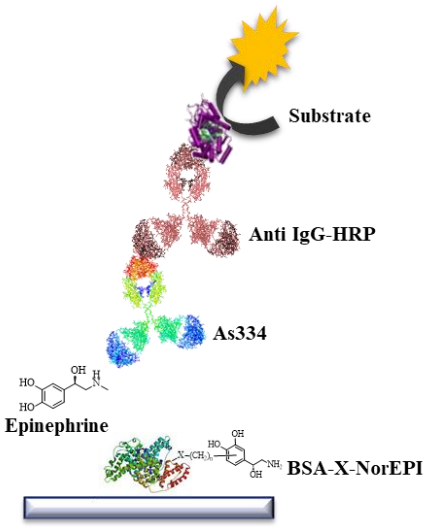

Figure 7.3-6: Scheme of the optimized indirect competitive ELISAs: the plate was coated with the heterologous competitor BSA-SIA-NorEPI or BSA-(N-SMP)-NorEPI (indicated as BSA-X-NorEPI) and As334 and epinephrine were added for the competition step. AntiIgG-HRP was used as a secondary labelled-antibody for the achievement of the colorimetric signal.

The features of the immunoassays are collected in Table 7.3-2 while the inhibition curves obtained from the optimized assays are shown in Figure 7.3-7. According to the experimental parameters both assays showed comparable detectability of EPI. After the optimization of the physicochemical parameters, that led to the introduction of a short pre-incubation step, the reached IC_{50} values were around 47±6 nM and 35±5 nM for BSA-SIA-NorEPI and BSA-(N-SMP)-NorEPI, respectively.

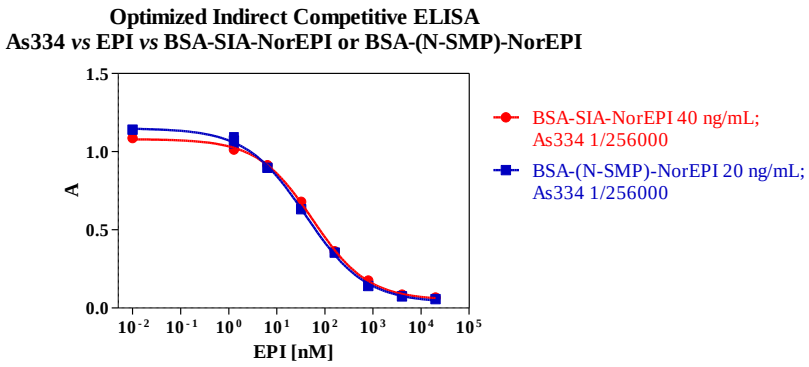

Figure 7.3-7: Inhibition curves of the optimized indirect competitive ELISAs among As334, epinephrine and BSA-SIA-NorEPI or BSA-(N-SMP)-NorEPI.

Table 7.3-2: Immunoassay features of the optimized indirect competitive ELISAs for epinephrine; information concerning immunoreagents, experimental parameters, A_{max}, A_{min}, R^2, IC_{50}, LOD and working range (WR) are summarized.

Experimental parameters	BSA-SIA-NorEPI	BSA-(N-SMP)-NorEPI
Ag concentration [ng/mL]	40	20
As334 dilution	1/256000	1/256000
Preincubation time	10 min	10 min
Competition time	30 min	30 min
Tween concentration	0.05 %	0.05 %
Conductivity [mS/cm]	5-16	5-12
pH	6.5-7.5	6.5-7.5
A_{max}	1.11 ± 0.04	1.07 ± 0.07
A_{min}	0.05 ± 0.01	0.04 ± 0.01
R^2	0.998	0.996
IC_{50} [nM] **IC_{50} [µg/L]**	47 ± 6 8.6 ± 1.0	35 ± 5 6.3 ± 0.7
LOD [nM]	2.1 ± 0.6	1.5 ± 0.3
WR [nM]	5-311	4-254

7.3.2 Development of the direct competitive ELISA

Once the immunoassay for the detection of EPI in an indirect competitive format was developed and optimized, the assay in a direct format was carried out, taking into account the immunoreagents and physicochemical conditions previously selected.

The first step was to address the preparation, characterization and immunochemical evaluation of the required enzymatic tracer (ET), HRP-(N-SMP)-NorEPI, which would be finally used for the immunoassays involving MNPs. As shown in Figure 7.3-8, the direct competitive ELISA assay was based on the competition between the analyte EPI and the conjugate HRP-(N-SMP)-NorEPI for the binding site of As334, adsorbed on the assay plate. The oxidation of the substrate solution was catalysed by the ET, avoiding the addition of the labelled secondary antibody and thus shortening the assay time.

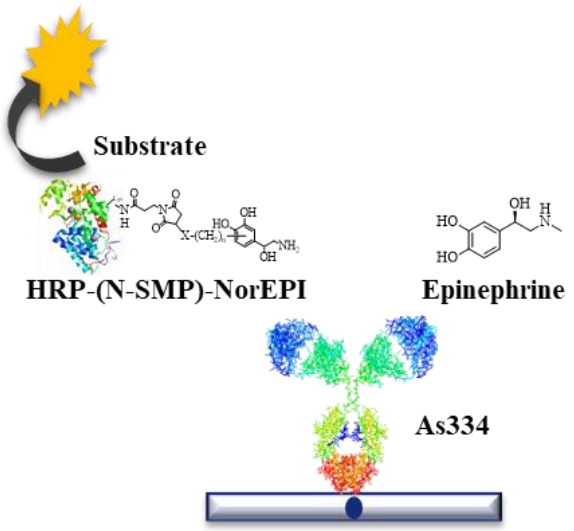

Figure 7.3-8: Scheme of the direct competitive ELISA for epinephrine: EPI and HRP-(N-SMP)-NorEPI competed for binding to As334, coating the plate. The oxidation of the substrate was catalysed by the enzymatic tracer that produced the colorimetric signal.

7.3.2.1 Enzymatic tracer HRP-(N-SMP)-NorEPI

HRP-(N-SMP)-NorEPI was selected as the ET for the direct ELISA according to the results obtained in the indirect competitive immunoassay, in which the most heterologous competitor conjugate BSA-(N-SMP)-NorEPI showed the best performance.

The ET was prepared in a two-step reaction, as shown in Figure 7.3-9. The first step consisted in the modification of the amino group of Lys residues with the linker N-SMP, forming amide bonds and introducing maleimide groups.[237] According to the structure of this enzyme, only two Lys residues are accessible enough to be derivatized. After the reaction, HRP-(N-SMP) conjugate was purified from the excess of linker by size exclusion chromatography on an ÄKTA prime system, eluting the sample through a Sephadex® G-25 column equilibrated with ultrapure H_2O. The introduction of the maleimide group on the enzyme allowed to conjugate the hapten of NorEPI, already synthesized and characterized in the Nb4D group. The second step consisted in the Michael addition of the nucleophilic functional group of the hapten (X) to the electrophilic double bond of the maleimide moiety on the enzymatic conjugate, leading to the formation of covalent bonds.

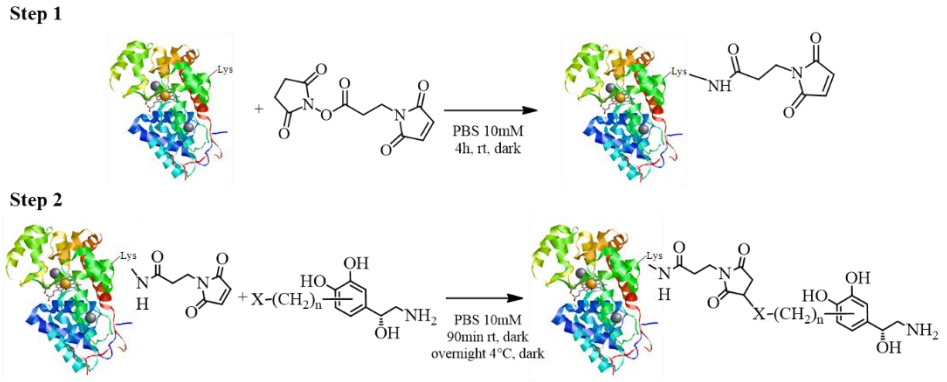

Figure 7.3-9: Reaction scheme for the preparation of HRP-(N-SMP)-NorEPI; activation of Lys residues with N-SMP (step 1) and Michael addition of the hapten of NorEPI (step 2).

After purification by dialysis with PBS and finally H_2O, the ET was characterized by MALDI-TOF-MS analysis to determine its hapten density. The comparison among the mass spectra, reported in Figure 7.3-10, of the starting reagent HRP (in blue), the intermediate conjugate HRP-(N-SMP) (in red) and the final product HRP-(N-SMP)-NorEPI (in green) confirmed the derivatization of the enzyme with the linker and the conjugation of the NorEPI hapten. The densities of linker and hapten were, respectively, 2 and 1.5 for each enzyme macromolecule.

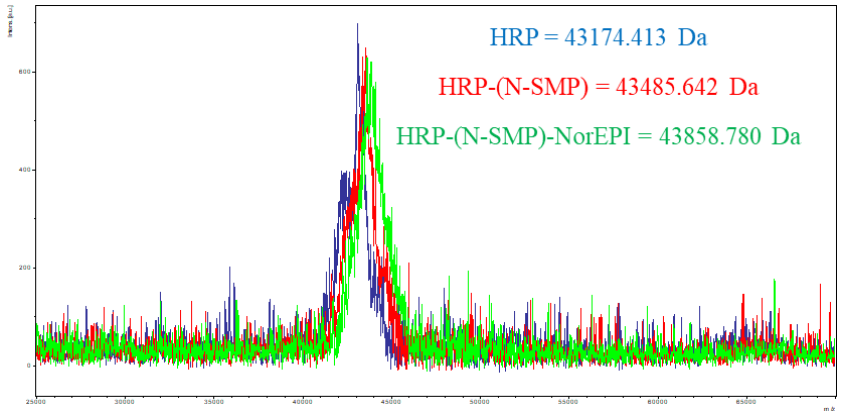

Figure 7.3-10: MALDI-TOF-MS analysis of HRP (in blue), HRP-(N-SMP) (in red) and HRP-(N-SMP)-NorEPI (in green) with the corresponding molecular weights.

7.3.2.2 Direct competitive ELISA

Once prepared the ET, 2D direct ELISA was performed both to assure the catalytic activity of HRP after conjugation process, and to optimize the As dilution and tracer concentration. The combination As334 1/12000 and HRP-(N-SMP)-NorEPI with a concentration of 8 ng/mL was selected for the competitive assay with EPI (0-50 µM).

In Figure 7.3-11 the competitive curve of the direct ELISA is compared to those obtained in the indirect formats while the experimental parameters of all these immunoassays are summarized in Table 7.3-3. The IC_{50} and LOD values and the working range of the direct ELISA were in the nanomolar range. The sensitivity

of this immunoassay, without optimization, was very similar to that of the indirect assay; however, the direct format could provide some advantages in terms of speed and simplicity of the immunochemical assay, being more attractive as diagnostic platform.

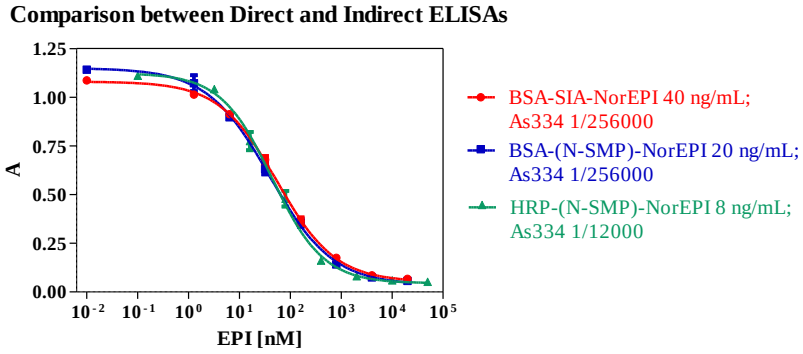

Figure 7.3-11: Comparison between the direct and indirect competitive ELISAs for the detection of epinephrine using As334. The direct competitive format was performed using HRP-(N-SMP)-NorEPI while the indirect ones using BSA-SIA-NorEPI and BSA-(N-SMP)-NorEPI.

Table 7.3-3: Comparison among the immunochemical features of the direct and indirect competitive ELISAs between epinephrine, As334 and HRP-(N-SMP)-NorEPI, BSA-SIA-NorEPI or BSA-(N-SMP)-NorEPI. IC_{50},A_{max}, A_{min}, R^2, LOD, hillslope and working range values are reported.

Experimental parameters	HRP-(N-SMP)-NorEPI	BSA-SIA-NorEPI	BSA-(N-SMP)-NorEPI
Ag or ET concentration [ng/mL]	8	40	20
As334 dilution	1/12000	1/256000	1/256000
A_{max}	1.10 ± 0.02	1.11 ± 0.04	1.07 ± 0.07
A_{min}	0.04 ± 0.01	0.05 ± 0.01	0.04 ± 0.01
Hillslope	-0.87 ± 0.04	-0.76 ± 0.03	-0.70 ± 0.05
R^2	0.994	0.998	0.996
IC_{50} [nM] **IC_{50} [µg/L]**	44 ± 1 8.1 ± 0.8	47 ± 6 8.6 ± 1.0	35 ± 5 6.3 ± 0.7
LOD [nM]	4.3 ± 1.3	2.1 ± 0.6	1.5 ± 0.3
WR [nM]	2-70	5-311	4-254

7.3.3 Synthesis and characterization of Ab-MNPs

Since the levels of EPI in biological fluids are in the picomolar range, as reported in the literature, the introduction of sample preconcentration could be very useful.[207] In this way, it could be possible to achieve a concentration of the analyte that might be measurable by direct or indirect immunochemical assays. The idea of preconcentrating the sample could be achieved by different methods, as explained in the introduction. In this context, one strategy might be using nanosystems able to recognize the analyte and then facilitate its separation from the mixture by a simple procedure.

For this purpose, MNPs-Ab could be a good solution, providing in one single platform the recognition element, the antibody, and the separating feature, the magnetic core. For this reason, Fe_3O_4@SiO_2 MNPs and Fe_3O_4@Cu@Au MNPs functionalized with the Ab - immunoglobulins G (IgGs) proteins - able to detect EPI were synthesized and characterized.

7.3.3.1 Antibody purification

The antiserum As334 was purified in order to obtain only the IgGs fraction for the functionalization of MNPs. The standard purification protocol for antibody consisted in few steps, as reported in the literature.[238,239] The pre-purification step by ammonium sulphate precipitation was used to separate immunoglobulins from other serum proteins, while the affinity chromatographic purification was needed to achieve purified IgGs in buffer solution, eluting the solution of immunoglobulins through a Protein A column. The elution of the IgGs solution through a desalting column provided the purified antibody, named Ab334, that was finally lyophilized and used for the functionalization of the nanosystems.

7.3.3.2 Functionalization of Fe_3O_4@SiO_2 MNPs

In order to immobilize the antibody Ab334 on the nanosystems, the preliminary activation of their surface with heterobifunctional molecules was performed.

The -OH groups present on silica shell of Fe_3O_4@SiO_2 MNPs were exploited for the reaction with the epoxy-silane 3-(glycidyloxypropyl)trimethoxy silane (GPTMS) that allowed the further conjugation of macromolecules, as shown in Figure 7.3-12. The -OH groups were first deprotonated by treating the Fe_3O_4@SiO_2 MNPs with 10% NaOH solution, increasing their nucleophilic power, and then used for the reaction with pure GPTMS (step 1). The MNPs-GPTMS were then washed with absolute EtOH to eliminate the excess of GPTMS and desiccated before the biofunctionalization. The surface activation with epoxy groups enabled the covalent binding of the antibody Ab334 on Fe_3O_4@SiO_2 MNPs (step 2); in fact, the nucleophilic residues of the protein, particularly Lys, can easily react with the epoxy groups ensuring the formation of covalent bonds between the antibody and the nanosystems. After the conjugation reaction, a capping step with ethanolamine was performed to deactivate all the unreacted epoxy groups. After washings with PBS, Fe_3O_4@SiO_2-Ab334 MNPs were stored at 4°C in the same buffer solution, characterized and then used for the immunochemical assays.

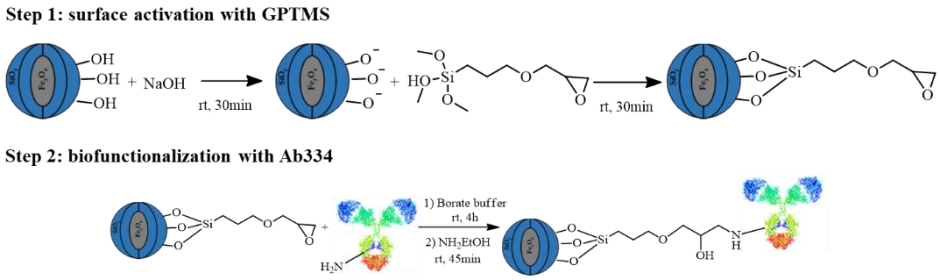

Figure 7.3-12: Reaction scheme of the functionalization of Fe_3O_4@SiO_2 MNPs with GPTMS (step 1) and then with the purified Ab334 (step 2).

7.3.3.3 Functionalization of Fe_3O_4@Cu@Au MNPs

To conjugate the antibody on Fe_3O_4@Cu@Au MNPs, a covalent approach involving heterobifunctional linkers was used instead of the easier but unstable protein absorption strategy.

Exploiting the chemical affinity between Au and thiol groups, already described in section 3.1.1.3, the surface of this kind of magnetic nanoparticles was first activated with a mixed SAM based on heterobifunctional thiol-PEG molecules, that were finally used for the conjugation of the Ab334, as shown in Figure 7.3-13.

A mixture of two kinds of linear PEG linkers, HS-PEG-COOH (average Mn=7500) and HS-PEG-OCH_3 (average Mn=6000) was used to achieve the mixed SAM. The presence of the thiol groups ensured the stable anchorage on Au surface, while the -COOH groups were exploited for the further conjugation of biomolecules through amide bonds. The use of two kinds of linkers instead of one, in a relative molar ratio HS-PEG-COOH : HS-PEG-OCH_3 of 1:3, decreased the negative charge density on the surface of nanoparticles, spacing them and promoting the biofunctionalization step. The anchorage of the linkers was performed under inert conditions in order to minimize the thiol-oxidation process, stirring the solution overnight at rt (step 1). Activated Fe_3O_4@Cu@Au-PEG MNPs were magnetically recovered, washed and then dried.

For the biofunctionalization with Ab334, the well-known carbodiimide chemistry was used; the -COOH groups were activated by an EDC/NHS solution and used for the reaction with Lys residues of the antibody, allowing its covalent binding through amide bonds formation (step 2). After the capping reaction with ethanolamine to deactivate all the unreacted reagents, the Fe_3O_4@Cu@Au-Ab334 MNPs were stored at 4°C in PBS.

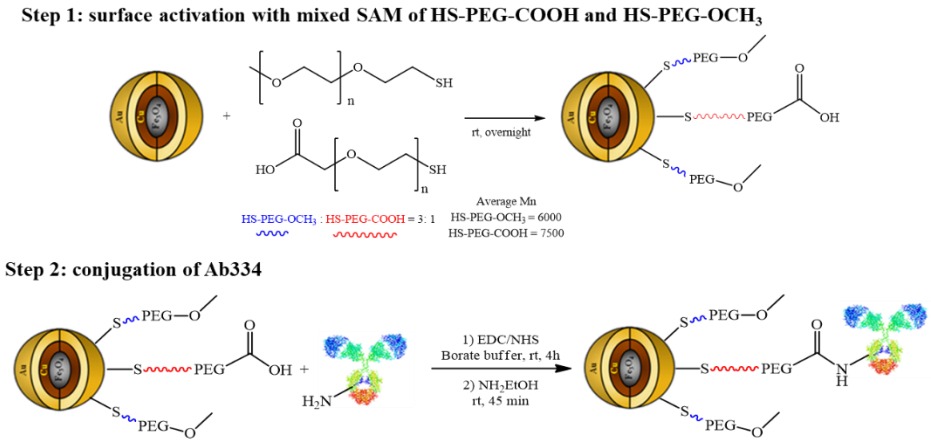

Figure 7.3-13: Reaction scheme of the activation of Fe_3O_4@Cu@Au MNPs with mixed-SAM made of SH-PEG-COOH and SH-PEG-OCH_3 (step 1) and their functionalization with Ab334 using EDC/NHS solution (step 2).

7.3.3.4 Characterization of the antibody-functionalized MNPs

The characterization of the two kinds of Ab334-MNPs was performed by different assays.

The presence of IgGs on nanosystems was confirmed by an immunochemical assay using anti-IgG-HRP, which was performed directly on Ab-MNPs known as magneto-ELISA format. The recognition process between IgG and anti-IgG led to the binding of the secondary antibody on nanoparticles. Consequently, the colorimetric signal, derived from the HRP-catalysed oxidation of the substrate solution, proved the binding of IgGs to the nanosystems.

The yields of the Ab conjugation reactions were determined by a quantitative Bradford protein assay.[240] This assay was performed on the supernatants and the washings of the reactions between Ab334 and the MNPs, using Ab334 serial dilutions for the calibration curve. When the molecule of Coomassie Brilliant blue G-250 interacts with a protein, in this case an Ab, the absorption band at λ=595 nm increases depending on protein concentration since it corresponds to the

protein-bound anionic form of the dye. As reported in Table 7.3-4, the conjugation of the Ab334 to nanosystems was successfully achieved, leading to reaction yields of 66.1% and 85.5% for Fe_3O_4@SiO_2-Ab334 MNPs and Fe_3O_4@Cu@Au-Ab334 MNPs, respectively.

Table 7.3-4: Experimental results of Bradford protein assays on the solutions (supernatant + washings) corresponding to Ab334-conjugation reactions. For each nanosystem the concentration of Ab334 in solution (μg/mL), the amount of Ab334 bound to MNPs - expressed as concentration (μg/mL) or referred to a mg of MNPs (μg/mg) - and the conjugation yield (%) are reported.

MNPs	Free Ab334 [μg/mL]	Bound Ab334 [μg/mL]	Bound Ab334 on MNPs mg [μg/mg]	Reaction yield [%]
Fe_3O_4@SiO_2-Ab334	169.32	330.69	8.55	66.1
Fe_3O_4@Cu@Au-Ab334	72.38	427.62	6.61	85.5

According to these experimental data, immunochemical magneto-assays based on MNPs-Ab-334 were developed in order to assess the recognition activity of the conjugated antibody towards EPI and to produce new and sensitive MNPs-based immunoassays.

7.3.4 Development of the direct competitive magneto-ELISA

Magneto-immunochemical assays were developed using the new synthesized and characterized Fe_3O_4@Cu@Au-Ab334 MNPs and Fe_3O_4@SiO_2-Ab334 MNPs. The ability of Ab334 to recognize and interact with the analyte or its competitors could have been affected by the conjugation process; structural modification of the antibody, in fact, could have been occurred during the reaction with nanoparticles. For these reasons, preliminary 2D direct magneto-ELISA assays were carried out in order to confirm the recognition ability of the Ab and to select

the optimal combination of MNPs/ET for the further competitive assay. The 2D magneto-ELISA assays were performed varying the quantity of Ab-334 functionalized magnetic nanoparticles, from 0 to 50 μg/well, and the concentration of HRP-(N-SMP)-NorEPI from 0 to 0.2 μg/mL. All the magneto-ELISA experiments were carried out following the protocol of the direct ELISA format; however, after each step of the assay the MNPs were magnetically separated from the solution, placing the plate on a magnetic rack, and manually washed. After the stopping reaction, the supernatants were moved to another plate and the colorimetric signal was measured at λ=450 nm, excluding the MNPs to avoid possible interferences.

The experimental evidences confirmed the activity of the Ab334 in detecting the ET, disproving the possible modification of the Ab due to the conjugation to MNPs. These assays allowed also the selection of the optimal combinations of MNPs quantity and ET concentration for the competitive assays, corresponding to 25 μg/well for Fe_3O_4@Cu@Au-Ab334 MNPs, 6 μg/well for Fe_3O_4@SiO_2-Ab334 MNPs and 60 ng/mL for HRP-(N-SMP)-NorEPI.

According to the inhibition curves obtained in the competitive assays, shown in Figure 7.3-14, EPI was able to compete with the enzymatic tracer for the binding site of Ab334 anchored to the surface of the nanosystems. As reported in Table 7.3-5, the detectability of the magnetic-immunoassays was comparable to that obtained using classic direct ELISA assays, especially in the case of Fe_3O_4@Cu@Au-Ab334 MNPs. The IC_{50} and LOD values, in fact, were in the nanomolar range.

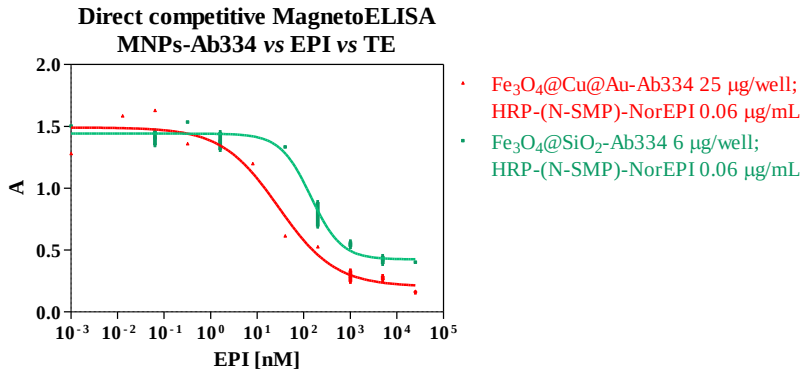

Figure 7.3-14: Inhibition curves obtained in the competitive magneto-ELISAs among Fe_3O_4@Cu@Au-Ab334 or Fe_3O_4@SiO_2-Ab334, epinephrine and HRP-(N-SMP)-NorEPI.

Table 7.3-5: Analytical parameters of the competitive direct magneto-ELISAs. Absorbance (minimum and maximum values), hillslope, R^2 and immunoassay features such as IC_{50}, LOD and WR are reported for Fe_3O_4@Cu@Au-Ab334/HRP-(N-SMP-NorEPI) and Fe_3O_4@SiO_2-Ab334/HRP-(N-SMP)-NorEPI combinations.

	Fe_3O_4@Cu@Au-Ab334 HRP-(N-SMP)-NorEPI	**Fe_3O_4@SiO_2-Ab334 HRP-(N-SMP)-NorEPI**
MNPs amount (µg/well)	25	6
ET concentration (ng/mL)	60	60
A_{min}	0.21 ± 0.07	0.42 ± 0.04
A_{max}	1.49 ± 0.06	1.44 ± 0.03
Hillslope	-0.71 ± 0.18	-1.33 ± 0.36
R^2	0.969	0.977
IC_{50} (nM) **IC_{50} (µg/L)**	45.9 ± 1.5 8.4 ± 0.3	253.9 ± 1.2 46.5 ± 0.3
LOD (nM)	0.04	14.8
WR (nM)	4-404	68-797

The poor reproducibility of the assays derived from the intrinsic variability of the experiments limited the applicability of the magneto-ELISA immunoassays. However, starting from the encouraging experimental data achieved in those assays, the simplest and reliable electrochemical readout for the implementation of the magneto immunoassays was addressed.

7.3.5 Development of the electrochemical magneto-immunosensors

Ab334-MNPs were used for the development of amperometric magneto-immunosensors, as proofs of concept of diagnostics methods for the detection of EPI.

As described previously in 7.1.2.1, MNPs could bring many advantages in electrochemical immunosensors; for instance, they could be easily manipulated, improving the washings and separation steps, and allow the possibility of renewing the surface of the electrode and shortening the time of the immunochemical assay. Moreover, the main advantage could derive from the possibility of using the Ab-MNPs for the recognition event of the analyte directly in the complex matrix, limiting the interferences due to different electroactive compounds present in the sample.

For the development of the electrochemical magneto-immunosensors, 1D immunoassays were first performed for the evaluation of the best combination of MNPs amount and ET concentration; starting from the results obtained in magneto-ELISA formats, a constant amount of MNPs was treated with serial dilutions of HRP-(N-SMP)-NorEPI. In detail, 30 μg/sample of Fe_3O_4@SiO_2-Ab334 MNPs and 125 μg/sample of Fe_3O_4@Cu@Au-Ab334 MNPs were stirred with enzymatic tracer solutions with concentrations ranging from 0 to 2 μg/mL. After the recognition step, MNPs were washed and then deposited on a screen-printed carbon electrode (SPCE) for the electrochemical detection. The negative current was measured separately for each sample after the addition of the substrate solution. As shown in the scheme of the electrochemical cell, reported in Figure 7.3-15, applying the constant potential of -0.1 V, the substrate TMB oxidized by the HRP of the enzymatic tracer, was reduced; so, the experimental reduction

current was directly proportional to the concentration of HRP-(N-SMP)-NorEPI in the sample.

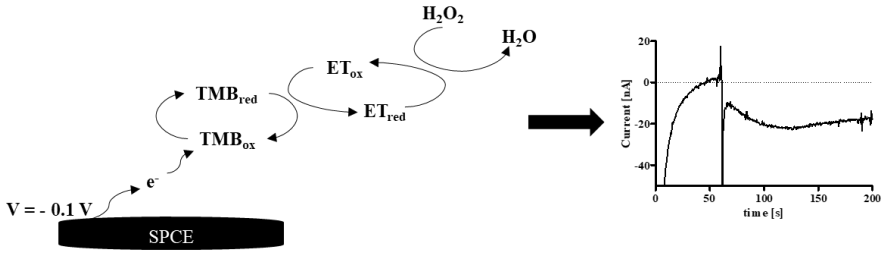

Figure 7.3-15: Scheme of the electrochemical cell for the magneto-immunoassays using Ab334 functionalized MNPs. Applying the constant V of -0.1 V to the SPCE containing the sample of Ab-MNPs, the negative current derived from the reduction of the HRP-oxidized TMB was measured.

From these electrochemical assays, the optimum concentrations of ET were selected, corresponding to 500 ng/mL and 250 ng/mL in combination with Fe_3O_4@SiO_2-Ab334 MNPs and Fe_3O_4@Cu@Au-Ab334 MNPs, respectively; the final reduction currents were around -300 nA after 30 min of immunochemical reaction performed in absence of analyte.

The competitive assays were carried out vigorously stirring standard solutions of EPI (0-50 μM) mixed with Ab-functionalized nanoparticles and ET solution. After magnetic separation and washings, the amperometric measurements of the concentration of the immunocomplexes MNPs/ET were performed in the electrochemical cell as previously described. The inhibitory effect of EPI was evident, according to the sigmoidal curves obtained from the electrochemical readout shown in Figure 7.3-16; the samples with high concentration of EPI, in fact, produced low reduction current.

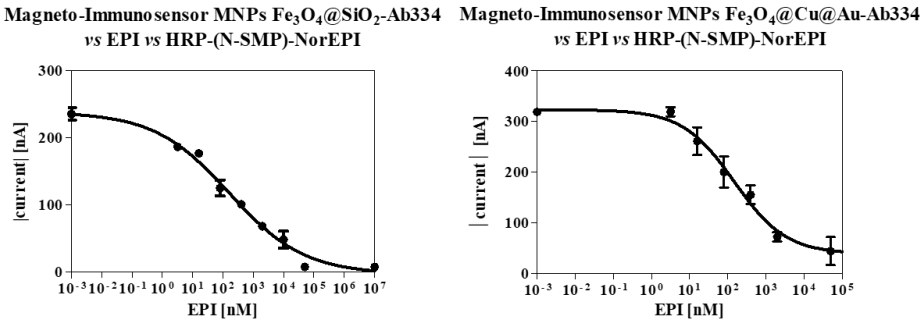

Figure 7.3-16: Inhibition curves achieved in direct competitive amperometric magneto-immunoassays among epinephrine, HRP-(N-SMP)-NorEPI and Fe_3O_4@SiO_2-Ab334 MNPs (left) or Fe_3O_4@Cu@Au-Ab334 MNPs (right).

Looking at the analytical parameters of these electrochemical immunoassays, summarized in Table 7.3-6, a slight but significant increment in the IC_{50} values was noted, comparing to the immunoassays performed without MNPs. However, despite the slight worsening of sensitivity of these assays, the use of MNPs could bring other advantages making the immunoassay quicker and easier to perform. Moreover, the optimization of some experimental parameters and the addition of a pre-incubation step might improve the sensitivity of this method.

According to these preliminary results, the electrochemical magneto-immunosensors based on Fe_3O_4@SiO_2-Ab334 or Fe_3O_4@Cu@Au-Ab334 nanosystems could be considered as promising diagnostics tools for the quantitative determination of EPI in biological samples.

Table 7.3-6: Analytical features of direct competitive amperometric magneto-immunoassays. The amount of Fe_3O_4@SiO_2-Ab334 MNPs or Fe_3O_4@Cu@Au-Ab334 MNPs, HRP-(N-SMP)-NorEPI concentration, minimum and maximum values of amperometric signals, hillslope, IC_{50}, LOD and WR values are reported in this table.

	Fe_3O_4@SiO_2-Ab334	**Fe_3O_4@Cu@Au-Ab334**
MNPs amount (µg/sample)	30	125
HRP-(N-SMP)-NorEPI concentration (ng/mL)	500	250
Current $_{bottom}$ (nA)	-3.1 ± 13.1	38.8 ± 18.0
Current $_{top}$ (nA)	238.2 ± 9.7	323.7 ± 17.7
Hillslope	-0.35 ± 0.05	-0.64 ± 0.15
R^2	0.979	0.924
IC_{50} (nM) **IC_{50} (µg/L)**	162.3 ± 1.6 29.7 ± 0.3	149.5 ± 1.5 27.4 ± 0.3
LOD (nM)	0.6	19.5
WR (nM)	4-5011	72-6310

7.4 CHAPTER CONTRIBUTIONS

- New immunochemical assays for the detection of EPI were developed. Indirect competitive ELISA assays demonstrated high sensitivity in the detection of the analyte achieving IC_{50} values in the nanomolar range (6-9 μg/L), using As334 as antiserum and BSA-(N-SMP)-NorEPI or BSA-SIA-NorEPI as competitors. Comparable analytical parameters were obtained by the direct competitive ELISA format using the enzymatic tracer HRP-(N-SMP)-NorEPI (IC_{50} 9-10 μg/L).
- New MNPs-Ab based on Fe_3O_4@SiO_2-Ab334 MNPs and Fe_3O_4@Cu@Au-Ab334 MNPs were synthesized and characterized. Different immunochemical assays were developed using these nanosystems, such as magneto-ELISAs and electrochemical magneto-immunosensors, achieving good sensitivity and low detectability limits (IC_{50} 27-30 μg/L), especially in the amperometric immunochemical assays. These nanosystems might be used both for the recognition and binding process of the analyte, due to the immobilized specific antibody, and for its separation and concentration from complex matrices, thanks to the properties of MNPs. The amperometric magneto-immunosensors might be considered promising diagnostics tools for the detection of EPI.

7.4.1 Future perspectives

- Optimize the experimental procedures of the amperometric magneto-immunosensor assays including, for instance, a pre-incubation step between MNPs and EPI.
- Evaluate the matrix effects of plasma and urine samples in the immunochemical assays and magneto-assays, and assess other analytical parameters (specificity, reproducibility and accuracy studies).

7.5 MATERIALS AND METHODS

Reagents, materials and equipment: The chemical reagents used were purchased by Sigma-Aldrich (Merck KGaA, Darmstadt, Germany). ÄKTA™ prime, provided with HiTrap™ Protein A HP column or HiTrap™ Desalting column (GE Helthcare, Uppsala, Sweden), was used for chromatographic purification with the corresponding software Prime View and Prime View Evaluation. OrDial D14 dialysis membranes (molecular weight cut off 12000-14000 Da) were purchased from Orange Scientific (Braine-l'Alleud, Belgium). The matrix-assisted laser desorption ionization time-of-flight mass spectrometer (MALDI-TOF-MS) was a Bruker autoflex III Smartbeam spectrometer (Billerica, Massachusetts). The pH and the conductivity of all buffers and solutions were measured with a pH-meter pH 540 GLP and a conductimeter LF 340, respectively (WTW, Weilheim, Germany). Polystyrene microtiter plates were purchased from Nunc (Maxisorp, Roskilde, Denmark). Dilution plates were purchased from Nirco (Barberà del Vallés, Spain). Washing steps of the immunochemical assays were performed on a Biotek ELx465 (Biotek Inc.). 96-well plate magnetic separation rack (CORTEX Biochem, WI, USA) was used for magnetic separation steps. Absorbances were read on a SpectramaxPlus (Molecular Devices, Sunnyvale, CA, USA) using the software SoftmaxPro v4.7 (Molecular Devices). Screen Printed Carbon Electrodes DRP-C110 (DropSens, Asturias, Spain) were connected to the potentiostat COMPACTSTAT.e Mobile Electrochemistry controlled by IviumSoft™ Electrochemistry Software (IVIUM Technologies, Eindhoven, The Netherlands). All the experimental data were analysed using the software GraphPad Prism 5.03 (GraphPad Software Inc., San Diego, CA, USA) and competitive curves were fitted with a four-parameters logistic equation.

Buffers: Unless otherwise indicated, phosphate buffer saline (PBS) is 0.01 M phosphate buffer in a 0.8% saline solution, pH 7.5. Coating buffer is a 0.05 M carbonate-bicarbonate buffer, pH 9.6. PBST is PBS with 0.05% Tween 20, pH

7.5. Citrate buffer is 0.04 M sodium citrate, pH 5.5. The substrate solution contains 0.01% 3,3',5,5'-tetramethylbenzidine (TMB) and 0.004% H_2O_2 in citrate buffer. Borate buffer is 0.2 M boric acid/sodium borate, pH 8.7.

Non-competitive indirect ELISA: The recognition and binding abilities of the antisera (As334-336) with the different antigens (BSA-SIA-EPI, BSA-(N-SMP)-EPI, BSA-SIA-NorEPI or BSA-(N-SMP)-NorEPI) were evaluated by two-dimensional titration assays. 2D-assays were carried out based on the measurement of the binding of serial dilutions of the antisera (1/1000 to 1/2048000, and zero) against different concentrations of the antigens (serial 1:2 dilutions of 1 μg/mL solution, and zero). The microtiter plate was coated with Ag dilutions in coating buffer (100 μL/well) and incubated overnight at 4°C. The next day, the plate was washed four times with PBST (300 μL/well) and the As dilutions were added to the wells (100 μL/well). After incubating 30 min at 25°C, the plate was washed again and a solution of anti-IgG-HRP (1/6000 in PBST) was added to the plate (100 μL/well). After 30 min incubating at rt, the plate was washed again and incubated in the dark after the addition of substrate solution (100 μL/well). The colorimetric reaction was stopped after 30 min at rt with 4 N H_2SO_4 (50 μL/well), and the absorbance was read at λ=450 nm. From these experiments, optimum concentrations for coating antigens and antisera dilutions were chosen to generate around 0.7-1 units of absorbance.

Competitive indirect ELISA: The microtiter plate was coated with the antigen, at the proper selected concentration in coating buffer (100 μL/well), and incubated overnight at 4 °C, covered with adhesive plate sealers. The next day, the plate was washed four times with PBST (300 μL/well), and the solutions of EPI (stock solution 10 mM in DMSO, serial dilutions from 50 μM to 0 nM in PBST) were added (50 μL/well), followed by the solution of antisera As334 (double concentration of the selected dilution in PBST, 50 μL/well). After 30 min at 25°C, the plate was washed four times with PBST (300 μL/well), and a solution of anti-IgG-HRP (1/6000 in PBST) was added to the plate (100 μL/well) and incubated

for 30 min at rt. The plate was washed again and then incubated in dark after the addition of the substrate solution (100 μL/well). The colorimetric reaction was stopped after 30 min at rt with 4 N H_2SO_4 (50 μL/well), and the absorbance was read at λ=450 nm. The standard curves were fitted to a four-parameter equation according to the following formula: $y = (A - B/[1 - (x/C)^D] + B$, where A is the maximal absorbance, B is the minimum absorbance, C is the concentration producing 50% of the maximal absorbance, and D is the slope at the inflection point of the sigmoid curve. Unless otherwise indicated, all the data presented for the immunochemical assays correspond to the average of at least three wells replicates.

Physicochemical parameters optimization: Different physicochemical parameters were assessed in the indirect competitive ELISA assays; the study included the variation of pre-incubation time (overnight – 0 min), competition time (60 – 0 min), Tween 20 concentration (0.1% - 0%), conductivity (96 – 2 mS/cm) and pH (11.5 – 2.5).

HRP-(N-SMP)-NorEPI synthesis: HRP was dissolved in PBS 10 mM pH=7.5 (5.04 mg in 474 μL) and N-SMP (0.65 mg in 30 μL DMF), ten-fold Lys equivalents, was added to the enzymatic solution, achieving a solution at 10 mg/mL in HRP. The reaction mixture was stirred for 4 h at rt in dark and then purified by ÄKTA™ chromatographic system eluting the solution through desalting columns by Milli-Q H_2O. The intermediate product HRP-(N-SMP) was mixed with NorEPI hapten (10 eq in DMF) and the reaction was performed in PBS 10 mM stirring in dark for 90 min at rt and then overnight at 4°C. The protein conjugate was purified by dialysis against 0.5 mM PBS (4×5 L) and Milli-Q H_2O (1×5 L) and was stored at 4°C. Working aliquots were prepared in 0.01 M PBS at 1 mg/mL and stored at 4 °C.

Hapten and linker densities of the bioconjugates were estimated by measuring the MW of the native protein and of the conjugates by MALDI-TOF-MS. BSA was

utilized as internal standard for calibrating the instrument, using the mixture HRP:BSA = 4:1 (40 µL HRP 10 mg/mL+10 µL BSA 10 mg/mL in H_2O) as the reference protein sample. Each mass spectrum was obtained by crystallization of the matrix (sinapinic acid, 2 µL of 10 mg/mL in a 70:30 solution of ACN / H_2O and 0.1% in HCOOH), followed by the addition of 2 µL of sample or 2 µL of the reference protein sample (diluted 1:2 with 0 ACN + 0.2% HCOOH). Finally, after evaporation of the solution deposited on the plate, 2 µL of the matrix were added again. The hapten densities (δ hapten) were calculated according to the following equation: $[MW_{conjugate}\text{-}MW_{HRP}]/MW_{hapten\ or\ linker}$.

2D Direct ELISA: The microtiter plate was coated with As334 dilutions in coating buffer (1/1000 to 1/1024000, and zero, 100 µL/well) and incubated overnight at 4°C. The following day, the plate was washed four times with PBST (300 µL/well), and serial 1:2 dilutions of HRP-(N-SMP)-NorEPI in PBST (starting solution 1 µg/mL in PBST, and zero) were added to the wells (100 µL/well). After stirring 30 min at rt in dark, the plate was washed again, and the substrate solution was added (100 µL/well). After stirring 30 min at rt in dark, the colorimetric reaction was stopped adding 4 N H_2SO_4 (50 µL/well), and the absorbance was read at λ=450 nm. From these experiments, optimum As334 dilution and enzymatic tracer concentration were chosen to generate around 0.7-1 units of absorbance.

Competitive direct ELISA: The microtiter plate was coated with As334 dilutions (1/12000 and 1/16000) in coating buffer (100 µL/well), incubated overnight at 4 °C. The next day, the plate was washed four times with PBST (300 µL/well), and the solutions of EPI (stock solution at 10 mM in DMSO, serial 1:5 dilutions from 50 µM to 0 nM in PBST) were added (50 µL/well), followed by the solution of HRP-(N-SMP)-NorEPI in PBST (32 and 16 ng/mL; 50 µL/well). After stirring 30 min at rt in dark, the plate was washed four times with PBST (300 µL/well) and the substrate solution was added (100 µL/well). The colorimetric reaction was stopped with 4 N H_2SO_4 (50 µL/well) after stirring 30 min at rt in dark, and the

absorbance was read at λ=450 nm. The inhibition curves were fitted as previously described.

As334 purification: A saturated solution of $(NH_4)_2SO_4$ was slowly added (50 μL each time) to three eppendorf containing 500 μL of As334 under stirring at 4°C, until reaching 45% of saturation. After stirring 4 h at 4°C, the solutions were centrifuged (10 min at 14000 rpm) and, once removed the supernatants, white precipitates were obtained. After solubilization with PBS 10 mM (300 μL/ sample), sample solutions were filtered on 0,2 μm filters and then purified by AKTA™, provided with Protein A column, eluting the solution with binding buffer (PBS 20 mM pH 7) and then with citrate buffer (0.1 M pH 4). The IgGs fraction of Ab334 was eluted with Milli-Q H_2O through the desalting column and finally lyophilized.

Synthesis of Fe_3O_4@SiO_2-Ab334 MNPs: 100 mg of Fe_3O_4@SiO_2 were stirred 30 min at rt with 2.4 mL of NaOH 10%. After washing with MilliQ H_2O (x3) and 60% EtOH (x3), 1.2 mL of pure GPTMS was added to the MNPs. After stirring 30 min at rt, the Fe_3O_4@SiO_2-GPTMS MNPs were washed three times with absolute EtOH and finally dried under vacuum.

1 mL of a stock solution of purified Ab334 (1 mg/mL in borate buffer 0.1 M pH 8.5) was added to 50 mg of Fe_3O_4@SiO_2-GPTMS MNPs dispersed in 1 mL of the same buffer solution and the reaction mixture was stirred 4 h at rt. Fe_3O_4@SiO_2-Ab334 were washed three times with the same buffer solution and then stirred with 1 mL of ethanolamine solution (0.1 M in PBS 10 mM). After 45 min, the Fe_3O_4@SiO_2-Ab334 MNPs were washed with PBS 10 mM and stored at 4°C in the same buffer at a concentration of 50 mg/mL.

Synthesis of Fe_3O_4@Cu@Au-Ab334 MNPs: 4 mL of an aqueous solution containing a mixture of HS-PEG-OCH_3 15 mM (2 mL, average M_n 6000, linear) and HS-PEG-COOH 5 mM (2 mL, average M_n 7500, linear) were added to 100 mg of Fe_3O_4@Cu@Au MNPs in 96 mL H_2O under N_2 flux. The solution was

divided in ten fractions that were stirred overnight at rt. The PEG-activated nanoparticles were magnetically collected, washed several times with MilliQ H_2O and dried.

50 mg of Fe_3O_4@Cu@Au-PEG MNPs were dispersed in 1 mL of EDC/NHS solution in 0.1 M borate buffer pH 8.5 (500 μL EDC 0.5 M + 500 μL NHS 0.4 M). After adding 1 mL of Ab334 stock solution (at 1 mg/mL in borate buffer), the mixture was stirred 4 h at rt. The Fe_3O_4@Cu@Au-Ab334 MNPs were magnetically collected, washed with the same buffer solution (1mL, x3) and dispersed in 1 mL of ethanolamine solution (0.1 M in PBS 10 mM). After 45 min of capping step, MNPs were washed three times with PBS 10 mM and then stored at 4°C in the same buffer at a concentration of 50 mg/mL.

Bradford protein assay: Serial 1:2 dilutions of Ab334 80 μg/mL in borate buffer were used for the calibration curve (160 μL/well) . The supernatants of the MNPs-functionalization reactions were diluted in borate buffer to obtain a theoretical concentration of 40 μg/mL (160 μL/well) while the washings solutions were used without further dilutions (160 μL/well). Adding 40 μL/well of Coomassie Brilliant Blue solution, the UV-Vis analysis was performed after 10 min measuring the absorbance at λ=595 nm. Comparing the A values of the samples to the calibration curve, the quantification of the free Ab334 and consequently of MNPs-bound Ab334 was performed.

Magneto-ELISA between MNPs and anti-IgG: MNPs-Ab334 dispersions in PBST, after 2 min sonicating, were added to the assay plate at serial 1:2 dilutions ranging from 50 μg/well to zero (100 μL/well). After magnetically separating the MNPs using the magnetic plate rack and removing the supernatants, 1/6000 dilution of anti-IgG-HRP in PBST was added (100uL/well). The plate was stirred 30 min at rt, MNPs were magnetically separated and three washings with PBST were performed. 100 μL/well of substrate solution were added to the plate and, after 30 min stirring at rt in dark, the colorimetric reaction was stopped adding 4

N H_2SO_4 (50 μL/well). MNPs were separated and the absorbance was read at λ=450 nm after moving the supernatants to a different dilution plate.

Direct magneto-ELISA: MNPs-Ab334 dispersions in PBST, after 2 min sonicating, were added to the assay plate at 1:2 serial dilutions ranging from 50 μg/well to zero (50 μL/well). 50 μL/well of HRP-(N-SMP)-NorEPI serial dilutions in PBST (from 0.4 μg/mL to zero) were added to the plate. After 30 min stirring at rt in dark, MNPs were magnetically collected using the magnetic plate rack and the assay plate was washed three times with PBST (100 μL/well). The substrate addition and the stopping reaction steps were performed as described in the previous protocol.

Direct competitive magneto-ELISA: Fe_3O_4@Cu@Au-Ab334 MNPs in PBST, after 2 min sonicating, were added to the assay plate at 25 μg/well (50 μL/well) while Fe_3O_4@SiO_2-Ab334 at 6 μg/well. 25 μL/well of EPI dilutions in PBST (from 50 μM to 0) and 25 μL/well of HRP-(N-SMP)-NorEPI 60 ng/mL in PBST were added to the plate. After 30 min stirring at rt in dark, MNPs were magnetically separated using the magnetic plate rack and the plate was washed three times with PBST (100 μL/well). The substrate addition and the stopping reaction steps were performed as previously described.

Amperometric magneto immunosensor direct assay: 125 μg/sample of Fe_3O_4@Cu@Au-Ab334 MNPs or 30 μg/sample of Fe_3O_4@SiO_2-Ab334 MNPs (100 μL/sample in PBST) were mixed with 1:2 serial dilutions of HRP-(N-SMP)-NorEPI (from 2 μg/mL in PBST to zero, 100 μL/sample) in eppendorf tubes. After 30 min stirring in dark at rt, MNPs were magnetically separated and washings with PBST were performed (3x100μL/sample). MNPs were dispersed in 160 μL of citrate buffer and 40 μL were put on the SPCE, holding them applying an external magnet, and used for each amperometric measurement. V=-0.1V was applied and, at t = 60 s, 10 μL of the substrate solution were added to the sample.

Current values measured at t=200 s, after resting the corresponding values at t=50 s, were plotted in front of [ET].

Amperometric magneto immunosensor direct competitive assay: 125 μg/sample of Fe_3O_4@Cu@Au-Ab334 MNPs (100 μL/sample in PBST) and 0.5 μg/mL of HRP-(N-SMP)-NorEPI (50 μL/sample in PBST) or 30 μg/sample of Fe_3O_4@SiO_2-Ab334 MNPs (100 μL/sample in PBST) and 1 μg/mL of HRP-(N-SMP)-NorEPI (50 μL/sample in PBST) were mixed in eppendorf tubes with 50 μL/sample of EPI serial dilutions in PBST (from 50 μM to zero). After 30 min stirring in dark at rt, MNPs were magnetically separated and washings with PBST were performed (3x100 μL/sample). The substrate addition and the amperometric detection were performed as previously described. Current values measured at t=200 s, after resting the corresponding values at t=50 s, were plotted in front of [EPI].

8. ANNEX: NANOPARTICLES-MEDIATED OXIDATION OF EPI

8.1 INTRODUCTION

This annex deals with the proposal of using Fe_3O_4-based nanosystems as multifunctional nanoplatforms for the detection of EPI exploiting its MNPs-mediated oxidation process. This research work was carried out in the Nb4D group.

8.1.1 Oxidation mechanism of EPI

The oxidation mechanism of EPI consists in two redox reactions separated by an intermediate cyclization reaction, as reported in Figure 8.1-1.[213] The catechol moiety of EPI is oxidised into the corresponding orto-quinone compound. Then, an 1,4 Michael addition can occur, depending on the pH, transforming adrenaline o-quinone into leucoadrenochrome; at pH > 3, in fact, the secondary amine group is partially deprotonated, reacting as nucleophile group by an intramolecular cyclization and producing the stable corresponding five-membered ring. Leucoadrenochrome can therefore undergo to another oxidation of the catechol group, producing adrenochrome which can carry out a polymerization process, producing melanin molecules.[212,241]

This mechanism can be catalyzed in the same way by using electrochemical techniques, oxidoreductase enzymes like HRP, and also some kinds of nanomaterials, such as SiO_2 NPs.[242,243]

Since the oxidation products show characteristic absorption bands, especially the red-colored final compound adrenochrome (λ_{max}=490 nm), the UV-Vis spectroscopy can be used for monitoring this oxidation pathway.[244]

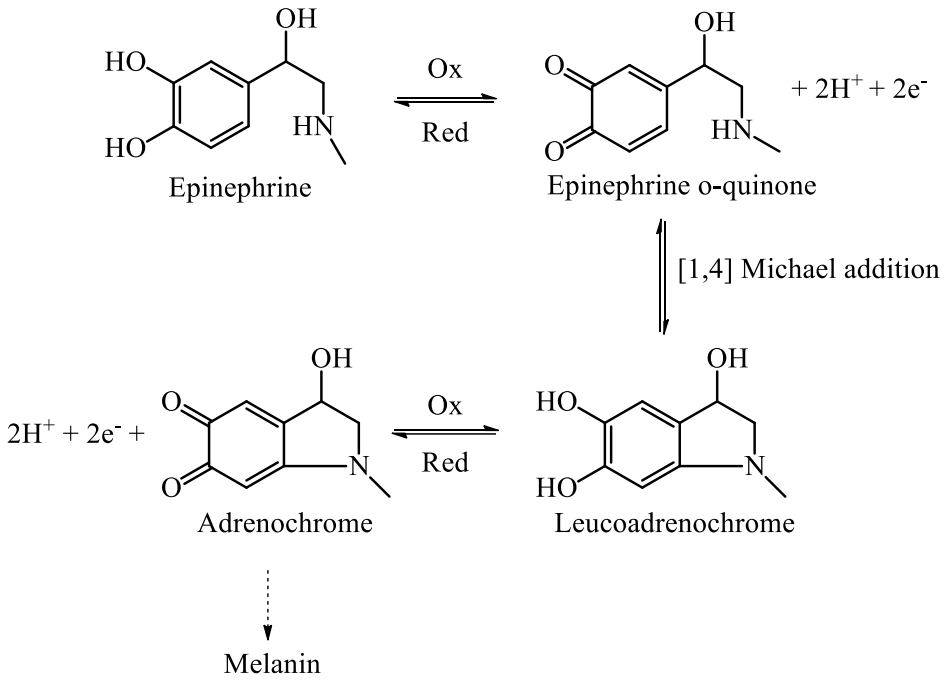

Figure 8.1-1: Oxidation pathway of epinephrine. The oxidation of the catechol moiety produces adrenaline o-quinone, that can undergo to an 1,4 Michael addition leading to leucoadrenochrome. Another oxidation produces adrenochrome which can polymerize into melanin molecules.

8.2 CHAPTER OBJECTIVES

The combination of the well-known catalytic properties of MNPs with their surface functionalization with Ab able to recognize EPI might pave the way for the development of powerful multimodal diagnostic tools.

For these reasons, the idea behind this annex is using MNPs-Ab for the recognition, separation and measurement of EPI using analytical techniques. The Fe_3O_4@Cu@Au-Ab334 MNPs and Fe_3O_4@SiO_2-Ab334 MNPs might be very promising nanosystems for this purpose; in fact, they combine the antibody able to detect EPI, as demonstrated in the previous chapter, with the superparamagnetic

core sensitive to the application of an external magnetic field. However, their oxidative power towards EPI should already be demonstrated.

The aim of this annex, as shown in Figure 8.2-1, is to evaluate the ability of Fe_3O_4@Cu@Au MNPs and Fe_3O_4@SiO_2 MNPs, functionalized with the anti-EPI Ab334 to oxidize adrenaline to adrenochrome, performing also a comparative study with MNPs functionalized with the Ab186, a pre-immune not specific antibody. In this way it might be possible to demonstrate, as proof of concept, the powerful potential applicability of MNPs-Ab334 as multitasking diagnostic tools for the recognition, separation and quantification of EPI.

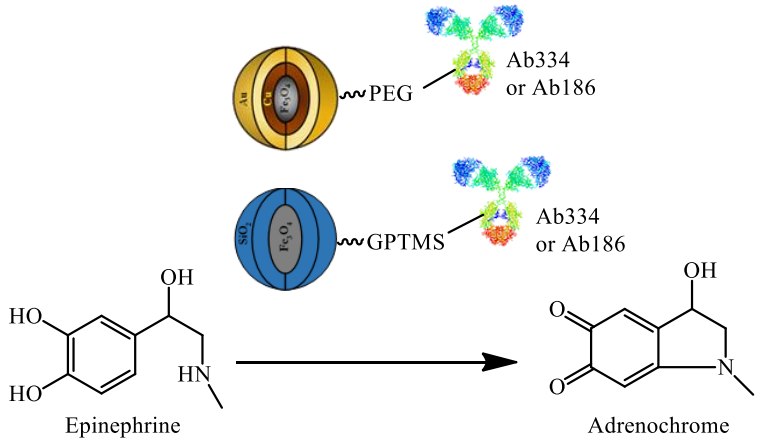

Figure 8.2-1: Scheme of the aim of the annex: a study of the oxidative ability of Fe_3O_4@Cu@Au and Fe_3O_4@SiO_2 nanosystems, functionalized with Ab334 (anti-EPI Ab) towards epinephrine, compared to other nanosystems functionalized with Ab186 (not specific Ab).

8.3 RESULTS AND DISCUSSION

In this section the experimental results concerning the study of the oxidative ability of Fe_3O_4@Cu@Au-PEG-Ab334 MNPs and Fe_3O_4@SiO_2-GPTMS-Ab334 MNPs towards EPI are presented. The evaluation of the selectivity of these nanosystems is also reported by a comparative study with the same nanoparticles functionalized with the pre-immune not specific antibody Ab186.

8.3.1 Evaluation of the oxidative ability of Ab334-MNPs

The study of the oxidative ability towards EPI of the MNPs-Ab334, previously synthesized and characterized as reported in chapter 7, was first assessed. Fe_3O_4@Cu@Au-Ab334 MNPs or Fe_3O_4@SiO_2-Ab334 MNPs were dispersed in EPI solutions in citrate buffer and H_2O_2 was added to trigger the oxidation reaction. The same samples of MNPs and EPI without adding H_2O_2 were used as negative controls, together with the blank of EPI and H_2O_2 without the MNPs. After stirring the samples for 20 min in dark, a significant and clearly visible increase in red colour was observed only in the solutions containing both MNPs and H_2O_2, as qualitatively shown in Figure 8.3-1. The same experiment was performed mixing MNPs with only H_2O_2, without achieving any colour variation in the samples. The change in the solutions from colourless to red was a strong proof that EPI (colourless) was oxidized to adrenochrome (red). These evidences were also an interesting signal of the key role of the MNPs as reaction promoters.

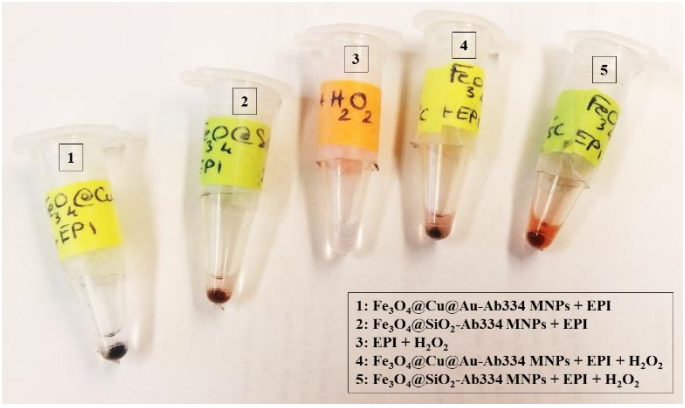

Figure 8.3-1: Qualitative proof of the MNPs-mediated oxidation of epinephrine (colorless) to adrenochrome (red). As reported in the legend, samples consisted in epinephrine solutions with or without nanosystems (Fe_3O_4@Cu@Au-Ab334 or Fe_3O_4@SiO_2-Ab334 MNPs) and H_2O_2 solution.

8.3.1.1 Kinetic evaluation

Since adrenochrome is the final product of the oxidation of EPI and is characterized by an absorption band in the visible region, kinetic studies by monitoring and measuring it were performed using UV-Vis spectroscopy to better understand the process. MNPs and EPI were stirred in the presence and in the absence of H_2O_2, recording UV-Vis spectra at times ranging from 0 min (before adding H_2O_2) to 360 min. Analysing the data reported in Figure 8.3-2, the increase of an absorption band corresponding to adrenochrome (λ_{max}=490nm) was evident only in the samples containing MNPs and H_2O_2, corresponding to green and blue lines. Any absorption band in the visible region was observed in the samples without H_2O_2 (red and orange lines) used as negative control neither in the EPI + H_2O_2 blank (purple line). In these experimental conditions – MNPs 1 mg, EPI 1 mM and H_2O_2 1% - the phenomenon was observed already after few minutes reacting and regardless of the kind of nanosystem used. The formation of the adrenochrome reached a maximum after 30 min stirring, according to the intensity of its corresponding absorption band, and then it probably reacted through polymerization mechanism to melanin since the solutions became colourless again

and the absorption band decreased. These experimental evidences validated the hypothesis of the MNPs-mediated oxidation of EPI, triggered by the formation of free radicals on the activated surface, which were able to oxidize the hydrogen donor substrate – here EPI.

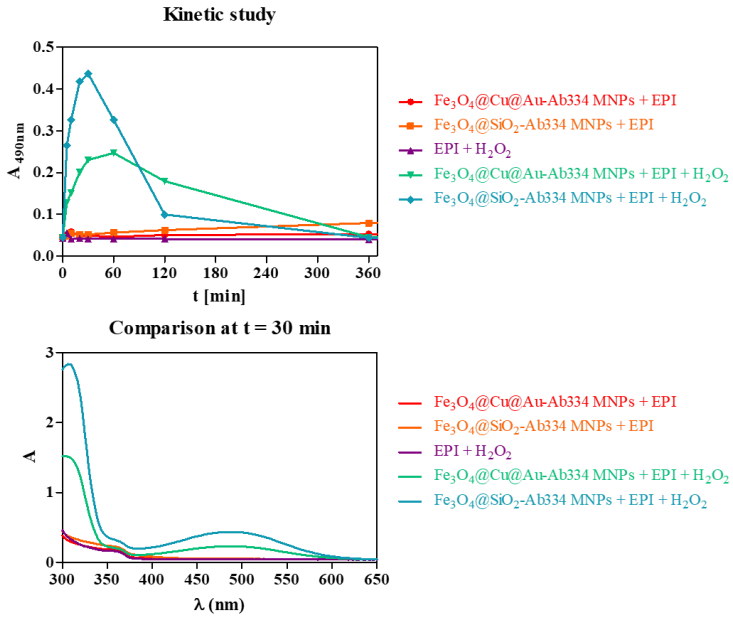

Figure 8.3-2: Top: UV-Vis kinetic study at λ=490 nm of the MNPs-mediated oxidation of epinephrine from 0 min to 360 min. Epinephrine solutions were stirred with Fe_3O_4@SiO_2 MNPs, in presence and in absence of H_2O_2 (blue and orange lines respectively) or with Fe_3O_4@Cu@Au-Ab334 MNPs in presence and in absence of H_2O_2 (green and red lines respectively). Purple line corresponds to negative control of EPI and H_2O_2. **Bottom**: Comparison among the same samples after 30 min reacting.

8.3.1.2 Changing of concentrations: MNPs, H_2O_2 and EPI

To achieve experimental evidences measurable by UV-Vis spectroscopy, high amounts of MNPs, H_2O_2 and EPI were used. First, the effects of changing the concentrations of each reagent was evaluated. MNPs concentration was assessed from 1 mg/sample to 1 μg/sample. The decrease in MNPs quantity from 1 mg/sample to 100 μg/sample led to a significant reduction of the maximum

intensity of the colorimetric signal, which was reached after long reaction time (40-60 min). Lower quantities of MNPs than 100 μg/sample did not produce measurable UV-Vis signals. H_2O_2 concentration was assessed from 3% to 0.01 %; the increase in H_2O_2 concentration from 1% to 3% had not a significant effect since it could be considered already in excess. Below 1%, the signal was not measurable. EPI solutions at a concentration ranging from 1 nM to 1 mM were analysed. The use of μM and nM EPI solutions produced an amount of adrenochrome too low for UV-Vis detection. For this reason, other analytical techniques, for instance electrochemical ones, should be probably used in order to detect samples with low concentrations of analyte (EPI < 1mM).

8.3.2 Evaluation of the selectivity of Ab334-MNPs

In order to evaluate the possibility to carry out a selective oxidative process, a pre-incubation step between MNPs and EPI was introduced. For this purpose, different kinds of MNPs-Ab were selected; MNPs loading Ab334 and MNPs functionalized with Ab186 were used. Fe_3O_4@Cu@Au-Ab186 MNPs and Fe_3O_4@SiO_2-Ab186 MNPs were synthesized in the same way as the corresponding MNPs-Ab334, as reported in 7.3.3, conjugating the purified pre-immune Ab186 already available in the Nb4D group. This antibody did not show specificity and for this reason it was selected, in opposition to the specific Ab334.

The four kinds of nanosystems at 1 mg/sample, Fe_3O_4@Cu@Au-Ab (334 or 186) MNPs and Fe_3O_4@SiO_2-Ab (334 or 186) MNPs were stirred with 1 mM EPI solution in citrate buffer for 15 min. This pre-incubation step was performed to promote the binding of EPI to the Ab-MNPs without triggering its oxidation. MNPs were then washed several times with citrate buffer to remove the unbound EPI and finally H_2O_2 1% solution was added to each sample. A solution containing only EPI and H_2O_2 was used as negative control. After 20 min stirring, the UV-

Vis spectra reported in Figure 8.3-3 were recorded. Analysing the experimental data, an increase in the absorption bands corresponding to EPI-oxidation products, especially adrenochrome (λ_{max}=490nm), was observed only in the samples containing MNPs functionalized with Ab334 (red and blue lines). Since the samples containing MNPs-Ab186 (green and purple lines) did not show any difference compared to the blank (EPI + H_2O_2; orange line), the oxidation of EPI was not occurred. Therefore, the UV-Vis absorption bands derived from the oxidation of the amount of EPI loaded to the MNPs only due to the specific recognition between Ab334 and the analyte, which took place during the pre-incubation step.

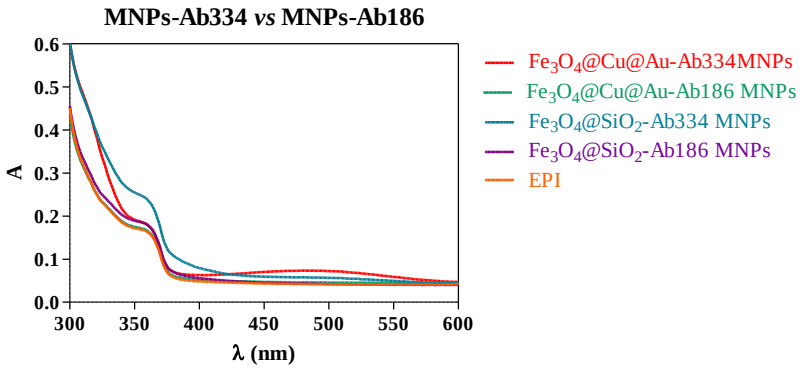

Figure 8.3-3: UV-Vis spectra concerning the selectivity experiment recorded after 20 min. Fe_3O_4@Cu@Au-Ab (334 or 186) and Fe_3O_4@SiO_2-Ab (334 or 186) were preincubated with epinephrine and, after magnetic separation and washings, H_2O_2 was added to the samples.

These experimental evidences can pave the way to the development of a diagnostic system for detecting EPI by a two-step procedure. The pre-incubation step between MNPs-Ab334 and the analyte into the sample ensures the specificity, promoting the recognition and binding events. The following addition of H_2O_2, after the magnetic separation of the nanosystems from the solution, triggers the oxidation process of the analyte, producing the signal measurable with sensitive analytical techniques.

8.4 CHAPTER CONTRIBUTIONS

- The nanosystems based on Fe_3O_4@Cu@Au and Fe_3O_4@SiO_2 MNPs were able to promote the oxidation of the catecholamine EPI mediated by H_2O_2,
- Using MNPs functionalized with a specific antibody raised against EPI, like Ab334, it was possible to achieve a selective method for binding, magnetically separating and detecting the analyte. Through a two-step procedure, consisting in a pre-incubation between MNPs-Ab334 and EPI followed by the addition of H_2O_2, the selective oxidation of EPI bound to MNPs-Ab334 could be achieved.

8.4.1 Future perspectives

- Study the MNPs-mediated oxidation of EPI using more sensitive analytical techniques, such as electrochemical ones, evaluating also the activity of bare MNPs. Optimize some physicochemical parameters such as the incubation time, buffer solution or concentration of MNPs.
- Validate the two-step procedure in standard complex solutions and biological matrices, such as plasma or urine.

8.5 MATERIALS AND METHODS

Reagents, materials and equipment: The chemical reagents used were purchased by Sigma-Aldrich (Merck KGaA, Darmstadt, Germany). The pre-immune antiserum As186 was already present in Nb4D group and ÄKTA™ prime, provided with HiTrap™ Protein A HP column or HiTrap™ Desalting column (GE Helthcare, Uppsala, Sweden), was used for its purification with the corresponding software Prime View and Prime View Evaluation. The pH and the conductivity of all buffers and solutions were measured with a pH-meter pH 540 GLP and a conductometer LF 340, respectively (WTW, Weilheim, Germany). UV-Vis spectra were recorded from 200 to 1000 nm by means of SpectramaxPlus (Molecular Devices, Sunnyvale, CA, USA) with the software SoftmaxPro v4.7 (Molecular Devices) using dilution plates as sample holders, purchased from Nirco (Barberà del Vallés, Spain). All the experimental data were analysed using the software GraphPad Prism 5.03 (GraphPad Software Inc., San Diego, USA).

Kinetic evaluation: two samples of Fe_3O_4@Cu@Au-Ab334 (1 mg/sample) and 2 samples of Fe_3O_4@SiO_2-Ab334 MNPs (1 mg/sample) were stirred at 25°C in Eppendorf tube with 1 mM EPI solution (180 µL/sample) in citrate buffer (0.04 M pH 5.5). UV-Vis spectra were recorded in a dilution plate before and after the addition of H_2O_2 10 % solution in citrate buffer (20 µL/sample) or only citrate buffer (20 µL/sample) from 5 min to 360 min. A solution of EPI 1 mM and H_2O_2 10 % without MNPs was used as blank.

Changing of concentrations: MNPs

90 µL/sample of EPI 1mM solution in citrate buffer were stirred with MNPs-Ab334 (Fe_3O_4@Cu@Au-Ab334 or Fe_3O_4@SiO_2-Ab334 MNPs) at concentrations of 1000, 100, 10 or 1 µg/sample. After adding 10 µL of H_2O_2 10 % in citrate buffer

UV-Vis spectra were recorded in a dilution plate at 20, 40 and 90 min. Samples of EPI/H_2O_2 and MNPs-Ab334/EPI/citrate buffer were used as blank.

Changing of concentrations: H_2O_2

90 µL/sample of EPI 1mM solution in citrate buffer were stirred with 100 µg/sample of MNPs-Ab334 (Fe_3O_4@Cu@Au-Ab334 or Fe_3O_4@SiO_2-Ab334 MNPs). After adding 10 µL of H_2O_2 solution in citrate buffer (at concentrations of 30%, 10%, 1% or 0.1%) UV-Vis spectra were recorded in a dilution plate after 20, 40 and 60 min. Samples of EPI/H_2O_2 30% and MNPs-Ab334/EPI/citrate buffer were used as blank.

Changing of concentrations: EPI

90 µL/sample of EPI solutions in citrate buffer, at concentrations ranging from 1 mM to 1 nM, were stirred with 100 µg/sample of MNPs-Ab334 (Fe_3O_4@Cu@Au-Ab334 or Fe_3O_4@SiO_2-Ab334 MNPs). After adding 10 µL of H_2O_2 10 % solution in citrate buffer, UV-Vis spectra were recorded in a dilution plate after 20 and 60 min. Samples of EPI 1 mM/ H_2O_2 10% and MNPs-Ab334/citrate buffer/H_2O_2 10% were used as blank.

Selectivity evaluation: 1 mg of Fe_3O_4@Cu@Au or Fe_3O_4@SiO_2 MNPs functionalized with Ab334 or Ab186 were stirred for 15 min with 100 µL/sample of EPI 0.9 mM in citrate buffer (0.04 M, pH 5.5). After magnetic separation, MNPs were washed twice with citrate buffer and then dispersed in H_2O_2 1% (100 µL/sample). A solution of EPI 1 mM (90 µL) and H_2O_2 10% (10µL), added after 15 min, was used as blank. After 20 min stirring, UV-Vis spectra of the samples were recorded in a dilution plate (100 µL sample/well).

9. CONCLUSIONS OF THIS THESIS

9.1 Conclusions

Among the superparamagnetic nanoparticles suitable for biomedical applications, new engineered nanosystems have been developed in this research work.

- Two basic core-shell structures made of Fe_3O_4@Cu@Au or Fe_3O_4@SiO_2 MNPs have been designed, synthesized and characterized by means of different physicochemical techniques, proving their nanometric size and core-shell structure.
- The surface activation exploiting the physicochemical features of the external inorganic shell, and the functionalization with polymers, proteins or bioactive molecules have been carried out according to the planned biomedical end use.
- The internalization of differently coated MNPs into monocyte-differentiated macrophages have been achieved, preferentially for the nanosystems loading Tf. These results, together with the possibility of further functionalization with drugs and combined with the ability of Tf in targeting cancer cells, make these nanosystems favourable for using in the Trojan Horse approach.
- The lipodepsipeptides SRE and SP22A have been loaded, for the first time, on nanoparticles without losing their biological activities. The confirmation of the *in vitro* antimicrobial activity on the yeast *R. pilimanae* and the uptake by monocyte-differentiated macrophages make the MNPs-SRE and MNPs-SP22A promising tools for a new-generation strategy for monitoring and treating infectious diseases.
- The development of the direct and indirect competitive ELISA immunoassays for the *in vitro* detection of EPI has been firstly addressed, reaching good sensitivity and detectability parameters. Amperometric magneto-immunosensors involving antibody-functionalized MNPs have been developed, avoiding analyte modification, reaching IC_{50} and LOD

values in the nanomolar range. These diagnostic platforms, including those based on the engineered nanosystems, could prove to be efficient and sensitive alternatives to the standard analytical methods used for detecting EPI in biological samples.

- The ability of antibody-functionalized MNPs to detect EPI and promote its H_2O_2-mediated oxidation have been demonstrated, opening the possibility to use them as diagnostic tools for the recognition, separation and analysis of EPI.

The scientific results achieved during this research work using the nanosystems based on Fe_3O_4@Cu@Au and Fe_3O_4@SiO_2 MNPs might contribute to know and develop new diagnostic tools and/or therapeutic strategies.

10. ACRONYMS AND ABBREVIATIONS

10.1 ACRONYMS AND ABBREVIATIONS

A	Absorbance
AA	Amino Acid
Ab	Antibody
Ab186	Antibody 186 after purification
Ab334	Antibody 334 after purification
ACN	Acetonitrile
AFM	Atomic Force Microscopy
Ag	Antigen
APTES	(3-AminoPropyl)TriethoxySilane
As	Antiserum
As334, As335, As336	Antiserum 334, 335, 336
Au NPs	Gold nanoparticles
BSA	Bovine Serum Albumin
CD	Circular dichroism
CSIC	Spanish National Research Council
CT	Computer Tomography
Da	Dalton
Dab	2,4-diaminobutyric acid
DCC	N,N'-dicyclohexylcarbodiimide
DHFR	DiHydroFolate Reductase
DMEM	Dulbecco's Modified Eagle's medium
DMF	N,N-dimethylformamide
DOSY	Diffusion Ordered SpectroscopY
EDC-HCl	1-Ethyl-3-(3-dimethylaminopropyl)carbodiimide hydrochloride
ELISA	Enzyme-Linked Immunosorbent Assay
EPI	(-)-EPInephrine
EPR	Enhanced Permeability and Retention Effect
ET	Enzymatic Tracer
FA	Folic Acid
FBS	Fetal Bovine Serum
FRs	Folate Receptors
FT-IR	Fourier-Transform Infrared Spectroscopy
GPTMS	(3-Glycidyloxypropyl)trimethoxysilane
H_c	Coercivity
HCH	Horseshoe Crab Hemocyanin
HRP	Horseradish Peroxidise
IC10	Concentration in which the signal is 90 % inhibited
IC20	Concentration in which the signal is 80 % inhibited
IC50	Concentration in which the signal is 50 % inhibited

IC80	Concentration in which the signal is 20 % inhibited
IC90	Concentration in which the signal is 10 % inhibited
IgG	Immunoglobulin G
IQAC	Institute of Advanced Chemistry of Catalonia
LA	Lipoic Acid
LOD	Limit Of Detection
LSPR	Localized Surface Plasmon Resonance
MALDI-TOF-MS	Matrix Assisted Laser Desorption Ionization - Time of Flight Mass Spectrometry
MIC	Minimum Inhibitory Concentration
MNPs	Magnetic NanoParticles
MNPs-Ab186	Fe_3O_4@Cu@Au-PEG-Ab186 or Fe_3O_4@SiO_2-GPTMS-Ab186
MNPs-Ab334	Fe_3O_4@Cu@Au-PEG-Ab334 or Fe_3O_4@SiO_2-GPTMS-Ab334
MNPs-APTES	Fe_3O_4@SiO_2-APTES MNPs
MNPs-GPTMS	Fe_3O_4@SiO_2-GPTMS
MNPs-LA-NHS	Fe_3O_4@Cu@Au-LA-NHS MNPs
MNPs-PEG	Fe_3O_4@Cu@Au-PEG
MNPs-PLA	Fe_3O_4@SiO_2-APTES-PLA MNPs
MNPs-PLA-SP22A-TR	Fe_3O_4@SiO_2-APTES-PLA-cadaverineTR-SP22A MNPs
MNPs-PLA-TR	Fe_3O_4@SiO_2-APTES-PLA-cadaverineTR MNPs
MNPs-PLL	Fe_3O_4@Cu@Au-LA-PLL
MNPs-PLL-FA	Fe_3O_4@Cu@Au-LA-PLL-FA
MNPs-PLL-MTX	Fe_3O_4@Cu@Au-LA-PLL-MTX
MNPs-PLL-TR	Fe_3O_4@Cu@Au-LA-PLL-TR MNPs
MNPs-SP22A	Fe_3O_4@SiO_2-APTES-PLA-SP22A MNPs
MNPs-SRE	Fe_3O_4@SiO_2-APTES-PLA-SRE MNPs
MNPs-Stv-TR	Fe_3O_4@Cu@Au-LA-Stv-TR
MNPs-Tf	Fe_3O_4@Cu@Au-LA-Tf
MNPs-Tf-TR	Fe_3O_4@Cu@Au-LA-Tf-TR
M_r	Remanence
MRI	Magnetic Resonance Imaging
M_{sat}	Saturation Magnetization
MTX	Methotrexate
MW	Molecular weight
Nb4D	Nanobiotechnology for Diagnostics Group
NHS	N-HydroxySuccinimide
NOESY	Nuclear Overhauser Effect Spectroscopy
NorEPI	(-)-NorEPIneprhine
NPs	Nanoparticles
N-SMP	N-succinimidyl 3-maleimidopropionate
P.s. pv. *syringae*	*Pseudomonas syringae* pv. *syringae*
PAb	Polyclonal Antibody

PABA	p-AminoBenzoic Acid
PBS	Phosphate Buffered Saline solution
PBST	Phosphate Buffered Saline Tween-20 solution
PEG	PolyEthylene Glycol
PEG-SH	Thiolated poly(ethylene)glycol
PET	Positron Emission Tomography
PhR	Phenol Red
PLA	Poly-L-Aspartic acid
PLA-TR	Poly-L-Aspartic acid-Texas Red cadaverine conjugate
PLL	Poly-L-Lysine
PLL-TR	Poly-L-Lysine-Texas Red conjugate
PMA	Phorbol 12-Myristate 13-Acetate
PVP	PolyVinylPyrrolidone
R. pilimanae	*Rhodotorula pilimanae*
RFC	Reduced Folate Carriers
RPMI	Roswell Park Memorial Institute medium
rt	Room temperature
SAM	Self-Assembled Monolayer
SIA	N-Succinimidyl IodoAcetate
SP22A	Syringopeptin 22A
SPCE	Screen Printed Carbon Electrode
SPION	SuperParamagnetic Iron Oxide Nanoparticles
SPs	Syringopeptins
SPR	Surface Plasmon Resonance
SRE	Syringomycin E
SRs	Syringomycins
Stv	Streptavidin
TEM	Transmission Electron Microscopy
TEOS	TetraEthyl Orthosilicate
Tf	Transferrin
TFA	Trifluoroacetic acid
TfRs	Transferrin Receptors
Tf-TR	Transferrin-Texas Red conjugate
THF	TetraHydroFolate
TMB	3,3',5,5'-TetraMethylBenzidine
TOCSY	TOtal Correlated SpectroscopY
TR	Texas Red
TSP	Trimethylsilyl propionate
V	Voltage
VSM	Vibrating Sample Magnetometer
XRPD	X-Ray Powder Diffraction
α-FR	α isoform of the Folate Receptor

11. BIBLIOGRAPHY

(1) H. Goesmann; C. Feldmann. Nanoparticulate functional materials. *Angewandte Chemie International Edition* **2010**, *49*, 1362-1395.
(2) L. Zhang; F.X. Gu; J.M. Chan; A.Z. Wang; R.S. Langer; O.C. Farokhzad. Nanoparticles in Medicine: Therapeutic Applications and Developments. *Clinical Pharmacology & Therapeutics* **2008**, *83*, 761-769.
(3) E.K. Lim; T. Kim; S. Paik; S. Haam; Y.M. Huh; K. Lee. Nanomaterials for Theranostics: Recent Advances and Future Challenges. *Chemical reviews* **2015**, *115*, 327-394.
(4) A.M. Nyström; Wooley, K. L. The Importance of Chemistry in Creating Well-Defined Nanoscopic Embedded Therapeutics: Devices Capable of the Dual Functions of Imaging and Therapy. *Accounts of Chemical Research* **2011**, *44*, 969-978.
(5) R. Singh; H.S. Nalwa. Medical Applications of Nanoparticles in Biological Imaging, Cell Labeling, Antimicrobial Agents, and Anticancer Nanodrugs. *Journal of Biomedical Nanotechnology* **2011**, *7*, 489-503.
(6) T. Sun; Y.S. Zhang; B. Pang; D.C. Hyun; M. Yang; Y. Xia. Engineered nanoparticles for drug delivery in cancer therapy. *Angewandte Chemie International Edition* **2014**, *53*, 12320-12364.
(7) N. Larson; H. Ghandehari. Polymeric conjugates for drug delivery. *Chem. Mat.* **2012**, *24*, 840-853.
(8) R. Popovtzer; A. Agrawal; N.A. Kotov; A. Popovtzer; J. Balter; T.E. Carey; R. Kopelman. Targeted Gold Nanoparticles enable Molecular CT Imaging of Cancer *Nano Letters* **2008**, *8*, 4593-4596.
(9) H.B. Na; I.C. Song; T. Hyeon. Inorganic Nanoparticles for MRI Contrast Agents. *Advanced Materials* **2009**, *21*, 2133-2148.
(10) L.E. Cole; R.D. Ross; J.M.R. Tilley; T. Vargo-Gogola; R.K. Roeder. Gold nanoparticles as contrast agents in x-ray imaging and computed tomography. *Nanomedicine* **2015**, *10*, 321-341.
(11) H.M.E. Azzazy; M.M.H. Mansour. In vitro diagnostic prospects of nanoparticles. *Clinica Chimica Acta* **2009**, *403*, 1-8.
(12) X. Chi; D. Huang; Z. Zhao; Z. Zhou; Z. Yin; J. Gao. Nanoprobes for in vitro diagnostics of cancer and infectious diseases. *Biomaterials* **2012**, *33*, 189-206.
(13) N. Sanvicens; C. Pastells; N. Pascual; M.P. Marco. Nanoparticle-based biosensors for detection of pathogenic bacteria. *TrAC Trends in Analytical Chemistry* **2009**, *28*, 1243-1252.
(14) G.V. Kurlyandskaya; D.S. Portnov; I.V. Beketov; A. Larrañaga; A.P. Safronov; I. Orue; A.I. Medvedev; A.A. Chlenova; M.B. Sanchez-Ilarduya; A. Martinez-Amesti; A.V. Svalov. Nanostructured materials for magnetic biosensing. *Biochimica et Biophysica Acta (BBA) - General Subjects* **2017**, *1861*, 1494-1506.
(15) K. Saha; S.S. Agasti; C. Kim; X. Li; V.M. Rotello. Gold Nanoparticles in Chemical and Biological Sensing. *Chemical reviews* **2012**, *112*, 2739-2779.
(16) D.R. Viswambari; M. Doble; R.S. Verma. Nanomaterials for early detection of cancer biomarker with special emphasis on gold nanoparticles in immunoassays/sensors. *Biosensors and Bioelectronics* **2015**, *68*, 688-698.
(17) M. Hasanzadeh; N. Shadjou; M. De la Guardia. Iron and iron-oxide magnetic nanoparticles as signal-amplification elements in electrochemical biosensing. *TrAC Trends in Analytical Chemistry* **2015**, *72*, 1-9.
(18) I. Vasconcelos; C. Fernandes. Magnetic solid phase extraction for determination of drugs in biological matrices. *TrAC Trends in Analytical Chemistry* **2017**, *89*, 41-52.
(19) S. Bedanta; W. Kleemann. Supermagnetism. *The Journal of Physics D: Applied Physics* **2009**, *42*, 013001.
(20) C.L. Nehl; J.H. Hafner. Shape-dependent plasmon resonances of gold nanoparticles. *Journal of Materials Chemistry* **2008**, *18*, 2415-2419.
(21) K.K. Lance; E. Coronado; L.L. Zhao; G.C. Schatz. The Optical Properties of Metal Nanoparticles: The Influence of Size, Shape, and Dielectric Environment. *The Journal of Physical Chemistry B* **2003**, *107*, 668-677.
(22) C.C. Berry. Progress in functionalization of magnetic nanoparticles for applications in biomedicine. *Journal of Physics D: Applied Physics* **2009**, *42*, 224003.

(23) G. Bao; S. Mitragotri; S. Tong. Multifunctional nanoparticles for drug delivery and molecular imaging. *Annual review of biomedical engineering* **2013**, *15*, 253-282.
(24) K. Chatterjee; S. Sarkar; K. Jagajjanani Rao; S. Paria. Core/shell nanoparticles in biomedical applications. *Advaces in Colloid and Interface Science* **2014**, *209*, 8-39.
(25) C. Fang; M. Zhang. Multifunctional magnetic nanoparticles for medical imaging applications. *Journal of Materials Chemistry* **2009**, *19*, 6258-6266.
(26) S.K. Yen; P. Padmanabhan; S.T. Selvan. Multifunctional iron oxide nanoparticles for diagnostics, therapy and macromolecule delivery. *Theranostics* **2013**, *3*, 986-1003.
(27) W. Zhou; X. Gao; D. Liu; X. Chen. Gold Nanoparticles for In Vitro Diagnostics. *Chemical reviews* **2015**, *115*, 10575-10636.
(28) M. Arruebo; R. Fernández-Pacheco; M.R. Ibarra; J. Santamaría. Magnetic nanoparticles for drug delivery. *Nano Today* **2007**, *2*, 22-32.
(29) M. Banobre-Lopez; A. Teijeiro; J. Rivas. Magnetic nanoparticle-based hyperthermia for cancer treatment. *Reports of Practical Oncology and Radiotherapy* **2013**, *18*, 397-400.
(30) H. Lu; M. Zhang; Y. Yang; Q. Huang; T. Fukuda; Z. Wang; Y. Shen. A bioinspired multilegged soft millirobot that functions in both dry and wet conditions. *Nature communications* **2018**, *9*, 3944.
(31) S.M. Taimoory; J.F. Trant; A. Rahdar; M. Aliahmad; F. Sadeghfar; M. Hashemzaei. Importance of the Inter-Electrode Distance for the Electrochemical Synthesis of Magnetite Nanoparticles: Synthesis, Characterization, Computational Modelling, and Cytotoxicity. *e-Journal of Surface Science and Nanotechnology* **2017**, *15*, 31-39.
(32) J. Xu; H. Yang; W. Fu; K. Du; Y. Sui; J. Chen; Y. Zeng; M. Li; G. Zou. Preparation and magnetic properties of magnetite nanoparticles by sol–gel method. *Journal of Magnetism and Magnetic Materials* **2007**, *309*, 307-311.
(33) A. Taebin; K.J. Hun; Y. Hee-Man; L.J. Woo; K. Jong-Duk. Formation Pathways of Magnetite Nanoparticles by Coprecipitation Method. *The Journal of Physical Chemistry C* **2012**, *116*, 6069-6076.
(34) L.H. Reddy; J.L. Arias; J. Nicolas; P. Couvreur. Magnetic Nanoparticles: Design and Characterization, Toxicity and Biocompatibility, Pharmaceutical and Biomedical Applications. *Chemical reviews* **2012**, *112*, 5818-5878.
(35) Q. Li; C.W. Kartikowati; S. Horie; T. Ogi; T. Iwaki; K. Okuyama. Correlation between particle size/domain structure and magnetic properties of highly crystalline Fe_3O_4 nanoparticles. *Scientific Reports* **2017**, *7*, 9894.
(36) T.K. Jain; J. Richey; M. Strand; D.L. Leslie-Pelecky; C.A. Flask; V. Labhasetwar. Magnetic nanoparticles with dual functional properties: drug delivery and magnetic resonance imaging. *Biomaterials* **2008**, *29*, 4012-4021.
(37) W. Wu; C.Z. Jiang; V.A. Roy. Designed synthesis and surface engineering strategies of magnetic iron oxide nanoparticles for biomedical applications. *Nanoscale* **2016**, *8*, 19421-19474.
(38) R.A. Bohara; N.D. Thorat; S.H. Pawar. Role of functionalization: strategies to explore potential nano-bio applications of magnetic nanoparticles. *RSC Advances* **2016**, *6*, 43989-44012.
(39) C. Rümenapp; B. Gleich; A. Haase. Magnetic Nanoparticles in Magnetic Resonance Imaging and Diagnostics. *Pharmaceutical Research* **2012**, *29*, 1165-1179.
(40) N. Griffete; J. Fresnais; A. Espinosa; C. Wilhelm; A. Bee; C. Menager. Design of magnetic molecularly imprinted polymer nanoparticles for controlled release of doxorubicin under an alternative magnetic field in athermal conditions. *Nanoscale* **2015**, *7*, 18891-18896.
(41) A. Espinosa; R. Di Corato; J. Kolosnjaj-Tabi; P. Flaud; T. Pellegrino; C. Wilhelm. Duality of Iron Oxide Nanoparticles in Cancer Therapy: Amplification of Heating Efficiency by Magnetic Hyperthermia and Photothermal Bimodal Treatment. *ACS nano* **2016**, *10*, 2436-2446.
(42) H. Ittrich; K. Peldschus; N. Raabe; M. Kaul; G. Adam. Superparamagnetic Iron Oxide Nanoparticles in Biomedicine: Applications and Developments in Diagnostics and Therapy. *Fortschr Röntgenstr* **2013**, *185*, 1149–1166
(43) M. Bietenbeck; A. Florian; C. Faber; U. Sechtem; A. Yilmaz. Remote magnetic targeting of iron oxide nanoparticles for cardiovascular diagnosis and therapeutic drug delivery: where are we now? *International journal of nanomedicine* **2016**, *11*, 3191-3203.

(44) R. Mejias; S. Perez-Yague; L. Gutierrez; L.I. Cabrera; R. Spada; P. Acedo; C.J. Serna; F.J. Lazaro; A. Villanueva; P. Morales Mdel; D.F. Barber. Dimercaptosuccinic acid-coated magnetite nanoparticles for magnetically guided in vivo delivery of interferon gamma for cancer immunotherapy. *Biomaterials* **2011**, *32*, 2938-2952.
(45) A.K. Silva; C. Menager; C. Wilhelm. Magnetic drug carriers: bright insights from light-responsive magnetic liposomes. *Nanomedicine* **2015**, *10*, 2797-2799.
(46) M.M. Yallapu; N. Chauhan; S.F. Othman; V. Khalilzad-Sharghi; M.C. Ebeling; S. Khan; M. Jaggi; S.C. Chauhan. Implications of protein corona on physico-chemical and biological properties of magnetic nanoparticles. *Biomaterials* **2015**, *46*, 1-12.
(47) D.E. Owens III; N.A. Peppas. Opsonization, biodistribution, and pharmacokinetics of polymeric nanoparticles. *International journal of pharmaceutics* **2006**, *307*, 93-102.
(48) L. Pang; C. Zhang; J. Qin; L. Han; R. Li; C. Hong; H. He; Wang, J. A novel strategy to achieve effective drug delivery: exploit cells as carrier combined with nanoparticles. *Drug delivery* **2017**, *24*, 83-91.
(49) M. Muthana; S.D. Scott; N. Farrow; F. Morrow; C. Murdoch; S. Grubb; N. Brown; J. Dobson; C.E. Lewis. A novel magnetic approach to enhance the efficacy of cell-based gene therapies. *Gene therapy* **2008**, *15*, 902-910.
(50) C.A. Quinto; P. Mohindra; S. Tong; G. Bao. Multifunctional superparamagnetic iron oxide nanoparticles for combined chemotherapy and hyperthermia cancer treatment. *Nanoscale* **2015**, *7*, 12728-12736.
(51) B. Sanz; M.P. Calatayud; T.E. Torres; M.L. Fanarraga; M.R. Ibarra; G.F. Goya. Magnetic hyperthermia enhances cell toxicity with respect to exogenous heating. *Biomaterials* **2017**, *114*, 62-70.
(52) D. Shi; M.E. Sadat; A.W. Dunn; D.B. Mast. Photo-fluorescent and magnetic properties of iron oxide nanoparticles for biomedical applications. *Nanoscale* **2015**, *7*, 8209-8232.
(53) B. Ding; S. Shen; L. Wu; X. Qi; H. Ni; Y. Ge. Doxorubicin-loaded Fe_3O_4@SiO_2 Nanoparticles as Magnetic Targeting Agents for Combined Photothermal-chemotherapy of Cancer. *Chemistry Letters* **2015**, *44*, 858-860.
(54) Z. Gao; X. Liu; G., D.; F. Zhou; L. Zhang; Q. Wang; J. Lu. Fe_3O_4@$mSiO_2$-FA-CuS-PEG Nanocomposites for Magnetic Resonance Imaging and Targeted Chemo-photothermal Synergistic Therapy of Cancer Cells. *Dalton Transactions* **2016**, *45*, 13456-13465.
(55) S. Elingarami; M. Liu; Z. Li; N. He. Surface-Engineered Magnetic Nanoparticles for Molecular Detection of Infectious Agents and Cancer. *J. Nanosci. Nanotechnol.* **2013**, *13*, 3204-3213.
(56) H. Gu; K. Xu; C. Xu; B. Xu. Biofunctional magnetic nanoparticles for protein separation and pathogen detection. *Chemical communications* **2006**, *0*, 941-949.
(57) A.L. Chun. Nanoparticles offer hope for TB detection. *Nature Nanotechnology* **2009**, *4*, 1-2.
(58) H. Xu; Z.P. Aguilar; L. Yang; M. Kuang; H. Duan; Y. Xiong; H. Wei; A. Wang. Antibody conjugated magnetic iron oxide nanoparticles for cancer cell separation in fresh whole blood. *Biomaterials* **2011**, *32*, 9758-9765.
(59) M. Lewin; N. Carlesso; C.H. Tung; X.W. Tang; D. Cory; D.T. Scadden; R. Weissleder. Tat peptide-derivatized magnetic nanoparticles allow in vivo tracking and recovery of progenitor cells. *Nature Biotechnology* **2000**, *18*, 410-414.
(60) Y. Chen; Y. Xianyu; Y. Wang; X. Zhang; R. Cha; J. Sun; X. Jiang. One-Step Detection of Pathogens and Viruses: Combining Magnetic Relaxation Switching and Magnetic Separation. *ACS nano* **2015**, *9*, 3184-3191.
(61) K. Atacan; B. Çakıroğlu; M. Özacar. Improvement of the stability and activity of immobilized trypsin on modified Fe_3O_4 magnetic nanoparticles for hydrolysis of bovine serum albumin and its application in the bovine milk. *Food Chemistry* **2016**, *212*, 460-468.
(62) Y.T. Zhu; X.Y. Ren; Y.M. Liu; Y. Wei; L.S. Qing; X. Liao. Covalent immobilization of porcine pancreatic lipase on carboxyl-activated magnetic nanoparticles: Characterization and application for enzymatic inhibition assays. *Materials Science and Engineering C: Materials for Biological Applications* **2014**, *38*, 278-285.

(63) M. Broto; J.P. Salvador; R. Galve; M.P. Marco. Biobarcode assay for the oral anticoagulant acenocoumarol. *Talanta* **2018**, *178*, 308-314.
(64) D.M. Bruls; T.H. Evers; J.A.H. Kahlman; P.J.W. Van Lankvelt; M. Ovsyanko; E.G.M. Pelssers; J.J.H.B. Schleipen; F.K. De Theije; C.A. Verschuren; T. Van der Wijk; J.B.A. Van Zon; W.U. Dittmer; A.H.J. Immink; J.H. Nieuwenhuis; M.W.J. Prins. Rapid integrated biosensor for multiplexed immunoassays based on actuated magnetic nanoparticles. *Lab on a Chip* **2009**, *9*, 3504-3510.
(65) D.G. Pinacho; F. Sánchez-Baeza; M.I. Pividori; M.P. Marco. Electrochemical Detection of Fluoroquinolone Antibiotics in Milk Using a Magneto Immunosensor. *Sensors* **2014**, *14*, 15965-15980.
(66) R.G. Chaudhuri; S. Paria. Core/shell nanoparticles: classes, properties, synthesis mechanisms, characterization, and applications. *Chemical reviews* **2012**, *112*, 2373-2433.
(67) B. Kalska-Szostko; U. Wykowska; D. Satuła. Magnetic nanoparticles of core–shell structure. *Colloids and Surfaces A: Physicochemical and Engineering Aspects* **2015**, *481*, 527-536.
(68) J.R. McCarthy; R. Weissleder. Multifunctional magnetic nanoparticles for targeted imaging and therapy. *Advanced drug delivery reviews* **2008**, *60*, 1241-1251.
(69) O. Chen; L. Riedemann; F. Etoc; H. Herrmann; M. Coppey; M. Barch; C.T. Farrar; J. Zhao; O.T. Bruns; H. Wei; P. Guo; J. Cui; R. Jensen; Y. Chen; D.K. Harris; J.M. Cordero; Z. Wang; A. Jasanoff; D. Fukumura; R. Reimer; M. Dahan; R.K. Jain; M.G. Bawendi. Magneto-fluorescent core-shell supernanoparticles. *Nature Communication* **2014**, *5*, 5093.
(70) X. Yang; H. Hong; J.J. Grailer; I.J. Rowland; A. Javadi; S.A. Hurley; Y. Xiao; Y. Yang; Y. Zhang; R.J. Nickles; W. Cai; D.A. Steeber; S. Gong. cRGD-functionalized, DOX-conjugated, and ^{64}Cu-labeled superparamagnetic iron oxide nanoparticles for targeted anticancer drug delivery and PET/MR imaging. *Biomaterials* **2011**, *32*, 4151-4160.
(71) J. Xie; K. Chen; J. Huang; S. Lee; J. Wang; J. Gao; X. Li; X. Chen. PET/NIRF/MRI triple functional iron oxide nanoparticles. *Biomaterials* **2010**, *31*, 3016-3022.
(72) L. Maggini; I. Cabrera; A. Ruiz-Carretero; E.A. Prasetyanto; E. Robinet; L. De Cola. Breakable mesoporous silica nanoparticles for targeted drug delivery. *Nanoscale* **2016**, *8*, 7240-7247.
(73) Y. Wang; Q. Zhao; N. Han; L. Bai; J. Li; J. Liu; E. Che; L. Hu; Q. Zhang; T. Jiang; S. Wang. Mesoporous silica nanoparticles in drug delivery and biomedical applications. *Nanomedicine: Nanotechnology, Biology and Medicine* **2015**, *11*, 313-327.
(74) W. Stöber; A. Fink; E. Bohn. Controlled growth of monodisperse silica spheres in the micron size range. *Journal of Colloid and Interface Science* **1968**, *26*, 62-69.
(75) T.G. Waddell; D.E. Leyden; M.T. DeBello. The nature of organosilane to silica-surface bonding. *The Journal of the American Chemical Society* **1981**, *103*, 5303-5307.
(76) C. Zhang; B. Wängler; B. Morgenstern; H. Zentgraf; M. Eisenhut; H. Untenecker; R. Krüger, R. H.; C. Seliger; W. Semmler; F. Kiessling. Silica- and Alkoxysilane-Coated Ultrasmall Superparamagnetic Iron Oxide Particles: A Promising Tool To Label Cells for Magnetic Resonance Imaging. *Langmuir : the ACS journal of surfaces and colloids* **2007**, *23*, 1427-1434.
(77) M.C. Daniel; D. Astruc. Gold nanoparticles: assembly, supramolecular chemistry, quantum-size-related properties, and applications toward biology, catalysis, and nanotechnology. *Chemical reviews* **2004**, *104*, 293-346.
(78) E.C. Dreaden; A.M. Alkilany; X. Huang; C.J. Murphy; M.A. El-Sayed. The golden age: gold nanoparticles for biomedicine. *Chemical Society Reviews* **2012**, *41*, 2740-2779.
(79) S. Eustis; M.A. El-Sayed. Why gold nanoparticles are more precious than pretty gold: Noble metal surface plasmon resonance and its enhancement of the radiative and nonradiative properties of nanocrystals of different shapes. *Chemical Society Reviews* **2006**, *35*, 209-217.
(80) A. Espinosa; M. Bugnet; G. Radtke; S. Neveu; G.A. Botton; C. Wilhelm; A. Abou-Hassan. Can magneto-plasmonic nanohybrids efficiently combine photothermia with magnetic hyperthermia? *Nanoscale* **2015**, *7*, 18872-18877.

(81) E. Pensa; E. Cortés; G. Corthey; P. Carro; C. Vericat; M.H. Fonticelli; G. Benítez; A.A. Rubert; R.C. Salvarezza. The Chemistry of the Sulfur–Gold Interface: In Search of a Unified Model. *Accounts of Chemical Research* **2012**, *45*, 1183-1192.
(82) R.G. Nuzzo; B.R. Zegarski; L.H. Dubois. Fundamental Studies of the Chemisorption of Organosulfur Compounds on Au(111). Implications for Molecular Self-Assembly on Gold Surfaces. *The Journal of the American Chemical Society* **1987**, *109*, 733-740.
(83) S. Rana; A. Bajaj; R. Mout; V.M. Rotello. Monolayer coated gold nanoparticles for delivery applications. *Advanced drug delivery reviews* **2012**, *64*, 200-216.
(84) J. Manson; D. Kumar; B.J. Meenan; D. Dixon. Polyethylene glycol functionalized gold nanoparticles: the influence of capping density on stability in various media. *Gold Bulletin* **2011**, *44*, 99-105.
(85) D. Kim; S. Park; J.H. Lee; Y.Y. Jeong; S. Jon. Antibiofouling Polymer-Coated Gold Nanoparticles as a Contrast Agent for in Vivo X-ray Computed Tomography Imaging. *The Journal of the American Chemical Society* **2007**, *129*, 7661-7665.
(86) Y.T. Liu; L. Yan; L.M. Sun; H.Q. Li; H.H. Li: *Mixed short-chain PEG self-assembled monolayer preparation and immobilization of protein*, 2014; Vol. 42. pp. 69-74.
(87) R.L. Letsinger; R. Elghanian; G. Viswanadham; C.A. Mirkin. Use of a Steroid Cyclic Disulfide Anchor in Constructing Gold Nanoparticles-Oligonucleotide Conjugates. *Bioconjugate Chemistry* **2000**, *11*, 289-291.
(88) J. Luo; Q. Fan; M. Suzuki; I.S. Suzuki; M.H. Engelhard; Y. Lin; N.Kim; J.Q. Wang; C.J. Zhong. Monodispersed Core−Shell Fe_3O_4@Au Nanoparticles. *The Journal of Physical Chemistry B* **2005**, *109*, 21593-21601.
(89) Y. Xing; Y.Y. Jin; J.C. Si; M.L. Peng; X.F. Wang; C. Chen; Y.L. Cui. Controllable synthesis and characterization of Fe_3O_4/Au composite nanoparticles. *Journal of Magnetism and Magnetic Materials* **2015**, *380*, 150-156.
(90) H. Maleki; A. Simchi; M. Imani; B.F.O. Costa. Size-controlled synthesis of superparamagnetic iron oxide nanoparticles and their surface coating by gold for biomedical applications. *Journal of Magnetism and Magnetic Materials* **2012**, *324*, 3997-4005.
(91) S.V. Salihov; Y.A. Ivanenkov; S.P. Krechetov; M.S. Veselov; N.V. Sviridenkova; A.G. Savchenko; N.L. Klyachko; Y.I. Golovin; N.V. Chufarova; E.K. Beloglazkina; A.G. Majouga. Recent advances in the synthesis of Fe_3O_4@Au core/shell nanoparticles. *Journal of Magnetism and Magnetic Materials* **2015**, *394*, 173-178.
(92) H. Cai; N. Zhu; Y. Jiang; P. He; Y. Fang. Cu@Au alloy nanoparticle as oligonucleotides labels for electrochemical stripping detection of DNA hybridization. *Biosensors and Bioelectronics* **2003**, *18*, 1311-1319.
(93) P. Li; L. Li; Y. Zhao; L. Sun; Y. Zhang. Selective binding and magnetic separation of histidine-tagged proteins using Fe_3O_4/Cu-apatite nanoparticles. *Journal of inorganic biochemistry* **2016**, *156*, 49-54.
(94) M. Tang; S. Zhang; X. Li; X. Pang; H. Qiu. Fabrication of magnetically recyclable Fe_3O_4@Cu nanocomposites with high catalytic performance for the reduction of organic dyes and 4-nitrophenol. *Materials Chemistry and Physics* **2014**, *148*, 639-647.
(95) D. Patel; A. Kell; B. Simard; B. Xiang; H.Y. Lin; G. Tian. The cell labeling efficacy, cytotoxicity and relaxivity of copper-activated MRI/PET imaging contrast agents. *Biomaterials* **2011**, *32*, 1167-1176.
(96) R. Massart. Preparation of Aqueous Magnetic Liquids in Alkaline and Acidic Media. *IEEE Transactions on Magnetics* **1981**, *17*, 1247-1248.
(97) K.J. Gallagher; W. Feitknecht; U. Mannweiler. Mechanism of Oxidation of Magnetite to γ-Fe_2O_3. *Nature* **1968**, *217*, 1118.
(98) K. Seo; K. Sinha; E. Novitskaya; O.A. Graeve. Polyvinylpyrrolidone (PVP) effects on iron oxide nanoparticle formation. *Materials Letters* **2018**, *215*, 203-206.
(99) F. De Angelis. Multitasking Nanoparticles for Theranostics: from the Synthesis to *in Vitro* Applications. Sapienza Università di Roma, 2016.
(100) D. Passeri; C. Dong; M. Reggente; L. Angeloni; M. Barteri; F.A. Scaramuzzo; F. De Angelis; F. Marinelli; F. Antonelli; F. Rinaldi; C. Marianecci; M. Carafa; A. Sorbo; D. Sordi; I.W.

Arends; M. Rossi. Magnetic force microscopy: quantitative issues in biomaterials. *Biomatter* **2014**, *4*, e29507.
(101) F. De Angelis; G. Berardi; F.A. Scaramuzzo; M. Liberatore; M. Barteri. Internalisation of core-shell superparamagnetic nanoparticles into human granulocytes. *International Journal of Nanotechnology* **2016**, *13*, 659-666.
(102) J. Xiong; Y. Wang; Q. Xue; X. Wu. Synthesis of highly stable dispersions of nanosized copper particles using l-ascorbic acid. *Green Chemistry* **2011**, *13*, 900-904.
(103) M.N. Nadagouda; R.S. Varma. A Greener Synthesis of Core (Fe, Cu)-Shell (Au, Pt, Pd, and Ag) using ascorbic acid. *Crystal Growth & Design* **2007**, *7*, 2582-2587.
(104) M. Sonmez; M. Georgescu; L. Alexandrescu; D. Gurau; A. Ficai; D. Ficai; E. Andronescu. Synthesis and Applications of Fe_3O_4/SiO_2 Core-Shell Materials. *Current Pharmaceutical Design* **2015**, *21*, 5324-5335.
(105) H.L. Ding; Y.X. Zhang; S. Wang; J.M. Xu; S.C. Xu; G.H. Li. $Fe_3O_4@SiO_2$ Core/Shell Nanoparticles: The Silica Coating Regulations with a Single Core for Different Core Sizes and Shell Thicknesses. *Chem. Mat.* **2012**, *24*, 4572-4580.
(106) R.L. Siegel; K.D. Miller; A. Jemal. Cancer Statistics, 2017. *CA: a cancer journal for clinicians* **2017**, *67*, 7-30.
(107) V. Sanna; N. Pala; M. Sechi. Targeted therapy using nanotechnology: focus on cancer. *International journal of nanomedicine* **2014**, *9*, 467-483.
(108) L. Jinxia. Nanotechnology-based platform for early diagnosis of cancer. *Science Bulletin* **2015**, *60*, 488-490.
(109) A Phase III Study of NK105 in Patients With Breast Cancer. https://clinicaltrials.gov/ct2/show/record/NCT01644890.
(110) O.L. Gobbo; K. Sjaastad; M.W. Radomski; Y. Volkov; A. Prina-Mello. Magnetic Nanoparticles in Cancer Theranostics. *Theranostics* **2015**, *5*, 1249-1263.
(111) N. Bertrand; J. Wu; X. Xu; N. Kamaly; O.C. Farokhzad. Cancer Nanotechnology: The impact of passive and active targeting in the era of modern cancer biology. *Advanced drug delivery reviews* **2014**, *66*, 2-25.
(112) D. Peer; J.M. Karp; S. Hong; O.C. Farokhzad; R. Margalit; R. Langer. Nanocarriers as an emerging platform for cancer therapy. *Nature Nanotechnology* **2007**, *2*, 751-760.
(113) K. Greish: Enhanced Permeability and Retention (EPR) Effect for Anticancer Nanomedicine Drug Targeting. In *Cancer Nanotechnology: Methods and Protocols*; Grobmyer, S. R., Moudgil, B. M., Eds.; Humana Press: Totowa, NJ, 2010; pp 25-37.
(114) J. Fang; H. Nakamura; H. Maeda. The EPR effect: Unique features of tumor blood vessels for drug delivery, factors involved, and limitations and augmentation of the effect. *Advanced drug delivery reviews* **2011**, *63*, 136-151.
(115) M. Wang; M. Thanou. Targeting nanoparticles to cancer. *Pharmacological Research* **2010**, *62*, 90-99.
(116) S. Xu; B.Z. Olenyuk; C.T. Okamoto; S.F. Hamm-Alvarez. Targeting receptor-mediated endocytotic pathways with nanoparticles: rationale and advances. *Advanced drug delivery reviews* **2013**, *65*, 121-138.
(117) C.H.J. Choi; C.A. Alabi; P. Webster; M.E. Davis. Mechanism of active targeting in solid tumors with transferrin-containing gold nanoparticles. *Proceedings of the National Academy of Sciences USA* **2010**, *107*, 1235-1240.
(118) Y. Lu; P.S. Low. Folate-mediated delivery of macromolecular anticancer therapeutic agents☆. *Advanced drug delivery reviews* **2012**, *64*, 342-352.
(119) M. Lucock. Folic Acid: Nutritional Biochemistry, Molecular Biology, and Role in Disease Processes. *Molecular Genetics and Metabolism* **2000**, *71*, 121-138.
(120) A.S. Wibowo; M. Singh; K.M. Reeder; J.J. Carter; A.R.Kovach; W. Meng; M. Ratnam; F. Zhang; III, C. E. D. Structures of human folate receptors reveal biological trafficking states and diversity in folate and antifolate recognition. *Proceedings of the National Academy of Sciences USA* **2013**, *110*, 15180-15188.

(121) J. Jolivet; R.L. Schilsky; B.D. Bailey; J.C. Drake; B.A. Chabner. Synthesis, Retention, and Biological Activity of Methotrexate Polyglutamates in Cultured Human Breast Cancer Cells. *The Journal of Clinical Investigation* **1982**, *70*, 351-360.
(122) B.A. Chabner; T.G. Roberts Jr. Chemotherapy and the war on cancer. *Nature Reviews Cancer* **2005**, *5*, 65-72.
(123) A. Cheung; H.J. Bax; D.H. Josephs; K.M. Ilieva; G. Pellizzari; J. Opzoomer; J. Bloomfield; M. Fittali; A. Grigoriadis; M. Figini; S. Canevari; J.F. Spicer; A.N. Tutt; S.N. Karagiannis. Targeting folate receptor alpha for cancer treatment. *Oncotarget* **2016**, *7*, 52553-52574.
(124) F. M. Sirotnak; B. Tolner. Carrier-mediated membrane transport of folates in mammalian cells. *Annual Reviews of Nutrition* **1999**, *19*, 91-122.
(125) N. Parker; M.J. Turk; E. Westrick; J.D. Lewis; P.S. Low; C.P. Leamon. Folate receptor expression in carcinomas and normal tissues determined by a quantitative radioligand binding assay. *Analytical Biochemistry* **2005**, *338*, 284-293.
(126) L.E. Kelemen. The role of folate receptor alpha in cancer development, progression and treatment: cause, consequence or innocent bystander? *International Journal of Cancer* **2006**, *119*, 243-250.
(127) P.T. Wong; S.K. Choi. Mechanisms and Implications of Dual-Acting Methotrexate in Folate-Targeted Nanotherapeutic Delivery. *International Journal of Molecular Sciences* **2015**, *16*, 1772-1790.
(128) S. Wang; P.S. Low. Folate-mediated targeting of antineoplastic drugs, imaging agents, and nucleic acids to cancer cells. *Journal of Controlled Release* **1998**, *53*, 39-48.
(129) Y. Takemura; H. Kobayashi; H. Miyachi. Cellular and molecular mechanisms of resistance to antifolate drugs: new analogues and approaches to overcome the resistance. *International Journal of Hematology* **1997**, *66*, 459-477.
(130) L. Liu; K.T. Yong; I. Roy; W.C. Law; L. Ye; J. Liu; J. Liu; R. Kumar; X. Zhang; P.N. Prasad. Bioconjugated pluronic triblock-copolymer micelle-encapsulated quantum dots for targeted imaging of cancer: in vitro and in vivo studies. *Theranostics* **2012**, *2*, 705-713.
(131) A. Sulistio; J. Lowenthal; A. Blencowe; M.N. Bongiovanni; L. Ong; Sally L. Gras; X. Zhang; G.G. Qiao. Folic Acid Conjugated Amino Acid-Based Star Polymers for Active Targeting of Cancer Cells. *Biomacromolecules* **2011**, *12*, 3469-3477.
(132) S.S. Abolmaali; A.M. Tamaddon; R. Dinarvand. A review of therapeutic challenges and achievements of methotrexate delivery systems for treatment of cancer and rheumatoid arthritis. *Cancer chemotherapy and pharmacology* **2013**, *71*, 1115-1130.
(133) N. Kohler; C. Sun; A. Fichtenholtz; J. Gunn; C. Fang; M. Zhang. Methotrexate-immobilized poly(ethylene glycol) magnetic nanoparticles for MR imaging and drug delivery. *Small* **2006**, *2*, 785-792.
(134) G.Ph. Biewenga; G.R.M.M. Haenen; A. Bast. The Pharmacology of the Antioxidant Lipoic Acid. *General Pharmacology* **1997**, *29*, 315-331.
(135) C. Nativi; C. Ghelardini; G. La Marca; E. Dragoni. Compounds with both analgesic and anti-hyperalgesic efficacy WO/2011/080725A1.
(136) D.I. Gittins; F. Caruso. Tailoring the Polyelectrolyte Coating of Metal Nanoparticles. *The Journal of Physical Chemistry B* **2001**, *105*, 6846-6852.
(137) H.J.P. Ryser; W.C. Shen. Conjugation of methotrexate to poly(l-lysine) increases drug transport and overcomes drug resistance in cultured cells. *Proceedings of the National Academy of Sciences USA* **1978**, *78*, 3867-3870.
(138) X. Wang; F. Wei; A. Liu; L. Wang; J.C. Wang; L. Ren; W. Liu; Q. Tu; L. Li; J. Wang. Cancer stem cell labeling using poly(L-lysine)-modified iron oxide nanoparticles. *Biomaterials* **2012**, *33*, 3719-3732.
(139) R.J. Lee; P.S. Low. Delivery of Liposomes into Cultured KB Cells via Folate Receptor-mediated Endocytosis. *The Journal of Biological Chemistry* **1994**, *269*, 3198-3204.
(140) C. Lorente; A.H. Thomas. Photophysics and Photochemistry of Pterins in Aqueous Solution. *Accounts of Chemical Research* **2006**, *39*, 395-402.

(141) A.H. Thomas; C. Lorente; A.L. Capparelli; M. Raj Pokhrel; A.M. Braun; E. Oliveros. Fluorescence of pterin, 6-formylpterin, 6-carboxypterin and folic acid in aqueous solution: pH effect. *Photochemical & Photobiological Sciences* **2002**, *1*, 421-426.
(142) R. Meier; T.D. Henning; S. Boddington; S. Tavri; S. Arora; G. Piontek; M. Rudelius; C. Corot; H.E. Daldrup-Link. Breast Cancers: MR Imaging of Folate-Receptor Expression with the Folate-Specific Nanoparticle P1133 *Radiology* **2010**, *255*, 527-535.
(143) V. Vichai; K. Kirtikara. Sulforhodamine B colorimetric assay for cytotoxicity screening. *Nature Protocols* **2006**, *1*, 1112-1116.
(144) N. Yang; H. Zhang; M. Wang; Q. Hao; H. Sun. Iron and bismuth bound human serum transferrin reveals a partially-opened conformation in the N-lobe. *Scientific Reports* **2012**, *2*, 999.
(145) Z.M. Qian; H. Li; H. Sun; K. Ho. Targeted Drug Delivery via the Transferrin Receptor-Mediated Endocytosis Pathway. *Pharmacological reviews* **2002**, *54*, 561-587.
(146) T. Inoue; P.G. Cavanaugh; P.A. Steck; N. Brunner; G.L. Nicolson. Differences in Transferrin Response and Numbers of Transferrin Receptors in Rat and Human Mammary Carcinoma Lines of Different Metastatic Potentials. *Journal of Cellular Physiology* **1993**, *156*, 212-217.
(147) T.R. Daniels; E. Bernabeu; J.A. Rodríguez; S. Patel; M. Kozman; D.A. Chiappetta; E. Holler; J.Y. Ljubimova; G. Helguera; M.L. Penichet. The transferrin receptor and the targeted delivery of therapeutic agents against cancer. *Biochimica et Biophysica Acta (BBA) - General Subjects* **2012**, *1820*, 291-317.
(148) Z. Shao; J. Shao; B. Tan; S. Guan; Z. Liu; Z. Zhao; F. He; J. Zhao. Targeted lung cancer therapy: preparation and optimization of transferrin-decorated nanostructured lipid carriers as novel nanomedicine for co-delivery of anticancer drugs and DNA. *International journal of nanomedicine* **2015**, *10*, 1223-1233.
(149) Y. Han; Y. Zhang; D. Li; Y. Chen; J. Sun; F. Kong. Transferrin-modified nanostructured lipid carriers as multifunctional nanomedicine for codelivery of DNA and doxorubicin. *International journal of nanomedicine* **2014**, *9*, 4107-4116.
(150) L. Chaiet; F.J. Wolf. The properties of streptavidin, a biotin-binding protein produced by Streptomycetes. *Archives of Biochemistry and Biophysics* **1964**, *106*, 1-5.
(151) B.A. Katz; R.T. Cass. In Crystals of Complexes of Streptavidin with Peptide Ligands Containing the HPQ Sequence the pKa of the Peptide Histidine Is Less than 3.0 *The Journal of Biological Chemistry* **1997**, *272*, 13220-13228.
(152) M. Wilchek; E.A. Bayer. The avidin-biotin complex in immunology. *Immunology Today* **1984**, *5*, 39-43.
(153) E.P. Diamandis; T.K. Christopoulos. The Biotin-(Strept)Avidin System: Principlesand Applicationsin Biotechnology. *Clinical Chemistry* **1991**, *37*, 625-636.
(154) N. Nath; A. Chilkoti. A Colorimetric Gold Nanoparticle Sensor To Interrogate Biomolecular Interactions in Real Time on a Surface. *Analytical Chemistry* **2002**, *74*, 504-509.
(155) J. Wu; Y. Chen; M. Yang; Y. Wang; C. Zhang; M. Yang; J. Sun; M. Xie; X. Jiang. Streptavidin-biotin-peroxidase nanocomplex-amplified microfluidics immunoassays for simultaneous detection of inflammatory biomarkers. *Analytica Chimica Acta* **2017**, *982*, 138-147.
(156) L. Wang; Y. Zhang; X. Gao; Z. Duan; S. Wang. Determination of Chloramphenicol Residues in Milk by Enzyme-Linked Immunosorbent Assay: Improvement by Biotin−Streptavidin-Amplified System. *Journal of Agricultural and Food Chemistry* **2010**, *58*, 3265-3270.
(157) Y. Li; Y. Zhang; L. Jiang; P.K. Chu; Y. Dong; Q. Wei. A sandwich-type electrochemical immunosensor based on the biotin- streptavidin-biotin structure for detection of human immunoglobulin G. *Scientific Reports* **2016**, *6*, 22694.
(158) H.L. Liu; C.H. Sonn; J.H. Wu; K.M. Lee; Y.K. Kim. Synthesis of streptavidin-FITC-conjugated core–shell Fe_3O_4-Au nanocrystals and their application for the purification of CD4+ lymphocytes. *Biomaterials* **2008**, *29*, 4003-4011.
(159) R. De Palma; C. Liu; F. Barbagini; G. Reekmans; K. Bonroy; W. Laureyn; G. Borghs; G. Maes. Magnetic Particles as Labels in Bioassays: Interactions between a Biotinylated Gold

Substrate and Streptavidin Magnetic Particles. *The Journal of Physical Chemistry C* **2007**, *111*, 12227-12235.
(160) F. Pierigè; S. Serafini; L. Rossi; M. Magnani. Cell-based drug delivery. *Advanced drug delivery reviews* **2008**, *60*, 286-295.
(161) C. Eyileten; K. Majchrzak; Z. Pilch; K. Tonecka; J. Mucha; B. Taciak; K. Ulewicz; K. Witt; A. Boffi; M. Krol; T. P. Rygiel. Immune Cells in Cancer Therapy and Drug Delivery. *Mediators of Inflammation* **2016**, *2016*, 13 pages.
(162) M.R. Choi; R. Bardhan; K.J. Stanton-Maxey; S. Badve; H. Nakshatri; K.M. Stantz; N. Cao; N.J. Halas; Clare, S. E. Delivery of nanoparticles to brain metastases of breast cancer using a cellular Trojan horse. *Cancer Nanotechnology* **2012**, *3*, 47-54.
(163) A.C. Anselmo; S. Mitragotri. Cell-Mediated Delivery of Nanoparticles: Taking Advantage of Circulatory Cells to Target Nanoparticles. *Journal of Controlled Release* **2014**, *28*, 531-541.
(164) H. Dou; C.J. Destache; J.R. Morehead; R.L. Mosley; M.D. Boska; J. Kingsley; S. Gorantla; L. Poluektova; J.A. Nelson; M. Chaubal; J. Werling; J. Kipp; B.E. Rabinow; H.E. Gendelman. Development of a macrophage-based nanoparticle platform for antiretroviral drug delivery. *Blood* **2006**, *108*, 2827-2835.
(165) A.M. Brynskikh; Y. Zhao; R.L. Mosley; S. Li; M.D. Boska; N.L. Klyachko; A.V. Kabanov; H.E. Gendelman; E.V. Batrakova. Macrophage delivery of therapeutic nanozymes in a murine model of Parkinson's disease. *Nanomedicine* **2010**, *5*, 379-396.
(166) X. Dong; D. Chu; Z. Wang. Leukocyte-mediated Delivery of Nanotherapeutics in Inflammatory and Tumor Sites *Theranostics* **2017**, *7*, 751-763.
(167) M.R. Choi; K.J. Stanton-Maxey; J.K. Stanley; C.S. Levin; R. Bardhan; D. Akin; S. Badve; J. Sturgis; J.P. Robinson; R. Bashir; N.J. Halas; S.E. Clare. A Cellular Trojan Horse for Delivery of Therapeutic Nanoparticles into Tumors. *Nano Letters* **2007**, *7*, 3759-3765.
(168) J. Xue; Z. Zhao; L. Zhang; L. Xue; S. Shen; Y. Wen; Z. Wei; L.Wang; L. Kong; H. Sun; Q.Ping; R. Mo; C. Zhang. Neutrophil-mediated anticancer drug delivery for suppression of postoperative malignant glioma recurrence. *Nature Nanotechnology* **2017**, *12*, 692-700.
(169) E.V. Batrakova; H.E. Gendelman; A.V. Kabanov. Cell-mediated drug delivery. *Expert Opinion on Drug Delivery* **2011**, *8*, 415-433.
(170) S.K. Patel; J. M. Janjic. Macrophage Targeted Theranostics as Personalized Nanomedicine Strategies for Inflammatory Diseases. *Theranostics* **2015**, *5*, 150-172.
(171) Vinogradov, S.; Warren, G.; Wei, X. Macrophages associated with tumors as potential targets and therapeutic intermediates. *Nanomedicine* **2014**, *9*, 695-707.
(172) J. Choi; H.Y. Kim; E.J. Ju; J. Jung; J. Park; H.K. Chung; J.S. Lee; J.S. Lee; H.J. Park; S.Y. Song; S.Y. Jeong; E.K. Choi. Use of macrophages to deliver therapeutic and imaging contrast agents to tumors. *Biomaterials* **2012**, *33*, 4195-4203.
(173) L. Pang; J. Qin; L. Han; W. Zhao; J. Liang; Z. Xie; P. Yang; J. Wang. Exploiting macrophages as targeted carrier to guide nanoparticles into glioma. *Oncotarget* **2016**, *7*, 37081-37091.
(174) M. Muthana; A.J. Kennerley; R. Hughes; E. Fagnano; J. Richardson; M. Paul; C. Murdoch; F. Wright; C. Payne; M.F. Lythgoe; N. Farrow; J. Dobson; J. Conner; J.M. Wild; C. Lewis. Directing cell therapy to anatomic target sites in vivo with magnetic resonance targeting. *Nature communications* **2015**, *6*, 8009-8019.
(175) M. Gonçalves; T. Sameiro. Fluorescent Labeling of Biomolecules with Organic Probes. *Chemical reviews* **2009**, *109*, 190-212.
(176) S. Tsuchiya; M. Yamabe; Y. Yamaguchi; Y. Kobayashi; T. Konno; K. Tada. Establishment And Characterization Of A Human Acute Monocytic Leukemia Cell Line (Thp-1). *International Journal of Cancer* **1980**, *26*, 171-176.
(177) J. Auwerx. The human leukemia cell line, THP-1 : A multifacetted model for the study of monocyte-macrophage differentiation. *Experientia* **1991**, *47*, 22-31.
(178) R. Andreesen; J. Osterholz; H. Bodemann; K.J. Bross; U. Costabel; G.W. Löhr. Expression of transferrin receptors and intracellular ferritin during terminal differentiation of human monocytes. *Blut* **1984**, *49*, 195-202.

(179) N.S. Iacobellis; P. Lavermicocca; I. Grgurina; M. Simmaco; A. Ballio. Phytotoxic properties of Pseudomonas syringae pv. syringae toxins. *Physiological and Molecular Plant Pathology* **1992**, *40*, 107-116.
(180) C. L. Bender; F. Alarcon-Chaidez; D.C. Gross. *Pseudomonas syringae* Phytotoxins: Mode of Action, Regulation, and Biosynthesis by Peptide and Polyketide Synthetases. *Microbiology and Molecular Biology Reviews* **1999**, *63*, 266-292.
(181) I. Grgurina: Lipopeptide Secondary Metabolites from the Phytopathogenic Bacterium *Pseudomonas syringae*. In *Advances in Microbial Toxin Research and its Biotechnological Exploitation*; Rajeev K. Upadhayay, K. A., Ed.; Plenum Publisher: New York, 2002.
(182) N. Bionda; J.P. Pitteloud; P. Cudic. Cyclic lipodepsipeptides: a new class of antibacterial agents in the battle against resistant bacteria. *Future medicinal chemistry* **2013**, *5*, 1311-1330.
(183) M.L. Hutchison; D.C. Gross. Lipopeptide Phytotoxins Produced by *Pseudomonas syringae* pv. *syringae:* Comparison of the Biosurfactant and Ion Channle-Forming Activities of Syringopeptin and Syringomycin. *Molecular Plant-Microbe Interactions* **1997**, *10*, 347-354.
(184) A. Fiore; J.M. Laparra; R. Farre; M.R. Fullone; I. Grgurina; M. Gallo; V. Fogliano. Lipodepsipeptides from Pseudomonas syringae Are Partially Proteolyzed and Are Not Absorbed by Humans: An In Vitro Study. *Jorunal of Food Protection* **2008**, *71*, 979-985.
(185) V.V. Malev; L.V. Schagina; P.A. Gurnev; J.Y. Takemoto; E.M. Nestorovich; S.M. Bezrukov. Syringomycin E Channel: A Lipidic Pore Stabilized by Lipopeptide? *Biophysical Journal* **2002**, *82*, 1985-1994.
(186) A.M. Feigin; L.V. Schagina; J.Y. Takemoto; J.H. Teeter; J.G. Brand. The effect of sterols on the sensitivity of membranes to the channel-forming antifungal antibiotic, syringomycin E. *Biochimica et Biophysica Acta (BBA) - Biomembranes* **1997**, *1324*, 102-110.
(187) K.N. Sorensen; K.H. Kim; J.Y. Takemoto. In Vitro Antifungal and Fungicidal Activities and Erythrocyte Toxicities of Cyclic Lipodepsinonapeptides Produced by *Pseudomonas syringae pv. syringae*. *Antimicrobial agents and chemotherapy* **1996**, *40*, 2710-2713.
(188) M.F. Bensaci; P.A. Gurnev; S.M. Bezrukov; J.Y. Takemoto. Fungicidal Activities and Mechanisms of Action of *Pseudomonas syringae pv. syringae* Lipodepsipeptide Syringopeptins 22A and 25A. *Frontiers in microbiology* **2011**, *2*, 216-222.
(189) I. Grgurina; M. Bensaci; G. Pocsfalvi; L. Mannina; O. Cruciani; A. Fiore; V. Fogliano; K.N. Sorensen; J.Y. Takemoto. Novel cyclic lipodepsipeptide from *Pseudomonas syringae pv. lachrymans* strain 508 and syringopeptin antimicrobial activities. *Antimicrobial agents and chemotherapy* **2005**, *49*, 5037-5045.
(190) H. Gu; P.L. Ho; E. Tong; L. Wang; B. Xu. Presenting Vancomycin on Nanoparticles to Enhance Antimicrobial Activities. *Nano Letters* **2003**, *3*, 1261-1263.
(191) E.N. Houben; L. Nguyen; J. Pieters. Interaction of pathogenic mycobacteria with the host immune system. *Current opinion in microbiology* **2006**, *9*, 76-85.
(192) D.L. Clemens; B.Y. Lee; M. Xue; C.R. Thomas; H. Meng; D. Ferris; A.E. Nel; J.I. Zink; M.A. Horwitz. Targeted intracellular delivery of antituberculosis drugs to *Mycobacterium tuberculosis*-infected macrophages via functionalized mesoporous silica nanoparticles. *Antimicrobial agents and chemotherapy* **2012**, *56*, 2535-2545.
(193) Y. Liu; Y. Li; X.M. Li; T. He. Kinetics of (3-aminopropyl)triethoxylsilane (APTES) silanization of superparamagnetic iron oxide nanoparticles. *Langmuir : the ACS journal of surfaces and colloids* **2013**, *29*, 15275-15282.
(194) S.M. Thombre; B.D. Sarwade. Synthesis and Biodegradability of Polyaspartic Acid: A Critical Review. *Journal of Macromolecular Science, Part A* **2005**, *42*, 1299-1315.
(195) N. Sadeghiani; L.S. Barbosa; L.P. Silva; R.B. Azevedo; P.C. Morais; Z.G.M. Lacava. Genotoxicity and inflammatory investigation in mice treated with magnetite nanoparticles surface coated with polyaspartic acid. *Journal of Magnetism and Magnetic Materials* **2005**, *289*, 466-468.
(196) E. Gutierrez; T.C. Miller; J.R. Gonzalez-Redondo; J.A. Holcombe. Characterization of Immobilized Poly-L-aspartate as a Metal Chelator. *Environmental Science & Technology* **1999**, *33*, 1664-1670.
(197) A. Lavasanifar; J. Samuel; G.S. Kwon. Poly(ethylene oxide)-block-poly(L-amino acid) micelles for drug delivery. *Avanced Drug Delivery Reviews* **2002**, *54*, 169-190.

(198) J. Vega-Chacon; M.I.A. Arbelaez; J.H. Jorge; R.F. Marques; M. Jafelicci Jr. pH-responsive poly(aspartic acid) hydrogel-coated magnetite nanoparticles for biomedical applications. *Materials Science and Engineering C: Materials for Biological Applications* **2017**, *77*, 366-373.
(199) J.R. Brannon; J.L. Thomassin; S. Gruenheid; H. Le Moual. Antimicrobial Peptide Conformation as a Structural Determinant of Omptin Protease Specificity. *Journal of bacteriology* **2015**, *197*, 3583-3591.
(200) E. Vaillo; A. Ballio; P. Luisi; R.M. Thomas. The Spectroscopic Properties of the Lipodepsipeptide, Syringomycin E. *Biopolymers* **1992**, *32*, 1317-1326.
(201) S. Gelperina, K. K., M.D. Iseman and L. Heifets. The potential advantages of nanoparticle drug delivery systems in chemotherapy of tuberculosis. *American journal of respiratory and critical care medicine* **2005**, *172*, 1487-1490.
(202) Y.V. Anisimova; S.I. Gelperina; C.A. Peloquin; L.B. Heifets. Nanoparticles as antituberculosis drugs carriers: effect on activity against Mycobacterium tuberculosis in human monocyte-derived macrophages. *Journal of Nanoparticle Research* **2000**, *2*, 165-171.
(203) W.R. Butt: *Hormone Chemistry: Steroid and miscellaneous hormones*; 2nd ed.; Ellis Horwood Ltd: Chichester, 1976; Vol. 2.
(204) L. Bonhomme; D. Benhamou; C. France; E. Comoy; V. France; N. Preaux; C. France. Stability of Epinephrine in Alkalinized Solutions. *Annals of Emergency Medicine* **1990**, *19*, 1242-1244.
(205) G. Eisenhofer; I.J. Kopin; D.S. Goldstein. Catecholamine metabolism: a contemporary view with implications for physiology and medicine. *Pharmacological reviews* **2004**, *56*, 331-349.
(206) T. Deboch; D.A. McGrowder; S.S. Budall. Indexing of Urinary Catecholamines and Metanephrines by Urinary Creatinine Levels in the Diagnosis of Phaeochromocytoma. *Trends in Medical Research* **2006**, *1*, 113-121.
(207) R.T Peaston; C. Weinkove. Measurement of catecholamines and their metabolites. *Annals of Clinical Biochemistry* **2004**, *41*, 17-38.
(208) Y.C. Kudva; A.M. Sawka; W.F. Young Jr. The laboratory diagnosis of adrenal pheochromocytoma: the Mayo Clinic experience. *The Journal of Clinical Endocrinology & Metabolism* **2003**, *88*, 4533-4539.
(209) M.M. Fung; O.H. Viveros; D.T. O'Connor. Diseases of the adrenal medulla. *Acta Physiologica (Oxf)* **2008**, *192*, 325-335.
(210) J. Bicker; A. Fortuna; G. Alves; A. Falcão. Liquid chromatographic methods for the quantification of catecholamines and their metabolites in several biological samples—A review. *Analytica Chimica Acta* **2013**, *768*, 12-34.
(211) G. Eisenhofer; M. Peitzsch; B.C McWhinney. Impact of LC-MS/MS on the laboratory diagnosis of catecholamine-producing tumors. *TrAC Trends in Analytical Chemistry* **2016**, *84*, 106-116.
(212) M.D. Hawley; S.V. Tatawawadi; S. Piekarski; R.N. Adams. Electrochemical Studies of the Oxidation Pathways of Catecholamines. *The Journal of the American Chemical Society* **1967**, *89*, 447-450.
(213) R.N. Goyal; A.R.S. Rana; H. Chasta. Electrochemical and peroxidase-catalyzed oxidation of epinephrine. *Electrochimica Acta* **2012**, *59*, 492-498.
(214) M. Tsunoda. Recent advances in methods for the analysis of catecholamines and their metabolites. *Analytical and bioanalytical chemistry* **2006**, *386*, 506-514.
(215) O.D. Leite; K.O. Lupetti; O. Fatibello-Filho; I.C. Vieira; A. De M. Barbosa. Synergic effect studies of the bi-enzymatic system laccase peroxidase in a voltammetric biosensor for catecholamines. *Talanta* **2003**, *59*, 889-896.
(216) E. Wierzbicka; M. Szultka-Młyńska; B. Buszewski; G.D. Sulk. Epinephrine sensing at nanostructured Au electrode and determination its oxidative metabolism. *Sensors and Actuators B: Chemical* **2016**, *237*, 206-215.
(217) N.G. Mphuthi; A.S. Adekunle; E.E. Ebenso. Electrocatalytic oxidation of Epinephrine and Norepinephrine at metal oxide doped phthalocyanine/MWCNT composite sensor. *Scientific Reports* **2016**, *6*, 26938.

(218) M. Saraji; A. Shahvar. Selective micro solid-phase extraction of epinephrine, norepinephrine and dopamine from human urine and plasma using aminophenylboronic acid covalently immobilized on magnetic nanoparticles followed by high-performance liquid chromatography-fluorescence detection. *Analytical Methods* **2016**, *8*, 830-839.
(219) L. Jiang; Y. Chen; Y. Luo; Y. Tan; M. Ma; B. Chen; Q. Xie; X. Luo. Determination of catecholamines in urine using aminophenylboronic acid functionalized magnetic nanoparticles extraction followed by high-performance liquid chromatography and electrochemical detection. *Journal of separation science* **2015**, *38*, 460-467.
(220) C. Tudisco; F. Bertani; M.T. Cambria; F. Sinatra; E. Fantechi; C. Innocenti; C. Sangregorio; E. Dalcanale; G.G. Condorelli. Functionalization of PEGylated Fe_3O_4 magnetic nanoparticles with tetraphosphonate cavitand for biomedical application. *Nanoscale* **2013**, *5*, 11438-11446.
(221) C.H. Liu; C.J. Yu; W.L. Tseng. Fluorescence assay of catecholamines based on the inhibition of peroxidase-like activity of magnetite nanoparticles. *Analytica Chimica Acta* **2012**, *745*, 143-148.
(222) R. Sharma; S.E. Deacon; D. Nowak; S.E. George; M.P. Szymonik; A.A.S. Tang; D.C. Tomlinson; A.G. Davies; M.J. McPherson; C. Walti. Label-free electrochemical impedance biosensor to detect human interleukin-8 in serum with sub-pg/ml sensitivity. *Biosensors and Bioelectronics* **2016**, *80*, 607-613.
(223) U. Eletxigerra; J. Martinez-Perdiguero; R. Barderas; J.M. Pingarrón; S. Campuzano; S. Merino. Surface plasmon resonance immunosensor for ErbB2 breast cancer biomarker determination in human serum and raw cancer cell lysates. *Analytica Chimica Acta* **2016**, *905*, 156-162.
(224) C. Karunakaran; M. Pandiaraj; P. Santharaman: Chapter 4 - Immunosensors. In *Biosensors and Bioelectronics*; Karunakaran, C., Bhargava, K., Benjamin, R., Eds.; Elsevier, 2015; pp 205-245.
(225) C. Zhou; D. Liu; L. Xu; Q. Li; J. Song; S. Xu; R. Xing; H. Song. A sensitive label–free amperometric immunosensor for alpha-fetoprotein based on gold nanorods with different aspect ratio. *Scientific Reports* **2015**, *5*, 9939.
(226) H.M. Nassef; L. Civit; A. Fragoso; C.K. O'Sullivan. Amperometric Immunosensor for Detection of Celiac Disease Toxic Gliadin Based on Fab Fragments. *Analytical Chemistry* **2009**, *81*, 5299-5307.
(227) K.K. Mistry; K. Layek; A. Mahapatra; C. RoyChaudhuri; H. Saha. A review on amperometric-type immunosensors based on screen-printed electrodes. *Analyst* **2014**, *139*, 2289-2311.
(228) X. Liu; Y. Hu; S. Zheng; Y. Liu; Z. He; F. Luo. Surface plasmon resonance immunosensor for fast, highly sensitive, and in situ detection of the magnetic nanoparticles-enriched Salmonella enteritidis. *Sensors and Actuators B: Chemical* **2016**, *230*, 191-198.
(229) A. Sanchis Villariz. New Immunochemical Approaches for Multiplexed Diagnostics. Universitat de Barcelona, 2018.
(230) N. Sanvicens; I. Mannelli; J.P. Salvador; E. Valera; M.P. Marco. Biosensors for pharmaceuticals based on novel technology. *TrAC Trends in Analytical Chemistry* **2011**, *30*, 541 -553.
(231) V. Urbanova; M. Magro; A. Gedanken; D. Baratella; F. Vianello; R. Zboril. Nanocrystalline Iron Oxides, Composites, and Related Materials as a Platform for Electrochemical, Magnetic, and Chemical Biosensors. *Chem. Mat.* **2014**, *26*, 6653-6673.
(232) A. Muriano; D.G. Pinacho; V. Chabottaux; J.M. Diserens; B. Granier; S. Stead; F. Sanchez Baeza; M.I. Pividori; M.P. Marco. A portable electrochemical magnetoimmunosensor for detection of sulfonamide antimicrobials in honey. *Analytical and bioanalytical chemistry* **2013**, *405*, 7885-7895.
(233) X. Liu; L. Li; Y.Q. Liu; X.B. Shi; W.J. Li; Y. Yang; L.G. Mao. Ultrasensitive detection of deltamethrin by immune magnetic nanoparticles separation coupled with surface plasmon resonance sensor. *Biosensors and Bioelectronics* **2014**, *59*, 328-334.

(234) J. Westermann; W. Hubl; N. Kaiser; L. Salewski. Simple, Rapid and Sensitive Determination of Epinephrine and Norepinephrine in Urine and Plasma by Non-competitive Enzyme Immunoassay, compared with HPLC Method. *Clinical Laboratoy* **2002**, *48*, 61-71.
(235) R.W. Avenia; B. Pecherer. Immunoassay for catecholamines.
(236) O.B. Torres; R. Jalah; K.C. Rice; F. Li; J.F. Antoline; M.R. Iyer; A.E. Jacobson; M.N. Boutaghou; C.R. Alving; G.R. Matyas. Characterization and optimization of heroin hapten-BSA conjugates: method development for the synthesis of reproducible hapten-based vaccines. *Analytical and bioanalytical chemistry* **2014**, *406*, 5927-5937.
(237) S. Yoshitake; M. Imagawa; E. Ishikawa; Y. Niitsu; I. Urushizaki; M. Nishiura; R. Kanazawa; H. Kurosaki; S. Tachibana; N. Nakazawa; H. Ogawa. Mild and Efficient Conjugation of Rabbit Fab' and Horseradish Peroxidase Using a Maleimide Compound and Its Use for Enzyme Immunoassay. *The Journal of Biochemistry* **1982**, *92*, 1413-1424.
(238) S. Hober; K. Nord; M. Linhult. Protein A chromatography for antibody purification. *Journal of Chromatography B: Analytical Technologies in the Biomedical and Life Sciences* **2007**, *848*, 40-47.
(239) J.E. Liddell: *Antibody Purification by Ammonium Sulfate Precipitation*; John Wiley & Sons, Ltd, 2003.
(240) M.M. Bradford. A rapid and sensitive method for the quantitation of microgram quantities of protein utilizing the principle of protein-dye binding. *Analytical Biochemistry* **1976**, *72*, 248-254.
(241) J.D. Bu'Lock. The Formation of Melanin from Adrenochrome. *Journal of the Chemical Society* **1961**, *0*, 52-58.
(242) Z. Tao; G. Wang; J. Goodisman; A. Tewodros. Accelerated Oxidation of Epinephrine by Silica Nanoparticles. *Langmuir : the ACS journal of surfaces and colloids* **2009**, *25*, 10183-10188.
(243) S. Adak; U. Bandyopadhyay; D. Bandyopadhyay; R.K. Banerjee. Mechanism of Horseradish Peroxidase Catalyzed Epinephrine Oxidation: Obligatory Role of Endogenous O_2^- and H_2O_2. *Biochemistry* **1998**, *37*, 16922-16933.
(244) S. Siva; G. Venkatesh; A.M. Prabhu; R.K. Sankaranarayanan; N. Rajendiran. Absorption and fluorescence spectral characteristics of norepinephrine epinephrine isoprenaline methyl dopa terbutaline and orciprenaline drugs. *Physics and Chemistry of Liquids* **2012**, *50*, 434-452.